

UNIVERSITÀ DEGLI STUDI DI MODENA E REGGIO EMILIA

Dottorato di ricerca in Fisica

Scuola di dottorato in Fisica e Nanoscienze

XXVI Ciclo

TESI PER IL CONSEGUIMENTO DEL TITOLO
DI DOTTORE DI RICERCA

ELECTRON CORRELATION IN GRAPHENE QUANTUM DOTS

Candidato: Karina Andrea Guerrero Becerra

Relatore: Dott. Massimo Rontani

Direttore della Scuola di dottorato: Prof. Dott. Marco Affronte

UNIVERSITÀ DEGLI STUDI DI MODENA E REGGIO
EMILIA

DOCTORAL THESIS

Physics and Nanosciences School of Graduate Studies

**Electron Correlation in Graphene
Quantum Dots**

Presented by:

Karina Andrea GUERRERO
BECERRA

Supervisor:

Dr. Massimo RONTANI

January 2015

Acknowledgements

It is a great pleasure for me to thank my mentor Dr. Massimo Rontani for having supervised my work. Foremost, I thank him for the opportunity to work in a topical research field and to present our results at various international conferences, such experience has been very exciting and instructive. Besides, I am especially grateful for his guidance and his enthusiastic support throughout my PhD.

I would like to acknowledge the people who have directly and indirectly contributed to my studies in the CNR-NANO S3 Research Center: Prof. Dr. Elisa Molinari, Dr. Deborah Prezzi, Dr. Filippo Troiani, Dr. Andrea Candini, Dr. Andrea Ferretti, Dr. Stefano Corni, Dr. Ilaria Siloi, Dr. Alberto Lodi Rizzini. I acknowledge also, from other institutions Dr. Marco Polini, Dr. Vittorio Pellegrini, Dr. Joseph Stroschio, Dr. Francesc Malet Giralt, Dr. Pablo San José, Dr. Matthias Droth and Dr. Pierdomenico Memeo.

I would like to express my gratitude also to the following professors at the Università di Modena e Reggio Emilia, for their instruction through formal and informal discussions: Prof. Giorgio Santoro, Prof. Carlo Calandra Buonauro, Prof. Franca Manghi, Prof. Anna Franchini, Prof. Andrea Bizzeti.

It is worth mentioning my former and present colleagues who have contributed to a rich and collaborative environment. Among them I owe many thanks to Dr. Pino D' Amico and Dr. Andrea Secchi for advices and scientific discussions.

My deepest gratitude goes to Carlo and his family, as well as to my sister Maria Paula and to my father Hernando.

This work has been possible thanks to the support of MIUR-PRIN2012 MEMO, EU-FP7 Marie Curie initial training network INDEX, MIUR ABNANOTECH, CINECA-ISCRA grants IscrC_TUN1DFEW, IscrC_TRAP-DIP, and IscrC_PAIR-1D.

Contents

Acknowledgements	i
List of Figures	iv
1 Introduction	1
2 Graphene quantum dots background	5
2.1 Preamble	5
2.2 Electronic graphene properties	8
2.2.1 Crystal and band structure	8
2.2.2 Low-energy excitations	12
2.2.3 Landau levels quantization for Dirac fermions	13
2.3 Confinement in graphene	15
2.3.1 Klein tunneling in graphene	16
2.3.2 Sublattice-induced symmetry breaking and band-gap opening in graphene	19
2.3.3 Single-electron tunneling spectroscopy	21
2.3.4 Towards cleaner graphene quantum dots	27
3 Wigner localization background	31
3.1 The Wigner crystal	31
3.2 The Wigner molecule	33
3.3 Experimental investigation of Wigner molecules	36
3.4 Electron localization in graphene QDs	39
4 Model system and numerical approach	42
4.1 Single-particle model	42
4.1.0.1 Bound-states with magnetic field	44
4.1.0.2 Bound-states with zero magnetic field	47
4.1.0.3 Single particle energy spectrum: magnetic field lifting of the valley degeneracy	49
4.2 Configuration interaction method	51
4.2.1 Introduction to the Configuration Interaction method	51
4.2.2 N-body interacting problem in second quantization	52
4.2.3 Configuration state function expansion	53
4.2.4 Single particle basis-set and two-body matrix elements	54
4.2.5 Numerical methods	60

5	Wigner localization in graphene quantum dots with a mass gap	62
5.1	Theoretical model and single-particle properties	62
5.2	Coulomb blockade spectroscopy	65
5.3	Emergence of radial correlations	66
5.4	Suppression of exchange interactions	68
5.5	Emergence of angular correlations	68
5.6	Excitation spectrum	70
6	Few-body energy spectrum in the presence of a magnetic field	72
6.1	Single-particle energy spectrum	72
6.2	Evolution of Coulomb resonances in a perpendicular magnetic field	75
6.3	Electron localization onset	79
6.4	Discussion	81
7	Conclusion	83
7.1	Summary	83
7.2	Outlook	84
	Bibliography	85

List of Figures

2.1	Graphene crystal structure	8
2.2	Linear dispersion of graphene at the Dirac points	11
2.3	Predicted and measured Landau levels in gapped graphene	15
2.4	Klein tunneling of graphene Dirac massless fermions	18
2.5	Opening of a band gap by inversion symmetry breaking	19
2.6	Quantum dot device for electronic transport	21
2.7	High bias transport regime scheme	24
2.8	Excited-states spectroscopy scheme	26
2.9	Confinement in etched graphene QDs	27
2.10	Atomically precise graphene nanostructures	28
2.11	Graphene QDs in alternative substrates	29
2.12	Electrostatically-defined graphene QDs	29
3.1	Measured correlation-induced singlet-triplet transition	36
3.2	Observation of Wigner molecules in semiconductor QDs	37
3.3	Observation of Wigner molecules in carbon-nanotube QDs	38
3.4	Predicted edge-states Wigner molecules in graphene	39
4.1	Radial confinement potential	43
4.2	Massive single-particle spectrum	49
4.3	Single-particle energy spectrum symmetries	50
4.4	Example of convergence test	60
5.1	Graphene QD defined by electrostatic gates	63
5.2	Non-interacting levels and envelopes	64
5.3	Single-particle level structure washed-out	65
5.4	Emergence of radial correlations	66
5.5	Radial correlations for different dot sizes	67
5.6	Suppression of exchange interactions	67
5.7	Four-electron Wigner molecule: angular correlation	68
5.8	Polygonal Wigner molecules	69
5.9	Quenching of excitation energies	70
6.1	Single-particle levels merging the bulk Landau levels	73
6.2	Radial profiles of non-interacting envelopes at different magnetic fields	74
6.3	Magnetic field dependence of the non-interacting energy spectrum	76
6.4	Chemical potential vs magnetic field: weakly interacting regime	77
6.5	Chemical potential vs magnetic field: highly interacting regime $\varepsilon = 5$	78
6.6	Chemical potential vs magnetic field: highly interacting regime $\varepsilon = 2$	79

6.7	Ground-state angular correlation at selected magnetic fields	80
-----	--	----

Chapter 1

Introduction

This thesis is devoted to the investigation of the effects of electron-electron interactions in graphene quantum dots (QDs). Graphene, a monatomically-thin layer of carbon atoms, is the subject of an exponential growth of publications (and patents) [1, 2, 3] that since 2004—when graphene was synthesized in a controlled way for the first time—has been unrestrained up to now [3]. This intense research is motivated by the fact that graphene combines both fundamental and applicative interests due to the unusual behaviour of its charge carriers and its eminent material properties [4]. Within an unprecedented short period of time the research on graphene has moved from basic science to the first commercial applications¹, and expected industrial breakthroughs² are presently promoted by global investments³. Many of the applications involve graphene-based nano-structures such as QDs. Notwithstanding this fast development, the fundamental research on graphene, which has been extremely fruitful and intense up to now, is far from being exhausted.

Among many active research areas on graphene, the topic of our theoretical investigation is the role of electron-electron interactions [9, 10, 11, 12] that impacts on the operation of quantum dots [13, 14, 15] and other graphene-based nanodevices [14, 16, 17, 18, 19, 20, 21, 22]. Peculiar of graphene—with respect to the conventional two-dimensional electron gas—is the linear, gapless, dispersion relation near the charge neutrality points, and the consequent chirality of graphene charge carriers. With regards to electron-electron interactions, an immediate consideration is that since the density of states

¹first applications, as flexible electronic devices are expected to be available in a few years. For a review on the status and challenges of graphene vast range of applications see Ref. [3].

²disruptive advances are expected in important fields such as: electronics [5], optoelectronic [6] and spintronics [7].

³In Europe, the Graphene Flagship [8], with a budget of 1 billion EUR for the decade 2013-2023 financed by the European Commission, is leading the transition toward graphene industrial adoption. This is only one example of the massive private and state investments which are taking place mainly in USA, China and South Korea; the latter being ranked first in terms of patents [3]

vanishes at the charge neutrality point, the Coulomb interaction is unscreened, therefore one might expect a strongly correlated behaviour at low energies. Indeed, the fine structure constant $\alpha = e^2/(\varepsilon\hbar v_F)$ —which is the ratio of Coulomb to Fermi energy—is of order unity for most of the relevant experimental regimes, much larger than the value $\alpha = 1/137$ of quantum electrodynamics, therefore the many-body problem may not be treated with perturbative methods (here ε is the background dielectric constant and v_F the Fermi velocity). As a matter of fact, the predicted ratio of viscosity to entropy per electron is characteristic of an extremely interacting quantum fluid [23]. However, electrons in bulk graphene allegedly behave as noninteracting particles [24], except for subtle effects due to velocity renormalization [25, 26, 27], coupling with phonons or plasmons [28, 29], and a hypothetical excitonic gap [30, 31, 32]. The key to this paradox is that the density parameter r_s , which quantifies the impact of electron correlations [33], does not depend on the electron density n but coincides with α [34]. In contrast, $r_s \sim n^{-1/2}$ of the conventional two-dimensional electron gas [35] increases as n decreases due to the massive dispersion of electrons. An electron solid (Wigner crystal) is even predicted in the dilute limit [36], as the long-range order induced by Coulomb interaction localizes electrons in space. Therefore, a way to disclose the many-body physics of graphene is to make electrons massive, invalidating the above scaling argument. This occurs e.g. in the fractional quantum Hall effect [37, 38] and in bilayer graphene [39], which might be an excitonic insulator [32, 40].

The question that we consider in this thesis is whether strongly correlated behaviour may take place in finite-size graphene systems. To this aim, we explore theoretically the few-body physics of a graphene QD with a mass gap. The motivation to our study is twofold: On one side, electrons in semiconductor QDs may form Wigner molecules (WMs), [41, 42, 43, 44] i.e., finite-size precursors of the Wigner crystal, including carbon-based nanostructures—nanotubes—for which the effect is dramatic [45]. On the other side, a current trend in graphene QDs is to minimize the roles of disorder and edge states, which are extrinsic sources of localization. These next-generation devices include atomically precise nanoribbons [18, 46] and bilayer QDs—defined through gates [20, 47, 48, 49, 50] combined with the exploitation of optimal substrates [21, 51, 52].

Previous investigations already suggested that electrons in graphene QDs may crystallize. However, most of these analyses were limited to degenerate edge states that are sensitive to interactions as well as to all kinds of perturbations [53, 54, 55, 56], whereas other theories treated Coulomb interaction at the mean field level [57], which may artificially enhance localization [41], or considered only valley-polarized electrons [58], which artfully breaks time-reversal symmetry. The aim of the present work is to provide a complete description of the interaction effects among delocalized states in disorder-free

dots by accounting for the presence of the two inequivalent Dirac cones. In order to include correlations at all orders we employ the exact diagonalization of the full interacting Hamiltonian. Results will show that strong correlation plays a crucial role for realistic graphene devices with a mass gap. The evidence we obtained relies on the analysis of exact few-body observables, including different kinds of correlation functions. In order to provide precise predictions for future experiments we analyse observables accessible through magneto-transport tunneling spectroscopy. Despite the fact that we focused on a specific type of device we expect our conclusions to be generic to clean carbon-based nanostructures exhibiting a mass gap, including atomically precise ribbons and bilayer graphene quantum dots.

The structure of the Thesis is as follows:

Chapter 2. Introduces the fundamental aspects of graphene behind its outstanding electronic properties and the features relevant for the present work. The second section is dedicated to the confinement of charge carriers in graphene. The problems related to electrostatic confinement and to the lack of a band gap are surveyed. The basic concepts of electron transport through quantum dots—that are needed to interpret tunneling spectroscopy measurements—are given. Lastly the ongoing experimental progress towards cleaner graphene QDs is discussed.

Chapter 3. Contains an introduction to the concept of Wigner localization in the two-dimensional conventional electron gas (with quadratic dispersion relation of charge carriers) as compared to graphene. The concept of electron localization in semiconductor-based finite-size systems—widely studied—is reviewed, highlighting the existing experimental evidence of strong electron correlation in QDs. Finally we consider the theoretical works dedicated to this subject in graphene QDs.

Chapter 4. Presents the model system, the formulation of the problem of few-interacting charge carriers in the graphene QD under investigation, and provides a detailed description of the analytical and numerical methods used to solve it. Both the cases of presence and absence of a magnetic field, normal to the graphene surface, are treated.

Chapter 5. An extended version of the results published in the paper K. A. Guerrero-Becerra and M. Rontani Phys. Rev. B 90, 125446 (2014) is proposed. We consider a clean, circular QD with a mass gap induced by the breaking of sublattice symmetry. This could be realized through the interaction between graphene and substrate [59]. The presence of the gap allows to electrostatically define the QD as well as to perform Coulomb blockade spectroscopy. Evidence of Wigner molecule formation is presented and a recipe for its observation from transport experiments is given.

Chapter 6. The energy spectrum of graphene QDs with a mass gap in the presence of a perpendicular magnetic field is studied in an extended range of magnetic field values, including the emergence of Landau levels. The effect of increasing interaction is

investigated. Detailed predictions amenable to comparison with magneto-transport experiments are given.

Chapter 2

Graphene quantum dots background

2.1 Preamble

Graphene is a two-dimensional (2D) carbon allotrope with relativistic charge carriers. Early theoretical investigations, based on tight binding calculations, back in the forties [60], found that the electronic properties of a single layer of graphite are unusual, featuring a linear dispersion relation at low energies. The initial investigations treated graphene as a simpler model to study the widely used material graphite [61], and its two-dimensional character was merely an academic issue, however they identified the semimetal character of undoped graphene. Remarkably, the low-energy fermionic excitations in graphene—electrons on the conduction band and holes in the valence band—are governed by an equation, determined back in 1956 [62], which resembles—as pointed out in the eighties [63, 64]—the Dirac-Weyl ultra-relativistic 2D equation describing massless neutrinos, albeit with the velocity factor multiplying the momentum being 300-times smaller. Indeed, graphene low-energy excitations are described by a two component wave function whose components encode the pseudospin degree of freedom that, in analogy to the spin, confers them a defined helicity. The huge implications of these early discoveries will flourish only after graphene isolation in 2004.

Notwithstanding the existence of two-dimensional crystals was questioned by thermodynamic arguments [65, 66, 67, 68], graphene is the first truly two-dimensional material which has become experimentally attainable [69, 70]. Attempts to isolate graphene were performed already in the sixties by the same authors who proposed to standardize its

name [71]. However, reduced graphene-oxide rather than pristine ¹ graphene was obtained. Other early reports were anticipatory of some of the actual techniques [73], reaching samples not amenable to be electrically characterized [74, 75] or not reaching the identification of single layers [76]. The first electrical characterization of clearly isolated graphene was performed in 2004 by K. Novoselov, A. Geim and coworkers [69]. It was obtained by fully exploiting the micromechanical cleavage approach—which consist on pressing high purity graphite against a silicon wafer and on breaking the low van der Waals force between the layers by repeatedly peeling graphite—the single layer was detected by the standard optical microscopy technique, exploiting the optimized contrast of a silicon wafer surface.

The isolation of the 2D carbon allotrope ²—awarded by the Nobel Prize in physics in 2010 [77]—inaugurated a fast developing area on fundamental physics studies, animated the research on other 2D materials ³ and fired up huge amounts of research on proof-of-concept devices and applications.

The peculiarity of graphene low-energy excitations with respect to *conventional*⁴ materials excitations, relying on graphene’s crystal symmetries, enforced the reconsideration of well known effects in the field of solid state physics. Soon after graphene isolation the observation of the half-integer quantum hall effect [78, 79] sensationally confirmed the Dirac-like description of charge carriers in graphene. Indeed, the half-integer quantum hall effect is a direct consequence of the quantization of a relativistic massless electronic spectrum in a magnetic field. The effect consists on an unusual sequence—shifted by 1/2 respect to the standard quantum hall effect—of Hall conductance plateaus when measured as a function of the electron density. In graphene the effect is observable at room temperature, as the Landau levels spacing is larger than the thermal energy, in contrast to conventional materials [80].

Another manifestation of graphene massless excitations is the tunnelling through arbitrary potential barriers with unitary probability, that is a consequence of the charge-conjugation symmetry of graphene excitations. The effect is known as Klein tunneling, it was early predicted [81], but it has been elusive in particle physics so far due to the fact that it is needed a huge electric field, varying sharply in very short length scales to take place. It was observed for the first time in graphene [82, 83] as an enhanced conductivity in abrupt potential barriers, induced by metallic gates. This phenomenon

¹without "heteroatomic contamination" [72]

²the missing allotrope among the three-dimensional diamond and graphite, the one-dimensional carbon-nanotubes and the zero-dimensional fullerene

³as boron nitride BN, tungsten disulfide WS₂, molybdenum disulfide MoS₂ or gallium selenide GaSe

⁴this epithet throughout the thesis will refer to materials with charge carriers described by the Schoedinger’s equation, widely metals and semiconductors where the energy spectrum is typically approximated by a parabolic dispersion relation

has important consequences for the transport properties of graphene: confinement of charge carriers is not achieved through electrostatic gates the same way as in conventional semiconductors-based devices. On the other hand, the presence of electrostatic barriers, induced by disorder, does not lead to Anderson localization of charge carriers [84].

Another elusive quantum electrodynamics prediction which found experimental demonstration in graphene is the—so called—atomic collapse, a relativistic phenomenon which renders atoms unstable above a nuclear charge threshold ($Z > 170$), not available among natural neither artificial nuclei. The phenomenon consists on the collapse of electrons into a supercritical electric field, by emitting an antiparticle. The artificial nucleus was simulated by grouping calcium atoms on the graphene surface, and the effect manifested as a specific spectrum of resonances [85], in accordance with predictions [86]. In graphene the threshold for observing the effect is much smaller, due to the large graphene effective fine structure constant which governs the strength of the interaction between charges and depends only on material parameters.

The consequences of graphene dimensionality are also remarkable. Already its existence under ambient conditions, as mentioned above, was a surprising demonstration of mechanisms—crumpling or wrinkling—stabilizing a two-dimensional crystal [87] subject to thermodynamic fluctuations, as predicted by the Mermin-Wagner theorem [68]. The entire field of research on 2D atomic crystals [70], increased remarkably after graphene isolation, as well as the interest on heterostructures built on them [88]. A consequence of the motion of electrons in the 2D super-lattice created by placing graphene on a boron-nitride surface, as exposed to a strong magnetic field, is a fractal structure of the density of states when measured as a function of the magnetic field. The effect, known as Hofstadter's butterfly, that was measured both in graphene [89] and in bilayer graphene [90]—again—had been long sought since its prediction [91] without success. The difficulty of its observation relies on the infeasible high magnetic field needed to obtain incommensurability between the cyclotron frequency and the lattice structure.

The precedent are examples of the richness of the fundamental investigation of bulk graphene manifesting in the behaviour of charge carriers interacting among them and with external fields. Graphene charge carriers can be further confined to construct one-dimensional or zero-dimensional structures such as nano-wires and graphene quantum dots. Beyond being of fundamental interest, the investigation of these structures has been also motivated by the graphene prominent properties, appealing for nano-electronic applications among many others (see Ref. [3]). Indeed, graphene has great strength, it supports high electron densities, it has long mean free-paths⁵ and remarkably high

⁵about 400 nm at room temperature

mobilities ⁶. Graphene-based nano-structures exhibit ballistic transport at room temperature [52] and quantum coherence extending over micrometer distances. Furthermore graphene is integrable into existing electronic devices, and can be patterned in different sizes with consistent electronic properties, an advantage over carbon-nanotubes. Respect to the latter, graphene nano-structures can be seamlessly interconnected [92] overcoming problems related to contacts and improving nano-electronic circuitry. Single electron transistors and entire integrated circuits have been designed entirely on graphene [15, 80]. Some graphene-based devices have already shown the potentialities of this promise, as an example, graphene-based high speed transistors have been developed by different groups [93, 94].

2.2 Electronic graphene properties

2.2.1 Crystal and band structure

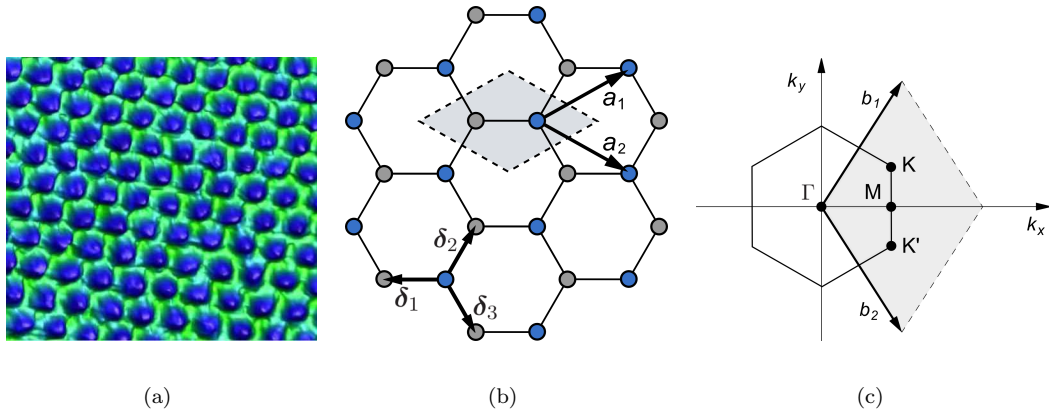


FIGURE 2.1: (a) Transmission electron microscope (false color) image of suspended graphene showing the hexagonal network of carbon atoms. Figure adopted from Ref. [95] (b) Direct space graphene lattice composed by two inter-penetrating triangular lattices, denoted as A-type (gray) and B-type (blue) sublattices. The primitive lattice vectors of the triangular Bravais lattice are indicated as \mathbf{a}_1 and \mathbf{a}_2 . The unit cell is the shaded region. The vectors δ_1 , δ_2 and δ_3 denote the vectors linking each carbon atom to three nearest-neighbour atoms on the different sublattice. (c) Reciprocal graphene lattice generated by the vectors \mathbf{b}_1 , \mathbf{b}_2 . The corners of the hexagonal Brillouin zone belong to two equivalence classes referred as K and K'.

Graphene is a single layer of carbon atoms arranged in an hexagonal, honeycomb-like network. This lattice structure—shown in Fig. 2.1(a) reporting a transmission electron microscope image of suspended graphene—is determined by the planar σ bonds connecting each carbon atom to its three neighbours. The σ bonds are the strongest form of covalent bonds, they are formed by the hybridized sp^2 orbitals of adjacent carbon atoms

⁶exceeding over 20 times Si-based materials

involving three carbon atom valence electrons. The fourth valence electron is in the $2p_z$ orbital normal to the lattice plane, this orbital hybridize with other analogue orbitals of neighbour atoms and concur to the formation of delocalized π orbitals. Electrons in the π orbitals are responsible for the transport properties of graphene.

The hexagonal crystal structure of graphene is composed of two inter-penetrating triangular sublattices which are given the A and B labels (gray and blue atoms in Fig. 2.1(b)). The Bravais triangular lattice can be constructed from the primitive lattice vectors $\mathbf{a}_1 = a_0(3, \sqrt{3})/2$ and $\mathbf{a}_2 = a_0(3, -\sqrt{3})/2$, with $a_0 \approx 1.42 \text{ \AA}$ the carbon-carbon distance, of modulus (lattice constant) $a = |\mathbf{a}_1| = |\mathbf{a}_2| = \sqrt{3}a_0 \approx 2.46 \text{ \AA}$. The unit cell (shaded rhombus in Fig. 2.1(b)) has area $\mathcal{A} = \sqrt{3}a^2/2 \approx 5.1 \text{ \AA}^2$ and contains one carbon atom per each A/B sublattice [10]. The nearest neighbour vectors of the bipartite lattice have positions $\boldsymbol{\delta}_1 = a_0(-1, 0)$, $\boldsymbol{\delta}_2 = a_0(1, \sqrt{3})/2$ and $\boldsymbol{\delta}_3 = a_0(1, -\sqrt{3})/2$ and link atoms of different sublattices.

The reciprocal lattice is in turn triangular with lattice vectors given by $\mathbf{b}_1 = 2\pi(1, \sqrt{3})/3a_0$ and $\mathbf{b}_2 = 2\pi(1, -\sqrt{3})/3a_0$ in the reference frame shown in Fig. 2.1(c). The hexagonal first Brillouin zone (BZ) (Fig. 2.1(c)) displays highly symmetric points located at the center $\Gamma = (0, 0)$, center of the edge $\mathbf{M} = 2\pi(1, 0)/3a_0$ and two apexes $\mathbf{K} = 2\pi(1, 1/\sqrt{3})/3a_0$ and $\mathbf{K}' = 2\pi(1, -1/\sqrt{3})/3a_0$ of the hexagon. The remaining four corners of the first BZ can be obtained from the \mathbf{K} and \mathbf{K}' positions through translation by a reciprocal lattice vector, the so obtained equivalence class will be denoted as K and K'. Note that the points \mathbf{K} and \mathbf{K}' are not connected from each other by linear combinations of \mathbf{b}_1 and \mathbf{b}_2 , i.e., they are inequivalent.

K and K' are known as Dirac points because the dispersion relation of graphene in their proximity is linear as for massless Dirac fermions. This peculiarity of the graphene electronic structure near to the Fermi level is captured by the simplified one-orbital tight-binding (TB) model for the π states, first obtained by Wallace [60] in 1947. Below it is considered the nearest-neighbour approximation version of the TB model and effects beyond this approximation are discussed. The crucial attribute of the graphene lattice structure is its bipartite nature, the Bloch wavefunction capturing this attribute can be written as

$$\Psi_{\mathbf{k}}(\mathbf{r}) = \Phi_A(\mathbf{k}) \sum_{\mathbf{R}_A} e^{i\mathbf{k}\mathbf{R}_A} \varphi_{p_z}(\mathbf{r} - \mathbf{R}_A) + \Phi_B(\mathbf{k}) \sum_{\mathbf{R}_B} e^{i\mathbf{k}\mathbf{R}_B} \varphi_{p_z}(\mathbf{r} - \mathbf{R}_B) \quad (2.1)$$

where $\Phi_A(\mathbf{k})$ and $\Phi_B(\mathbf{k})$ (with $\mathbf{k} = (k_x, k_y)$ the momentum) describe the amplitude of the electron wavefunction to occupy the sublattice A and B respectively. $\varphi_{p_z}(\mathbf{r} - \mathbf{R}_{A/B})$ is the wavefunction of the p_z -orbital centered at the lattice sites \mathbf{R}_A or \mathbf{R}_B in each sublattice. The Schrödinger equation for the Bloch state $\hat{H}\Psi_{\mathbf{k}}(\mathbf{r}) = E\Psi_{\mathbf{k}}(\mathbf{r})$ can be

formulated in terms of the eigenvalue problem

$$\begin{pmatrix} E & -t \sum_i e^{-i\mathbf{k}\cdot\boldsymbol{\delta}_i} \\ -t \sum_i e^{i\mathbf{k}\cdot\boldsymbol{\delta}_i} & E \end{pmatrix} \begin{pmatrix} \Phi_A(\mathbf{k}) \\ \Phi_B(\mathbf{k}) \end{pmatrix} = 0 \quad (2.2)$$

for the coefficients $\Phi_{A/B}$. The deduction assumes vanishing overlap between orbitals more than one atom apart, exploits the lattice symmetries of the Hamiltonian and assumes vanishing on-site energies, i.e., redefines the zero of the energy at the crossing point between the conduction and the valence bands. The nearest-neighbour transfer integral $-t$ ⁷ with $t \approx 2.8$ eV⁸ is the only contribute of the lattice Hamiltonian. The vectors $\boldsymbol{\delta}_i$, with $i = 1, 2, 3$, linking nearest-neighbour atoms retain the lattice structure. From 2.2 the dispersion relation

$$E(\mathbf{k}) = \pm t \left| \sum_i e^{i\mathbf{k}\cdot\boldsymbol{\delta}_i} \right| = \pm t \sqrt{3 + 2 \cos(\sqrt{3}k_y a_0) + 4 \cos\left(\frac{\sqrt{3}}{2}k_y a_0\right) \cos\left(\frac{3}{2}k_x a_0\right)} \quad (2.3)$$

is deduced. The \pm sign distinguishes the conduction antibond- π^* band from the valence bonding- π band which are symmetric and touch at the K and K' points. This degeneracy makes of undoped graphene a semimetal (or a zero-gap semiconductor) with the Fermi surface reduced to the six corners of the BZ, in fact there are two electrons per unit cell filling completely the π band. The inclusion of the next-nearest neighbour hopping brings to the expression for the dispersion relation $E(\mathbf{k}) = \pm t \left| \sum_i e^{i\mathbf{k}\cdot\boldsymbol{\delta}_i} \right| - t' (|\sum_i e^{i\mathbf{k}\cdot\boldsymbol{\delta}_i}|^2 - 3)$. The next-nearest neighbour hopping removes the electron-hole symmetry of the spectrum so that $E(\mathbf{k}) \neq E(-\mathbf{k})$, and shifts the energy of the K and K' points, it is however a small contribution (different tight binding parametrizations estimate it within the range $0.02t \lesssim t' \lesssim 0.2t$ [10]) which does not changes the behaviour of the Hamiltonian near the Dirac points [98]. The low-energy limit is obtained from 2.3 by an expansion for the wavevector $\mathbf{k} = \boldsymbol{\delta}\mathbf{k} + \mathbf{K}$ near to the K point, for $|\boldsymbol{\delta}\mathbf{k}| \ll |\mathbf{K}|$, leading to

$$\sum_i e^{i(\mathbf{K}+\boldsymbol{\delta}\mathbf{k})\cdot\boldsymbol{\delta}_i} \approx \frac{3a_0}{2} e^{i\theta} (\delta k_x + i\delta k_y) \quad (2.4)$$

where the phase θ depends on the choice of the relative phase of the sublattices and can be absorbed through a redefinition of $\Phi_{A/B}$. By defining $v_F = 3a_0 t / 2\hbar \approx 10^6$ m/s, the conical dispersion

$$E(\boldsymbol{\delta}\mathbf{k}) \approx \pm \hbar v_F |\boldsymbol{\delta}\mathbf{k}| + O[|\boldsymbol{\delta}\mathbf{k}/\mathbf{K}|^2] \quad (2.5)$$

describes the energy dispersion of the primary bands near to the K point. An analogous expansion near to K' brings to the same result [60]. Importantly 2.5 implies that the Fermi velocity $v_F = (1/\hbar)(\partial E/\partial k)$ is constant in contrast to the conventional case of

⁷ $-t \equiv \int d\mathbf{r} \varphi_{p_z}(\mathbf{r} - \mathbf{R}_A) H \varphi_{p_z}(\mathbf{r} - \mathbf{R}_A + \boldsymbol{\delta}_1)$

⁸the estimated value range over [2.7, 3.1] eV, see Ref. [96, 97]

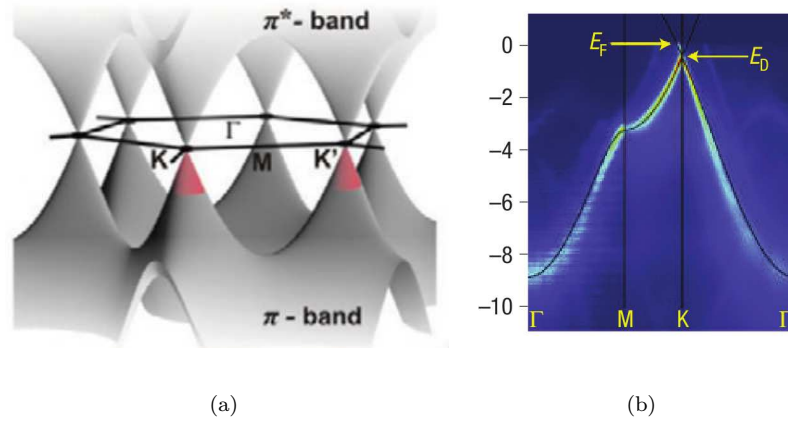


FIGURE 2.2: (a) Computed dispersion relation of graphene at low energies near to the Dirac points. Figure adapted from Ref. [99] (b) Measured graphene linear dispersion, obtained through the ARPES technique. Figure adapted from Ref. [100]

parabolic dispersion, where the velocity depends on the energy by $v = \sqrt{2E/m}$. Another important implication of the linear dispersion 2.5 is that the density of states (DOS) linearly vanishes at the Dirac points. The DOS per unit cell in the proximity of the Dirac point reads

$$\mathcal{D}(E) = \frac{2\mathcal{A}|E|}{\pi(\hbar v_F)^2} \quad (2.6)$$

with \mathcal{A} the unit cell area, this expression includes valley and spin degeneracy [10]. This vanishing electron density at the Dirac points implies that in neutral graphene the long-range Coulomb interaction is not screened as in metals. This characteristic make graphene a very peculiar system also from the point of view of electron-electron interactions [12].

The first angle resolved photoemission spectroscopy (ARPES) measurement of the linear dispersion of graphene is shown in Fig. 2.2(b), reporting from Ref. [100] the primary bands of epitaxial graphene, well reproduced by the simplified tight-binding expression 2.3 (black solid line) by including an energy shift (of about 0.45 eV) of the Fermi energy (E_F) from the Dirac point (E_D), which accounts for the p-doping effect on graphene, induced by the substrate SiC. Deviations from the linear dispersion near to the Dirac points can be deduced from the energy dispersion expansion up to the second order

$$E(\delta\mathbf{k}) \approx \pm\hbar v_F|\delta\mathbf{k}| + 3t' - \left[\frac{9t'a_0^2}{4} \pm \frac{3ta_0^2}{8} \sin(3\theta_{\delta\mathbf{k}}) \right] |\delta\mathbf{k}|^2 \quad (2.7)$$

including nearest t and next-nearest t' hoppings. The inclusion of second-order terms in $(\delta\mathbf{k}/\delta\mathbf{K})$ introduces a three-fold symmetric angular dependence of the spectrum on the angle in momentum space $\theta_{\mathbf{k}} = \arctan(\delta k_x/\delta k_y)$, known as trigonal warping, whose anisotropy increases by moving away from the Dirac point.

2.2.2 Low-energy excitations

The electronic transport properties of pristine graphene, when the Fermi level is at the intersection of the conical bands, are determined by the band structure near the K and K' points, while the bands away from this points are beyond the energy range relevant for transport. The linear expansion 2.4 of the tight binding Hamiltonian 2.2 of graphene near the Dirac point K leads to the effective equation ⁹

$$\hbar v_F \begin{pmatrix} 0 & k_x - ik_y \\ k_x + ik_y & 0 \end{pmatrix} \begin{pmatrix} \Phi_A \\ \Phi_B \end{pmatrix} = E \begin{pmatrix} \Phi_A \\ \Phi_B \end{pmatrix} \quad (2.8)$$

describing graphene low-energy electron and hole states. By introducing the operator $\hat{\tau} = (\hat{\tau}_1, \hat{\tau}_2, \hat{\tau}_3)$, which components are the Pauli matrices, acting on the sublattice space, Eq. 2.8 can be written in analogy to the Dirac-Weyl equation describing massless fermions in two dimensions [101]

$$H_K = \hbar v_F \mathbf{k} \cdot \hat{\tau}. \quad (2.9)$$

Around the K' point, a similar expansion yields to

$$H_{K'} = -\hbar v_F \hat{\tau}^* \cdot \mathbf{k}, \quad (2.10)$$

as stated by time reversal symmetry, explicitly

$$H_{K'} = \hbar v_F \begin{pmatrix} 0 & -k_x - ik_y \\ -k_x + ik_y & 0 \end{pmatrix}. \quad (2.11)$$

It is worth noting that the validity of these effective Hamiltonians is restricted to the description of graphene low-energy excitations close to the Dirac points—as long as anisotropic effects, up to the second order in k , can be neglected—i.e., for momentum $|\mathbf{k}| \ll 1/a$ close to the degeneracy points and in an energy range $|E| \lesssim t$. Within its range of validity, the formal analogy to ultra-relativistic (massless) fermions goes beyond the linear dispersion $E(\mathbf{k}) \approx \pm \hbar v_F |\mathbf{k}|$ arising from the Hamiltonian: the spinor here encodes the sublattice graphene structure and it is known as pseudospin since it transforms as the spin spinor under rotations. Furthermore the direction of the pseudospin is tighten to the direction of the momentum, i.e. the helicity ¹⁰ operator $\hat{h} = \hat{\tau} \cdot \mathbf{k}/|\mathbf{k}|$ commutes with the Hamiltonian. By introducing the valley index τ , distinguishing between the K ($\tau = 1$) and the K' ($\tau = -1$) valleys, the eigenvectors of H_K and $H_{K'}$ in real space can

⁹ to simplify notation hereafter we will denote $\delta\mathbf{k}$ with \mathbf{k} to be counted from the Dirac point.

¹⁰the term *chirality* is also widely used, chirality is identical with helicity only for massless particles

be written as [102]

$$\langle \mathbf{r} | \Phi_{\pm, \tau} \rangle = \Phi_{\pm, \tau}(\mathbf{r}) = \frac{1}{\sqrt{2}} \begin{pmatrix} e^{-i\tau\theta_{\mathbf{k}}/2} \\ \pm e^{i\tau\theta_{\mathbf{k}}/2} \end{pmatrix} e^{i\mathbf{k}\mathbf{r}} \quad (2.12)$$

it is recalled that $\theta_{\mathbf{k}} = \arctan(k_x/k_y)$, here the sign \pm refers to conduction and valence bands with respective energy eigenvalues $E(\mathbf{k}) = \pm\hbar v_F |\mathbf{k}|$. The helicity eigenvalue is positive (negative) for conduction-band states whereas it is negative (positive) for valence-band states at K (K'). Positive helicity corresponds to parallel momentum and pseudospin whereas negative helicity to anti-parallel vectors [103]. Note that this formalism of two separate Hamiltonians from K and K' is useful while the valleys are decoupled, which is the case in absence of atomic-scale inhomogeneities arising e.g. from boundaries or external electric or magnetic fields with relevant variations at the atomic scale.

2.2.3 Landau levels quantization for Dirac fermions

The unconventional linear dispersion, pseudospin and symmetries of graphene charge-carrier states noteworthy manifest in the presence of a magnetic field. Indeed, a determining prove of the Dirac massless-fermionic nature of graphene charge carriers was provided by the observation of the anomalous integer quantum hall effect (IQHE) by [78] [79] in 2005. A strong magnetic field applied to a two-dimensional electron gas gives rise to well-defined quantized energies known as Landau levels [104], which can be accessed through magneto-transport [105], scanning tunneling spectra [106] experiments, capacitance measurements [107] or even through infra-red transmission [108, 109] measurements. Here the distinctiveness of the Landau level spectrum of graphene—early computed by [110] or more recently by [111]—respect to the one measured in conventional semiconductor heterostructures is discussed after Ref. [112].

The inclusion of the effect of a perpendicular magnetic field $\mathbf{B} = \nabla \times \mathbf{A} = (0, 0, B)$ in the kinetics can be done by substituting ¹¹ $\mathbf{k} = -i\nabla \rightarrow -i\nabla + (e/\hbar)\mathbf{A}$ in Eq. 2.8 leading to

$$H_K = \hbar v_F (-i\hat{\nabla} + (e/\hbar)\mathbf{A}) \cdot \hat{\tau} \quad (2.13)$$

The magnetic field introduces the length $l_B = \sqrt{\hbar/eB}$ (magnetic length) scale. The solutions of the eigenvalue problem can be found analytically, e.g. by the choice of the

¹¹minimal coupling substitution, justified as $l_B \gg a_0$ which would be violated for magnetic fields as large as $B \gg 10^4$ T

Landau gauge $\mathbf{A} = B(-y, 0, 0)$ the Hamiltonian 2.13 becomes:

$$\hbar v_F \begin{pmatrix} 0 & -i\partial_x - y/l_B^2 - \partial_y \\ -i\partial_x - y/l_B^2 + \partial_y & 0 \end{pmatrix}. \quad (2.14)$$

By writing $\Phi(\mathbf{r}) = (\Phi_A(\mathbf{r}), \Phi_B(\mathbf{r}))^\top = e^{ik_x x} (\Phi_A(y), \Phi_B(y))^\top$, as $[\hat{H}, k_x] = 0$, the eigenvalue problem $\hat{H}_K \Phi = E \Phi$ can be recast into the decoupled equations for the spinor components

$$\begin{cases} [-\partial_y^2 + (k_x - \frac{y}{l_B^2})^2] \Phi_A(y) & = [(\frac{E}{\hbar v_F})^2 - \frac{1}{l_B^2}] \Phi_A(y) \\ [-\partial_y^2 + (k_x + \frac{y}{l_B^2})^2] \Phi_B(y) & = [(\frac{E}{\hbar v_F})^2 + \frac{1}{l_B^2}] \Phi_B(y) \end{cases} \quad (2.15)$$

which are harmonic oscillator equations with energy solutions

$$\begin{cases} E = \pm \hbar w_D \sqrt{n_A + 1} & \text{for } n_A = 0, 1, 2, \dots, \\ E = \pm \hbar w_D \sqrt{n_B} & \text{for } n_B = 0, 1, 2, \dots \end{cases} \quad (2.16)$$

Here $w_D = \sqrt{2} v_F / l_B$ denotes the cyclotron frequency for Dirac fermions [62], and the sing \pm refers to conduction (+) and valence (-) bands. The corresponding LL states are harmonic oscillator wavefunctions with center of the electron orbit $y = k_x l_B^2$. The number of LL states per unit area increases with B , being $n_L = eB/h$. From 2.16 it follows that there is a zero energy $E_0 = 0$ LL (the so-called 'zero mode'), corresponding to $n_B = 0$, which is shared by electrons and hole states. The corresponding eigenspinor is not a mix of pseudospin states but have only one non-null sublattice component. In the valley K' , Eq. 2.16 with the A and B indexes inverted holds, therefore the expression $E = \pm \hbar w_B \sqrt{n}$ (and $n = 0, 1, 2, \dots$) without valley specification is often used. Each LL host $4n_L$ states per unit area due to spin and valley degeneracy¹². Recalling the LLs of conventional 2D semiconductors $E_S \propto B(n + 1/2)$ [113] (with $n = 0, 1, 2, \dots$) it is notable that the graphene quantized spectrum in Eq. 2.16 has the following peculiarities. Graphene LLs depend on the square root of the magnetic field, and the energy spectrum is not equidistant; these are consequences of the linear rather than parabolic energy dispersion. The existence of the zero energy LL in graphene, linked to topological reasons (the index theorem [114]), is robust respect to eventual inhomogeneities of the magnetic field [98]. The graphene LLs separation is larger than the corresponding one in conventional semiconductor-based 2DEG and than the thermal energy for reasonable magnetic field values. All this features have important experimental consequences which are epitomized in the observation of the IQHE at room temperature [115].

¹²the graphene LLs separation is larger than the Zeeman splitting if only the low-lying LLs are filled, in this situation, the four-fold degeneracy is assured

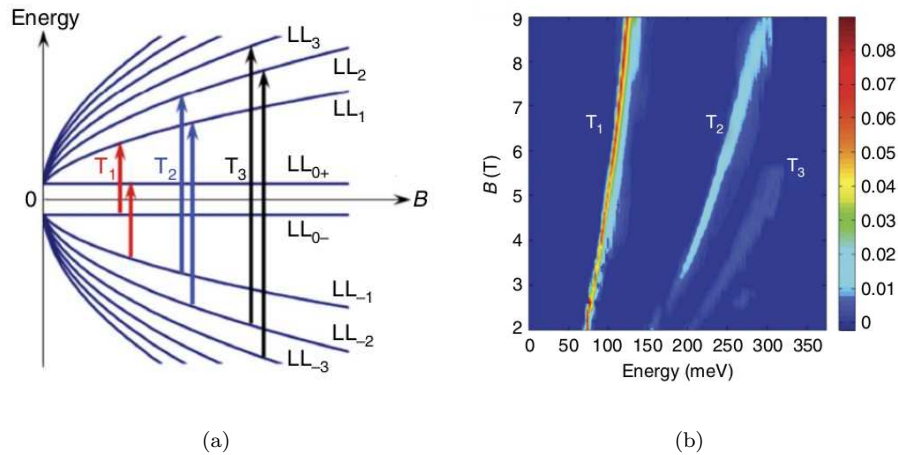


FIGURE 2.3: (a) Landau levels of graphene in the presence of a band gap in the energy spectrum, provided by interaction with a h-BN substrate at zero crystallographic alignment angle. (b) Infrared transmission spectra of the transitions between LLs indicated in figure (a). The logarithm of the magneto-transmission ratio spectra $-\ln(T(B)/T(B_0))$, for $B_0 = 0$, is shown vs the magnetic field. Both images are adapted from Ref. [109].

In the presence of an asymmetric potential between the two sublattices, as induced by the interaction with a periodic substrate (see Section 2.3.2), the Hamiltonian in the K valley becomes $H_K = \hbar v_F(-i\hat{\nabla} + (e/\hbar)\mathbf{A}) \cdot \hat{\tau} + \Delta\hat{\tau}_3$, with the diagonal term $\Delta\hat{\tau}_3$ including the difference between the potential energy in the A and in the B sublattices 2Δ . This Hamiltonian leads to the LL spectrum

$$\left\{ \begin{array}{l} E = \pm \sqrt{\Delta^2 + \frac{2(\hbar v_F)^2(n_A + 1)}{(l_B)^2}} \quad \text{for } n_A = 0, 1, 2, \dots, \\ \\ E = \pm \sqrt{\Delta^2 + \frac{2(\hbar v_F)^2(n_B)}{(l_B)^2}} \quad \text{for } n_B = 0, 1, 2, \dots \end{array} \right. \quad (2.17)$$

Fig. 2.3(b) reports the direct measurement of low laying LLs of Eq. 2.17 in epitaxial graphene perfectly aligned on a h-BN substrate. The magneto-optic measurement register the transitions between the LLs indicated in Fig 2.3(a).

2.3 Confinement in graphene

Quantum dots are 0-dimensional systems in which the wavefunction of charge carriers is confined in all the three spatial dimensions. Due to the reduced size of QDs devices—comparable with the de Broglie wavelength of charge carriers—the quantum nature of the orbital degrees of freedom and of the energy of charge carriers is at the heart of

their description. The electronic charge quantization becomes crucial in determining the transport properties of QDs, when the energy scale associated with the addition of a charge carrier into the system dominates over the thermal and quantum fluctuations. Besides, quantum dots allow to individually manipulate single electrons offering the possibility to store and process quantum information [116]. For a review including seminal transport experiments in quantum dots see Ref. [117].

Graphene QDs have triggered great amounts of experimental and theoretical work. In particular, there is large interest in carbon-based QDs to use as *hosts for qubits based on spins* [116] which derives from the expected reduction of the main limitations to obtain long spin-coherence times in semiconductor-based dot systems (as in GaAs), namely, substantial spin-orbit interactions [118, 119, 120] and electron spin interaction with the nuclear spin (hyperfine coupling) [121]. The reduction of the former is due to the lightness of the carbon nuclei ¹³, while the latter is reduced in carbon materials due to the fact that they are formed prevalently by the ¹²C isotope with vanishing nuclear spin [123]. Graphene QDs have also revived the interest in valleytronics [124], which aims to use the valley index to process information. Different schemes have been proposed to govern the valley polarization in graphene [125, 126].

The opportunity to study quantum phenomena in graphene QDs poses new challenges starting from the standard techniques to obtain electrostatic confinement, which is problematic for massless Dirac fermions. Most experimental work on graphene QDs uses graphene flakes to isolate graphene confined devices, their atomic-like properties having been proved by Coulomb blockade [127] and transport through excited states measurements [128, 129]. Beyond the standard spectroscopy tools, the employment of direct techniques as scanning tunneling spectroscopy [130] is facilitated in graphene due to the fact that it is an open surface. Notable experimental efforts are pointing towards disorder minimization which allows to isolate the intrinsic properties of graphene QDs as well as to enhance their control. We review graphene QDs in Section 2.3.4.

2.3.1 Klein tunneling in graphene

The probability of graphene charge carriers to tunnel through a potential barrier does not decrease exponentially with the potential barrier height and width as for non-relativistic particles but is unitary for certain angles independently of the potential barrier drop. This is the Klein tunneling relativistic effect predicted back in 1929 [81], expected to arise at enormous potential barriers of height greater than the electron rest energy. Before graphene, this counter-intuitive effect remained a gedanken experiment until it

¹³the intrinsic graphene spin-orbit coupling is of the order of tens of μeV [122], for broken inversion symmetry the Rashba term contribution is of the same order [119]

was observed in graphene p-n junctions [82, 83] thanks to the fact that there is no a minimal threshold for the potential barrier height required to the effect to take place. The scattering process of massless Dirac electrons is here reviewed by following the arguments of the first predictions in the context of graphene [84]. Consider a massless relativistic electron with energy E approaching the hard-wall potential barrier¹⁴

$$V(x) = \begin{cases} V_0 & \text{for } 0 \leq x \leq D, \\ 0 & \text{for } x < 0 \text{ or } x > D \end{cases} \quad (2.18)$$

from the left, with incidence angle ϕ . The wavefunction $\Phi = (\Phi_A, \Phi_B)$ satisfying the Dirac equation $(-i\hbar v_F \hat{\tau} \cdot \nabla + V(x))\Phi = E\Phi$ can be written as

$$\Phi_{(I)}(\mathbf{r}) = \begin{pmatrix} 1 \\ s e^{i\phi} \end{pmatrix} e^{i(k_x x + k_y y)} + r \begin{pmatrix} 1 \\ s e^{i(\pi - \phi)} \end{pmatrix} e^{i(-k_x x + k_y y)} \quad (2.19)$$

in the region (I) at the left of the barrier ($x < 0$). Here r is the reflection coefficient, $s = \text{sgn}(E)$ and the wavevector—outside the barrier—is $\mathbf{k} = (k_x, k_y) = (k_F \cos \phi, k_F \sin \phi)$, with $k_F = E/s\hbar v_F$ the Fermi wavevector. Note that the y component of the wavevector k_y is conserved and therefore the propagation angle for the reflected wave function becomes $\pi - \phi$. At the barrier the electron wave is refracted. Within the barrier region (II), where $0 < x < D$, by defining $k'_x = \sqrt{(E - V_0)^2/(\hbar v_F)^2 - k_y^2}$, the wavefunction can be written as

$$\Phi_{(II)}(\mathbf{r}) = a \begin{pmatrix} 1 \\ s' e^{i\phi'} \end{pmatrix} e^{i(k'_x x + k_y y)} + b \begin{pmatrix} 1 \\ s' e^{i(\pi - \phi')} \end{pmatrix} e^{i(-k'_x x + k_y y)} \quad (2.20)$$

where $s' = \text{sgn}(E - V_0)$, and $\phi' = \arctan(k_y/k'_x)$ is the refraction angle derived from the conservation of k_y . In the region $x > D$ (III), right to the barrier, the wavefunction is

$$\Phi_{(III)}(\mathbf{r}) = t \begin{pmatrix} 1 \\ s e^{i\phi} \end{pmatrix} e^{i(k_x x + k_y y)}, \quad (2.21)$$

with transmission coefficient t . The continuity condition for the wavefunction at the potential barrier edges $\Phi_{(I)}(x = 0, y) = \Phi_{(II)}(x = 0, y)$ and $\Phi_{(II)}(x = D, y) = \Phi_{(III)}(x = D, y)$ ¹⁵ determine the coefficients a, b, r, t . In particular, in the situation $ss' = -1$, i.e.

¹⁴this hard-wall expression assumes that the edges of the potential smear smoothly with respect to the graphene lattice constant ($\sim 2.42\text{\AA}$) and additionally it is assumed that the scattering does not mix the two graphene valleys.

¹⁵which imposes four equations due to the two-component nature of the wave-function

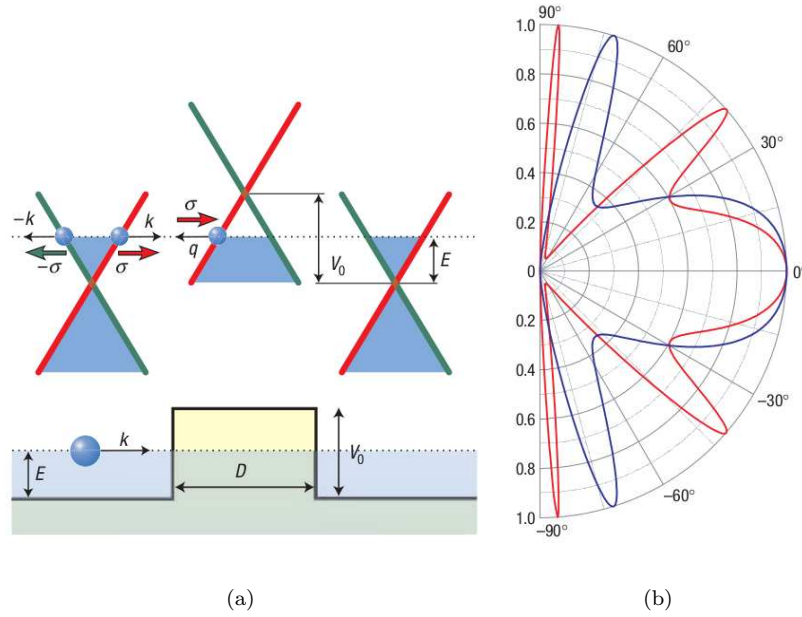


FIGURE 2.4: (a) Dirac spectrum, i.e., wavevector-energy dispersion inner and outer the barriers (top panel). The dotted line indicates the Fermi level. The arrows indicate the direction of the pseudospin (fixed for each branch), which points parallel (antiparallel) to the momentum in the conduction (valence) band. Space-energy diagram (bottom panel). The pseudospin is conserved in the scattering process, the matching between the directions of the pseudospin for particles outside and inside the barrier region leads to unitary transmission. (b) The transmission probability as a function of the incidence angle for two barriers of heights 200 meV (red curve) and 280 meV (blue curve) are compared. The barrier width is $D = 100$ nm. The Fermi energy for incidence electrons is $E_F \approx 80$ meV. Both figures are adapted from Ref. [84].

opposite energy signs inside and outside the barrier region, the transmission probability $T = |t|^2$ depends on the incidence angle ϕ as shown in Fig. 2.4(b). For simplicity it is reported the simplified expression of T in the limit of high barriers $|V_0| \gg |E|$

$$T = \frac{\cos^2 \phi}{1 - \cos^2(k'_x D) \sin^2 \phi}. \quad (2.22)$$

The transmission probability, at any angle, is unitary if the resonance condition $q_x D = \pi n$ with $n = 0, \pm 1, \dots$ is satisfied. This is not peculiar of graphene since in gap-less semiconductors an analogue situation of transparency which depends on tunneling parameters take place. However, for perpendicular incidence $\phi = 0$, the barrier is transparent *independently* of tunneling parameters, this is peculiar of graphene charge carriers with definite helicity. As a consequence of Klein tunneling, the mobility of electrons in graphene is high [131] regardless of being exposed to the environment that provides many scattering centres providing the conditions to create ballistic devices. Besides, Klein tunneling implies that graphene charge carriers cannot be confined by electrostatic gating as in conventional semiconductors except under particular circumstances

as the presence of a mass gap in the energy spectrum [132], or in geometries excluding normal incidence [133].

2.3.2 Sublattice-induced symmetry breaking and band-gap opening in graphene

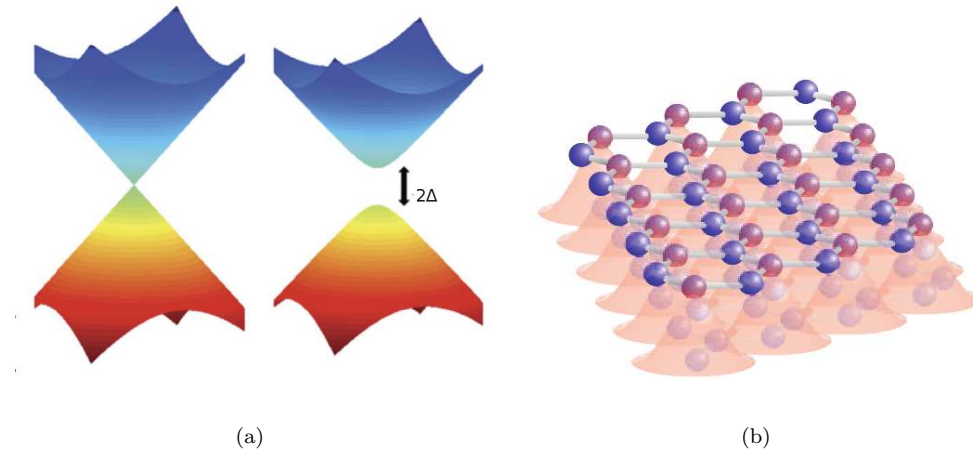


FIGURE 2.5: (a) Different mechanisms can modify the Dirac cone of pristine graphene (left) into a gapped spectrum (right). Figure adapted from Ref. [109]. (b) The breaking of the graphene sublattice symmetry opens a band gap in the graphene spectrum, which is caused by a commensurate potential that may be induced by a periodic substrate. Figure adopted from Ref. [134]

Pristine undoped graphene presents a linear gapless spectrum (see Section 2.2.2) and metallic conductivity also at (nominally) zero carrier concentration. The opening of an energy gap in the graphene spectrum (see Fig 2.5(a)), i.e., a finite energy difference between the the top of the valence band and the bottom of the conduction band at the Dirac points, represents an important technological challenge. In fact, an energy gap provides a conductance pinched-off mechanism in view of electronic applications such as digital transistors or sensors [134]. Besides, a band gap inhibits the coupling between electron and hole states, suppressing Klein tunneling [135], and enabling the electrostatic confinement of charge carriers. Many mechanisms can, in principle, give rise to a band gap, e.g., the spin-orbit coupling [122] opens a very small gap in the spectrum of graphene which can be enhanced by adatom doping [10]. Mechanical or chemical interventions in graphene, as strain engineering [136, 137] or absorption of molecules [138], and even the action of an infra-red laser beam [139] have been proposed beyond others.

The topical (open) challenge is that the mechanism should induce a sufficiently wide gap¹⁶ by retaining a good compromise with graphene transport quality. Two viable

¹⁶estimations suggest that for digital logic applications, on-off ratios of 10^6 in a field effect transistor (FET), a gap in the range 360 – 500 meV is needed [140]

approaches to open a band gap, relying on size quantization and the breaking of sublattice symmetry [63], employ the effect of confinement [128] and the effect of a periodic substrate [59, 132] respectively. In this latter proposal [141], the presence of a substrate induces a staggered potential in the atomic scale (see Fig. 2.5(b)), the amount of the gap depending on the substrate-graphene interaction. Different substrates have been proposed to fulfil this task as Au/Ru(001) [142], MgO [143], silicon carbide (SiC) or hexagonal boron nitride (h-BN). These two last semiconductor substrates have attracted a great deal of attention. It is possible to obtain graphene of high quality on them, in particular of high mobility [52, 89], so they have been extensively used as gate dielectrics for graphene-based devices. These substrates have been the platform of interesting fundamental discoveries in graphene.

The advantages of the use of SiC as a substrate, on which graphene is directly grown, with scalable techniques as the furnace growth¹⁷, assuring high quality graphene, are discussed extensively in Ref. [144]. Graphene can be grown over the silicon or the carbon face of the different SiC polytypes, the carbon face being preferred as there the graphene mobility is higher. Graphene on SiC is mostly stacked in a AB-manner when grown over the carbon face of SiC, which is called "buffer layer" since it is electronically inactive. In the AB-stacking the carbon atoms of graphene are alternatively above a substrate atom. It has been observed, through ARPES, a deviation from the conical dispersion in the energy spectrum of graphene grown on 6H-SiC (over the carbon phase), attributed to a band gap of about 260 meV, induced by sublattice symmetry breaking [145]. It needs to be considered that graphene on SiC is heavy n-type doped so that the Fermi level does not fall within the gap. However, the deviation from the conical dispersion observed through ARPES has been the subject of an intense controversy between the band gap interpretation [146] and the explanation of the observed feature at the Dirac points in terms of electron-plasmon interaction [28, 147]

Some of the appealing characteristics of the use of h-BN as a substrate are, beyond the very high carriers mobilities [89], the low carrier inhomogeneities¹⁸ and the high stability of graphene on h-BN, due to the planar h-BN structure [149]. The lattice constant mismatch between the h-BN and the graphene lattices is of $\approx 1.8\%$ [132], giving rise to moiré patterns for graphene not in registry with the substrate. The band gap of graphene on h-BN is linked to the commensurate alignment—no signs of a gap from transport measurements have been found in random crystallographic orientation [150, 151]. Due to the mismatch between graphene and h-BN lattices and due also to misalignment of the respective crystal axes, the sublattice potential might average out

¹⁷consisting on the inductive heating of SiC fragments enclosed in a graphitic chamber

¹⁸almost 1 order of magnitude lower than graphene on SiO₂. Comparison with SiO₂ is made since it is the substrate in which graphene has been first isolated [148]

on a large scale. Yet more recent experiments show that this is not necessarily the case [89]. The band has been estimated from transport measurements in approximately 30 meV [89, 152], and 38 meV from optical spectroscopy [109]. The precise mechanism behind the opening of a band gap in h-BN is still under investigation [89, 153], recent theoretical results [154] suggest how to control the band gap magnitude.

Formally, the conical Dirac points are protected, individually, from translational invariant perturbations conserving the inversion symmetry $H_K = \hat{\tau}_1 H_{K'} \hat{\tau}_1$ and the—so called true—time reversal symmetry [155] (linking the two valleys) $H_K = H_{K'}^*$, i.e., preserving the condition $H_\tau = \hat{\tau}_1 H_\tau \hat{\tau}_1$ for the single Hamiltonian in each valley $\tau = K, K'$ [156]. A constant potential difference between the A and B sites of graphene, as induced by a periodic substrate, breaks the inversion symmetry (by preserving the true time reversal symmetry) and it is accounted, in Hamiltonian of each single valley (see Eqs. 2.9 and 2.10) by a diagonal term $\Delta \hat{\tau}_3$, which acts as a mass term, differentiating the two sublattice components. The energy spectrum therefore becomes $E = \pm \sqrt{(\hbar v_F k)^2 + \Delta^2}$ in both valleys. It is characterized by an energy gap of 2Δ , as shown in Fig. 2.5(a).

2.3.3 Single-electron tunneling spectroscopy

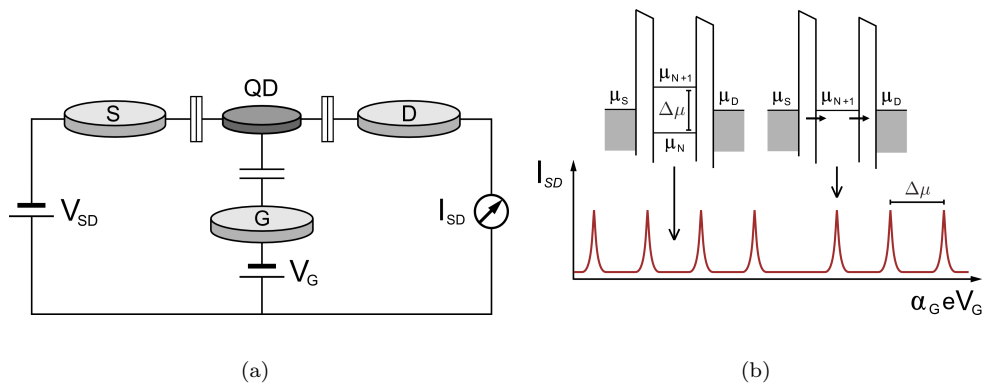


FIGURE 2.6: (a) Quantum dot device for electronic transport. The QD is tunnel-coupled with electrodes source (S) and drain (D) which are the charge carrier reservoirs. The capacitively-coupled gate electrode (G) modulates the chemical potential of the dot respect to the leads. (b) Coulomb-blockade resonances in the linear response regime. Insets: energetic situation in the source, drain and dot for the system in Coulomb blockade (left inset) and resonant transport (right inset)

Experimental transport data can access the QD electronic properties, which are determined by the interplay between the energy scales dictated by the electron-electron interaction and the confinement energy. In a tunneling spectroscopy experiment the QD is coupled through tunnel barriers with source (S) and drain (D) conducting leads, which are the reservoirs of charge carriers. The coupling with the leads is weak so that the

QD is almost an isolated system with an integer number of electrons N . A bias voltage $V_{SD} = V_S - V_D$, applied between source and drain, allows for transport within the bias (energy) window $\mu_S - \mu_D = -eV_{SD}$. Indeed, electrons tunnel through the QD available states inside the bias window from one conducting lead to the other, in order the current to flow. At a given bias voltage, it is possible to electrostatically modulate the number of available states in the QD within the bias window, by coupling the QD with a gate electrode (G) that therefore controls the current flow. The tunnel junctions related to the S (and D) lead has capacitance C_S (and C_D) and conductance $\mathcal{G}_S = 1/\mathcal{R}_S$ (and $\mathcal{G}_D = 1/\mathcal{R}_D$), while the gate electrode (with C_G) is capacitively coupled to the QD, i.e., $\mathcal{G}_G = 0$. This basic set-up to perform transport spectroscopy is illustrated in Fig. 2.6(a)

The defining properties of QDs, i.e., the quantization of the charge and of the energy spectrum, are considered in the simplest way by the constant capacitance model. Two major assumptions are at the basis of this model, which is adapted from the description of a metallic island. First: the interactions between charge carriers in the QD and with the environment, can be accounted by a constant capacitance. Second: interactions do not affect the single-particle energy spectrum [157]. The dot ground-state energy is given by

$$E_0(N) = \epsilon_N(B) + E_C N^2 - e \sum_l \alpha_l V_l N. \quad (2.23)$$

The first term is the energy of the (discrete) lowest occupied single-particle orbitals, which are determined by the confinement geometry and eventual presence of a magnetic field B and are filled in accordance with the Pauli principle, n -fold degeneracies being accounted by counting one level n times. The second and third terms include the electrostatic energy contributions¹⁹ arising from the addition of a quantized charge to the dot $E_C = e^2/2C$ (the charging energy) and from the voltages applied to the leads. $C = \sum_l C_l$ is the dot total capacitance, with $l = S, D, G$. This expression for the dot capacitance generalizes to a greater number of electrodes that can be used to locally tune the electrostatic energy. In the last term, the so-called level arms, $\alpha_l = C_l/C$ are dimensionless coupling parameters that relate the voltage in the corresponding lead to the induced potential in the dot. The electrochemical QD potential, i.e., the minimum energy required for loading the N th electron to the dot, is given by

$$\mu(N) = E_0(N) - E_0(N-1) = \epsilon_N - \epsilon_{N-1} + E_C(2N-1) - e \sum_l \alpha_l V_l \quad (2.24)$$

which is the difference between the ground-state energies in subsequent charge states. If the antisymmetric condition $V_S = -V_D$ is assumed, then $\mu(N)$ is independent from

¹⁹the total electrostatic energy is given by $\int_0^Q dQ(Q + \sum_l V_l C_l)/C$ where $Q = -eN$ is the quantized charge in the dot and the second term is the electrostatic potential difference between the dot and the reservoirs

the bias voltage V_{SD} .

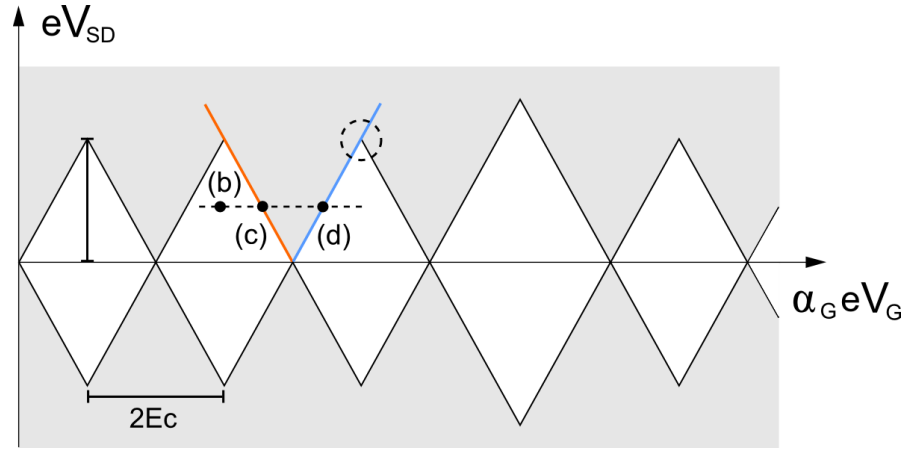
The same result for the chemical potential of Eq. 2.24, for large electron numbers and limited variations of the applied voltages, is obtained from the constant interaction model [117, 157, 158] based on the Hartree-Fock approximation for the dot N -electron system, assuming negligible exchange interactions, constant level arms and that the charging energy per electron does not depend on the electron number [112]. Despite the severe approximations at the basis of this simple model, this is a widely used starting point for the interpretation of transport experiments. First deviations can be accounted by considering variations of the capacitances and the level arms on the electron number or on the applied voltages.

Measurements in the linear response regime are performed by fixing a small transport window—smaller than the single-particle level spacing and than the charging energy—within which the current I varies linearly with V_{SD} . The conductance I/V_{SD} is measured as a function of the gate voltage V_G , that controls the dot electrochemical potential levels μ respect to μ_S and μ_D . For positive V_G , the ladder of dot electrochemical potentials is lowered proportionally to the V_G increase, see Eq. 2.24. Conductance resonances are registered whenever the electrochemical potential of the QD is aligned with the ones of source and drain $\mu_S \approx \mu(V_G) \approx \mu_D$, allowing for resonant transport (the energy landscape is depicted in the right inset of Fig. 2.6(b)). Between the peaks, the conductance is suppressed. The reason for blockade transport can be visualize from the energy landscape shown in the left inset of Fig. 2.6(b), for a dot filled with N electrons. Indeed, in such voltage configuration, the energy required to load the $N + 1$ th electron into the QD is greater than the energy gain of removing it from the source lead, i.e. $\mu_{N+1} > \mu_S$. This condition of blockade transport due to charging effects—Coulomb blockade [159]—is lifted alternatively by tuning μ by V_G , giving rise to a series of peaks in the conductance, as depicted in Fig. 2.6(b), each peak corresponding to the tunneling of a single electron. Coulomb blockade is accessible at low enough tunneling conductance such that the charge quantization in the QD becomes distinct, i.e. for $\mathcal{G}_{S/D} \ll e^2/h \approx (26k\Omega)^{-1}$ ²⁰, and at low enough temperatures $k_B T \ll E_C$ (here k_B is the Boltzmann's constant), so that the charging energy becomes resolvable beyond thermal fluctuations. Moreover if $k_B T < \Delta\epsilon$, with $\Delta\epsilon$ the single-particle level spacing, then also $\Delta\epsilon$ is resolvable, and transport involves only one quantized energy level per conductance resonance—this is the single-level transport regime [112]. The separation between the conductance peaks is the addition energy

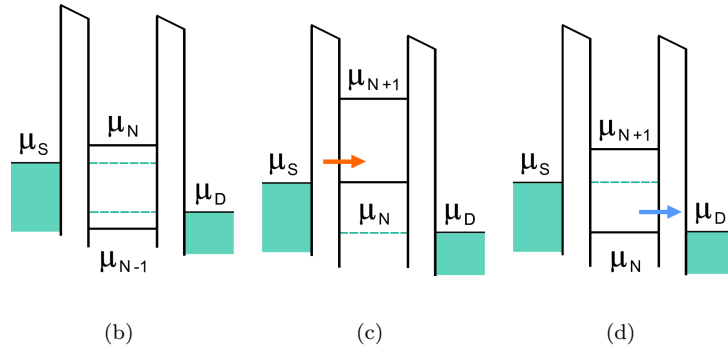
$$\Delta\mu(N) = \mu(N + 1) - \mu(N) = 2E_C + \Delta_N = ea_G\Delta V_G \quad (2.25)$$

²⁰this condition is deduced from the Heisemberg's uncertainty relation $\Delta E \Delta t > h$ relating the uncertainty over the RC-time for an electron to tunnel between the QD and the leads $\Delta t \approx C/G$ and the energy uncertainty, by the demand that the latter is less than the charging energy, i.e. $\Delta E < E_C$

with $\Delta_N \equiv \epsilon_{N+1} - 2\epsilon_N + \epsilon_{N-1}$. The addition energy is the energy amount that needs to be overthrown in order the $(N+1)$ th electron to tunnel into the dot filled with N electrons. From the last expression in Eq. 2.25 it is clear that the gate coupling constant α_G is required in order to determine $\Delta\mu$, which is not possible from a two terminal set-up measurement.



(a)



(b)

(c)

(d)

FIGURE 2.7: (a) Stability diagram scheme, the conductance vanishes within the white areas—due to Coulomb-blockade—while is finite in the gray areas. The addition energy is readable both from the width and from the height of the Coulomb diamonds. Along the dashed line, the Coulomb blockade condition (b) is lifted by increasing the gate voltage, transport persists from the $\mu = \mu_S$ (c) to the $\mu = \mu_D$ (d) resonant conditions.

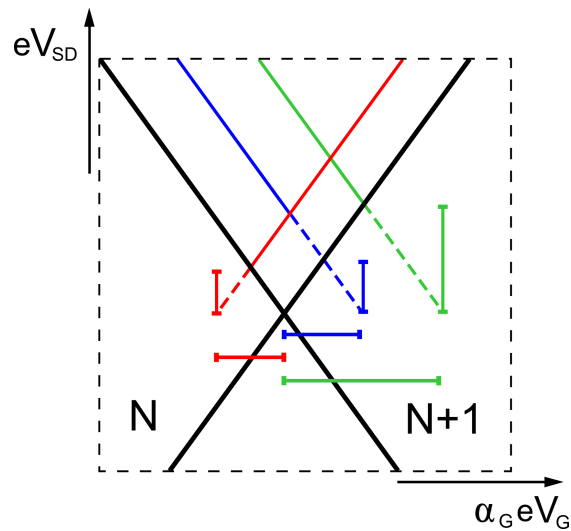
Opening the bias window $-eV_{SD}$, the system enters the non-linear transport regime. Measurements of the conductance are in general given in the form of stability diagrams, displaying its dependence on both the gate voltage and the bias voltage, as schematically illustrated in Fig. 2.7(a). From the stability diagrams, the level arms can be determined and the addition energy is directly legible. This transport regime allows to access also the QD excitation energies. In Fig. 2.7(a), for the set of (V_{SD}, V_G) inside the white areas, the so-called Coulomb diamonds, transport does not take place due to Coulomb-blockade. The potential diagram of this regions, for which the number of electrons in the dot fixed,

is schematized in Fig. 2.7(b). At zero bias voltage, the linear-response conductance resonances (Fig. 2.6(b)) correspond to the vertexes of the Coulomb diamonds in Fig. 2.7(a), separated by the addition energy given by Eq. 2.25. Starting from the vertexes of the Coulomb diamonds at zero-bias, by increasing the bias window, the regions of finite conductance—shaded regions in Fig. 2.7(a)—enlarge, since the transport condition $\mu_D \leq \mu(N, V_G) \leq \mu_S$, i.e., that at least one QD electrochemical potential falls within the bias window, is met for a range of V_G proportional to the bias voltage. At the edges of the Coulomb diamonds, the electrochemical potential of the dot is aligned with the source $\mu(N) = \mu_S$ (left-red boundary) or drain $\mu(N) = \mu_D$ (right-blue boundary) chemical potentials as depicted in the corresponding diagrams of Figs. 2.7(c) and 2.7(d). The boundaries of the shaded regions departing from neighbour conductance resonances at zero bias intersect, e.g., $\mu(N, V_G) = \mu_D$ intersects $\mu(N+1, V_G) = \mu_S$ at the encircle point in Fig. 2.7(a), corresponding to a bias voltage such that $\mu(N+1, V_G) - \mu(N, V_G) = eV_{SD}$. Therefore the addition energy is readable both from the width $\alpha_G e \Delta V_G$ and from the height eV_{SD} of the Coulomb diamonds, and the gate level arm is $\alpha_G = V_{SD} / \Delta V_G$.

Consider the case of a dot with charging energy comparable with the single-particle energy level spacing, supposed to be constant. The structure of the resonance peaks in the linear-response regime display a periodicity resembling the n -fold degeneracy of the orbital levels. n conductance peaks, separated by $2E_C$ are followed by the $(n+1)$ th peak, separated by $2E_C + \Delta\epsilon$. This structure is also reflected in the stability diagrams as a series of n diamonds of equal weight $2E_C$, followed by a diamond of greater weight $2E_C + \Delta\epsilon$. This sequence is depicted for four-fold degeneracy in Fig. 2.7(a), as expected for graphene quantum dots with two-fold orbital degeneracy arising from the valley degree of freedom in addition to the (conventional) two-fold spin degeneracy. If the single-particle level spacing is negligible respect to the Coulomb repulsion, the peak spacing (the diamonds weight) is expected to be roughly constant as it is determined only by the charging energy.

Energy spectroscopy of the excited-states can be performed for a sufficient wide transport (bias) window, greater than the excitation energy of the QD. Incoherent transport of single-electrons through the excited-states of the QD, is the dominant mechanism when the coupling with the leads is weak and the states in the QD are not degenerate. In this situation, in measurements of the differential conductance (sketched in Fig. 2.8), transport through excited-states appear as parallel lines to the Coulomb diamonds edges. This type of transitions are energetically allowed only outside the Coulomb diamonds, when an excited-state chemical potential falls within the bias window [157]. The electrochemical potential for the i th excited state with energy $E_i(N)$ is defined as

$$\mu_i(N) = E_i(N) - E_0(N-1) \quad (2.26)$$



(a)

FIGURE 2.8: (a) Stability diagram scheme. The differential conductance is plotted in the $(eV_{SD}, \alpha_G eV_G)$ plane. The black lines are the edges of Coulomb-blockade diamonds (Fig. 2.7(a)), i.e., correspond to transitions among ground-states. The red and green lines are transitions between excited-states and the ground-state corresponding to the black line parallel to them. The blue resonance corresponds to a transition between two excited-states. The chemical potentials related to excited-states transitions are indicated by scale-bars.

which is the energy involved in the transition from the $N - 1$ ground-state to the N electron i th excited-state. The chemical potentials related to excited state transitions—and therefore the excitation energies—can be extracted from the stability diagram (sketched in Fig. 2.8) either in the bias voltage axis, from the intersection of the resonance with the Coulomb diamond edge (vertical scaled-bar), or in the gate voltage axis by extrapolating the resonance line to zero bias voltage (horizontal scale-bar). Transitions between excited-states, involving the generalized chemical potential $\mu_i(N) = E_i(N) - E_j(N - 1)$ between the i th and the j th excited states in the N and $(N - 1)$ charge states, correspond to resonances ending in the trace of the initial excited-state as exemplified by the orange line in Fig. 2.8. This process, which takes place for tunneling rates greater than the relaxation rates, provides information about the relaxation rates of the QD levels [157] and gives further access to the low lying excitation energies. The above discussion is restricted to single-electron tunneling processes only, omitting higher order processes involving more than one tunneling event as well as deviations from the basic features. In this thesis it will be shown the importance of Coulomb interactions in graphene quantum dots through an accurate treatment of electron-electron interaction with respect to the simple model presented here, based on the solution of the many-body problem. Results will provide predictions for quantities accessible through tunneling spectroscopy.

2.3.4 Towards cleaner graphene quantum dots

The first generation of graphene quantum dots appeared simultaneously with graphene insulation [148] in the form of graphene nanoflakes, obtained by mechanically cutting (etching) graphene. The etching technique has been largely developed and is widely used to obtain 0-dimensional and 1-dimensional structures from graphene. In these structures, the opening of a gap is provided by space quantization. Clear Coulomb blockade was demonstrated [127] in etched graphene QDs, once the control over the tunneling constrictions had been improved by using graphene lateral gates. Extensive studies on

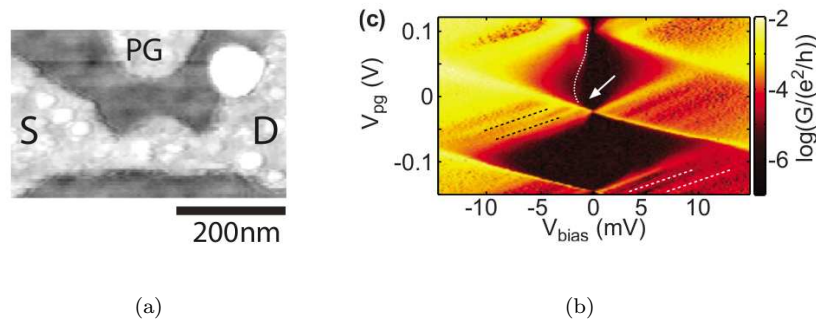


FIGURE 2.9: Confinement in etched graphene QDs (a) Atomic force micrograph of a graphene QD obtained through mechanical exfoliation of graphite. The dot size is 140 nm. The transport set-up is made of graphene constrictions connecting the dot to source (S) and drain (D) leads, transport is controlled by a plunger gate (PG) and a back gate (not shown) gate. (b) Measured stability diagram of the dot shown in panel (a). Excited-states (dashed-lines) are visible as resonances outer the Coulomb diamonds and confirmed by the finite conductance in the upper diamond, interpreted as a co-tunneling event (arrow). Figures adapted from Ref. [129].

the transport properties of etched graphene QDs (nano-flakes) of different sizes, showed the first signatures of transport through excited states [128], that were confirmed by the observation of inelastic co-tunneling events [129](see Fig. 2.9). In these devices, the graphene Landau levels (see Subsection 2.2.3) have been observed—for large perpendicular magnetic field—in the pattern displayed by the energy levels [129], and the zero-energy characteristic graphene Landau level, has been identified [160], marking the crossover between electron and hole states. The Zeeman splitting of spin states in an in-plane magnetic field has been monitored in conductance measurements, providing an estimation of the g-factor²¹ and a spin filling sequence compatible with comparable Coulomb interaction and confinement energy scales has been extracted [161]. The charge relaxation times of electronic excitations have been also reported²² [162]. In spite of these achievements, the detailed investigation of the energy spectrum of etched graphene

²¹the g-factor was evaluated to be ≈ 2 from the Coulomb peak spacing as a function of the parallel magnetic field in transitions between successive spin ground states [161]

²²the extracted charge relaxation times is 5-10 longer than on III/V semiconductor-based quantum dots [162]

QDs is often limited by extrinsic effects such as the presence of localized states in the constrictions, among others. Recent advances in identifying the intrinsic properties of etched graphene QDs have employed three-terminal set-ups which allow for the discrimination between the dot and the leads wave functions [163]. In etched graphene quantum

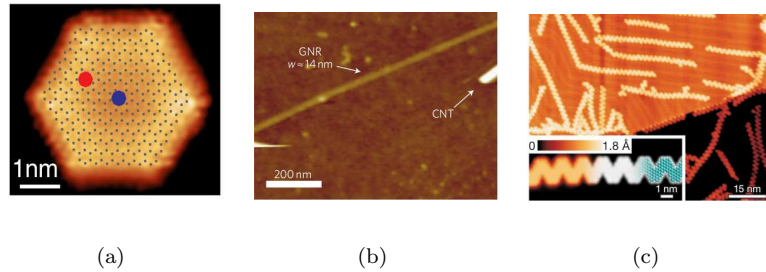


FIGURE 2.10: Atomically precise nano-structures with controlled edges, obtained through different techniques. (a) Scanning tunneling microscopy (STM) image of a hexagonal QD obtain by the chemical vapor deposition method (adopted from Ref. [164]) (b) Atomic force microscopy (AFM) image of a graphene nano-ribbon obtained by unzipping a carbon nanotube (adapted from Ref. [18]) (c) STM of a nano-structured chevron ribbon obtained through bottom-up fabrication and superimpose DFT simulation (grayscale) (adapted from Ref. [165])

dots [15], the class of graphene QDs most studied up to now, an important role in determining the electronic properties is played by the edges terminating the flakes that can be of armchair, zigzag or—predominantly—a combination of both geometries. Atomically sharp edges give rise to localized edge states dominating the electronic structure, except for perfect armchair orientation [46]. Therefore, it is a hurdle that the etching fabrication techniques lead to rough edges, rendering crucial edge-disorder in determining the transport properties of etched graphene confined devices²³. This issue was addressed by the chemical vapor deposition (CVD) growth of graphene QDs on metal substrates [164]. In this type of graphene QDs the local density of states (LDOS) has been investigated by scanning probe methods, an example of an hexagonal nano-structured dot with zig-zag edges on a Ir(111) substrate being shown in Fig. 2.10(a). The CVD technique leads to soft-confinement [130] due to the strong edge-substrate interaction. Many other techniques have been devoted to the fabrication of nano-structures with controlled sharp edges as, e.g., the unzipping of carbon nanotubes [18] (see Fig. 2.10(b)) and the bottom up approach [46, 165], that—changing the paradigm—enables for atomically precise design of edges (see Fig. 2.10(c)). An important source of disorder in addition to edge disorder is the inhomogeneous doping caused by the—widely used—silicon-oxide SiO₂ substrate. The reduction of bulk disorder can be tackled by designing architectures based on suspended graphene, or by the employment of a different substrate, such as hexagonal boron-nitride that retains the mechanical and electronic graphene prominent

²³for a comparative discussion in the role of edge disorder see Ref. [51]

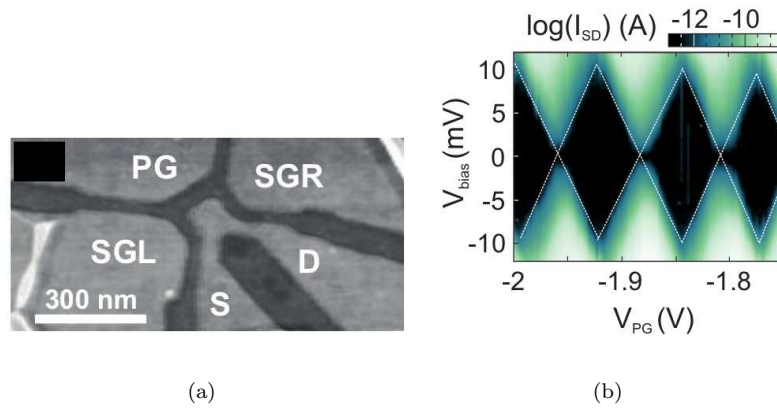


FIGURE 2.11: Bulk disorder is reduced in new-generation graphene QDs. (a) Scanning force micrograph of an etched graphene QD on h-BN substrate. The QD diameter is 110 nm. (b) Stability diagram of the device shown in panel (a). From the Coulomb diamonds, the extracted charging energy is $E_C \approx 8 - 10$ meV. Both figures are adapted from Ref. [21].

characteristics. Even though the first solution seems not to be feasible in graphene due to difficulty to gate suspended graphene layers [160], first transport measurements in alternative substrates (see Fig. 2.11) have been recently performed [21, 51, 52]. Both

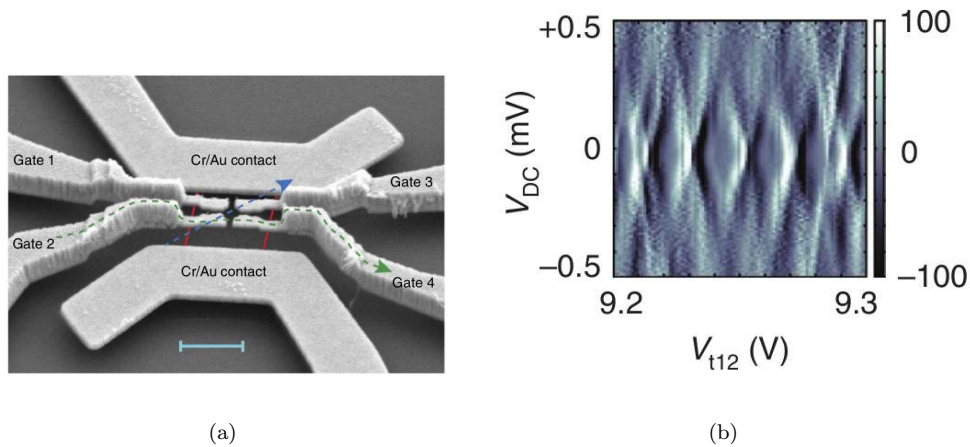


FIGURE 2.12: Reduction of bulk and edge disorder in bilayer graphene QDs (a) Scanning electron micrograph (SEM) image of the architecture holding a suspended bilayer graphene QD electrostatically confined. The bilayer (not visible) is placed below the top gates in correspondence to the red boundary. The scale bar marks $1 \mu\text{m}$. (b) Stability diagram of the device in panel (a). The conductance is given in units of e^2/h , as a function of the DC voltage V_{DC} through the device and the voltage on two top gates V_{t12} . The extracted charging energy is $E_C \approx 0.4$ meV. Both figures are adopted from Ref. [48]

approaches have been successfully employed to obtain electrostatically confined bilayer graphene QDs [48, 49], where the energy gap—provided by the breaking of the inversion symmetry—has the advantage to be controllable through a perpendicular electric field.

An example of a complex architecture for clean bilayer graphene QDs and the relative transport results is shown in Fig. 2.12. These proof-of-concept experiments pave the way to the next generation of highly tunable graphene quantum-confined devices, exploiting alternative ways to obtain a band gap and based on clean confinement as offered by patterned electrostatic gates. Such progress is highly desirable as it lifts the main limitations to investigation, and thus to control graphene QDs properties. Among the opportunities for fundamental research which this experimental trend proposes, being particularly relevant for this Thesis, the question of how electron-electron interactions in clean graphene QDs modify the non-interacting energy spectra is addressed.

Chapter 3

Wigner localization background

The Wigner localization concept is introduced as it is the subject of the original contributions of the Thesis in Chapters 5 and 6. First we review Wigner localization in the bulk, emphasizing the differences between graphene and the conventional two-dimensional electron gas. We then discuss both theoretical and experimental works on Wigner molecules in finite systems.

3.1 The Wigner crystal

The Wigner localization phenomenon, which is a paradigmatic example of strong electron correlation, has been extensively explored since its prediction [36]. In a conventional two-dimensional (2D) homogeneous electron gas¹, in the absence of disorder, the Fermi liquid [166] ground state—whose wavefunction is delocalized over the whole system size—undergoes a phase transition as the density is decreased becoming a strongly correlated state of localized electrons known as Wigner crystal (WC). This occurs because, by decreasing the electron density n_e , the ratio between the average Coulomb interaction energy $\langle C \rangle$ to the average kinetic energy $\langle E \rangle$, known as coupling constant, increases as²

$$r_s \equiv \langle C \rangle / \langle E \rangle = 1/a_B \sqrt{\pi n_e}, \quad (3.1)$$

where $a_B = \hbar^2 \varepsilon / m e^2$ is the Bohr radius, written in terms of the static dielectric constant of the host material ε , and the electron effective mass m . The coupling constant coincides, at zero magnetic field, with the average interparticle separation explicated in Bohr radius units known as Brueckner or Wigner-Seitz dimensionless density parameter. The scaling between competing energies (Eq. 3.1) derives from the charge carrier quadratic

¹in a background made of neutralizing positive charges

²in the presence of valley degeneracy g_v the density parameter is rescaled as $g_v r_s$

dispersion relation $E_k = \hbar^2 k^2 / 2m$ at small momenta k , that implies an average kinetic energy proportional to n_e as compared with the average Coulomb interaction energy scaling as $n_e^{1/2}$. Therefore at low densities, where the interaction dominates, the localization of electrons among lattice positions minimizes the total energy of the electron system. As a matter of fact, the 2D electron system is predicted to form a triangular lattice. The critical value of $r_s \approx 37$ has been estimated³ for a clean two-dimensional electron gas (2DEG) to transform into an electron-solid [167]. The melting of the crystal at zero temperature is driven by quantum fluctuations, i.e., the oscillatory motion of the electrons about their lattice equilibrium positions [168]. Experimentally the WC has been observed on the surface of liquid He [169], in GaAs/GaAlAs heterojunction [170] and in Si [171]. A recent theoretical and experimental review on the 2D Wigner crystal can be found in Ref. [168].

In graphene, in contrast with the conventional two dimensional electron gas (2DEG), the ratio between the interaction energy to the kinetic energy is independent of the electron density, this peculiarity arising from the linear dispersion relation of graphene charge carriers $E = \pm \hbar v_F k$ near to the Dirac points. In fact, while the average Coulomb energy is, as in 2DEG, proportional to $n_e^{1/2}$, in graphene also the average kinetic energy scales the same way so graphene coupling constant is ⁴

$$r_s = \frac{e^2}{\hbar \varepsilon v_F}. \quad (3.2)$$

Thus the only tunable parameters to drive Wigner crystallization are the dielectric constant ε and the Fermi velocity v_F . Therefore, the interaction parameter in graphene has an upper bound corresponding to the vacuum ($\varepsilon = 1$), providing $0 \leq r_s \leq 2.2$. In the presence of a typical low screening substrate as SiO₂, when $\varepsilon = (\varepsilon_{\text{SiO}_2} + 1)/2 \approx 2.5$, the interaction parameter in graphene is $r_s \approx 0.8$. Even in the limit case of minimum value of $\varepsilon = 1$, which means no screening, the value $r_s = 2.2$ is too small to drive localization. Therefore undoped graphene, in the absence of a magnetic field, is a weakly interacting system in comparison to the conventional 2DEG [9] and Wigner localization is not expected for any electron density [34].

In the presence of a perpendicular magnetic field, Wigner crystallization is favoured due to the fact that the magnetic field effectively localizes the electron wavefunctions while the quantized kinetic energy is controlled as the electrons occupy the highly degenerate Landau levels (LL). For the electrons within the last partially filled LL, the kinetic energy is quenched and the only energy scale is the Coulomb energy, which favours the formation of an electron crystal at small filling factors. In the limit of strong magnetic fields, at

³through Monte Carlo [167] and analytic calculations

⁴this expression does not take into account the spin and valley degeneracies

any density, the minimization of the energy of the system becomes equivalent to the problem of finding the ground state of classical charged particles. The possibility to drive Wigner crystallisation through a magnetic field [172] has been exploited experimentally in the attempt to access it in semiconductor heterostructures, where magneto-transport measurements have showed that at low filling factors the ground state is a Wigner crystal [173].

Graphene ground state, in the presence of a perpendicular magnetic field that quenches the kinetic energy, has been predicted to undergo crystallization. Such predictions, relying on mean field calculations [174], expect a triangular Wigner crystal structure for small non-integer filling factors and an anisotropic Wigner crystal for increasing filling factors [174]. Up to now, the whole experimental evidence of the electron solid is indirect, being based on transport measurements. We note that in graphene the electron density is directly accessible through local probes in contrast to the 2DEG in semiconductor heterostructures where the electrons are buried inside the substrate. Thus the first direct evidence of the WC electron-density modulations might be accessible in graphene. In view of possible comparison with local probe experiments, the local density of states (LDOS) and density of states (DOS) of the graphene electron solid for different filling factors have been investigated [175].

3.2 The Wigner molecule

In finite-size systems the broken translational symmetry is expected to favour localization of electrons respect to the corresponding bulk systems [41]. In analogy to the Wigner crystal in bulk, the strongly correlated state of localized electrons in finite-size systems is known as Wigner molecule (WM). Electron correlation in QDs becomes important when the inter-particle distance is large with respect to the single-electron wave function extension. This relation can be controlled both by diluting the QD population thus increasing the former term, or by applying a magnetic field, which decreases the latter term. The crossover from a weakly interacting regime, dominated by quantum mechanical confinement, to the Wigner-type behaviour, dominated by the interaction, as well as the nature of this behaviour have been investigated extensively in semiconductor quantum dots through different methods. A discussion of the various techniques can be found in Ref. [41]. The degree of localization of electrons in space can be analyzed theoretically through the one- or two-particle densities and the crossover between Fermi liquid and Wigner molecule can be characterized by the dependence of these quantities on quantum degrees of freedom. For example, as the limit case of classical point charges

is approached, the dependence of observables on spin degrees of freedom vanishes. Because of artificial spatial symmetry breaking, the use of mean field methods has to be regarded with some caution since no symmetries are broken in small quantum systems [176, 177]. Another way to search for the WM state is to look at the low-lying excitation spectrum, which in the strongly localized regime deviates from the atomic-like spectrum and consists on spin, rotational, vibrational and isomeric⁵ molecular excitations. Exact diagonalisation (see Section 4.2) allows to take into account all the correlations characterizing the WM and to predict the excitation spectra of the WM state. However, the isomeric configurations and melting mechanisms at high particle numbers need to be tackled through more flexible techniques dealing with greater numbers of electrons.

Different criteria for the onset of the electron localization—a smooth crossover—have been used depending on the kind of confinement under consideration. In contrast to homogeneous systems, where the Wigner-Seitz dimensionless density parameter r_s is defined in terms of the homogeneous density, for few-electron quantum dots it is not straightforward to define an overall density, thus the parameter r_s has been defined in different ways by authors. For example it has been determined numerically from the first maximum of the two-particle correlation function in effective Bohr units [178]. In parabolic quantum dots, it is widely used directly the dimensionless coupling constant tuning the Coulomb interaction $l = l_0/a_B = (e^2/\epsilon l_0)/\hbar w_0$, with $l_0 = \sqrt{\hbar/w_0 m}$ the harmonic oscillator length unit (in terms of the harmonic oscillator frequency w_0). Also, it has been used $r_s = (l^4/\sqrt{N})^{1/3}$ [179], and in analogy with macroscopic systems $r_s = (2l^4)^{1/3}$ [180]. For polygonal QDs $r_s = \sqrt{A/\pi N}$ with A the polygon area [181]. This have to be regarded when comparing different works.

Early theoretical studies [182] of two-particles confined in small boxes found signatures of Wigner localization in the electronic structure and in the spatial correlation function. It was pointed out that correlation dominates for large box dimensions and is more important for narrow rectangular boxes than for square boxes. Electron localization has been investigated in polygonal QDs, without rotational symmetry. The continuous problem of interacting electrons in this geometries has been mapped on a lattice model [183]. More recent studies, based on spin density functional calculations, have shown that increasing the size of polygonal dots the electron densities display as many maxima as the number of electrons for sufficiently weak confinement [181]. The Wigner localization in a hard-wall potential has been recently interpreted in analogy with the hybridization among atomic orbitals [184].

Several theoretical works are dedicated to the WM in QDs with isotropic parabolic confinement potential, widely used to model the diverse confining experimental set-ups.

⁵transitions between diverse geometrical arrangements of electrons

In this case the Wigner molecule electronic configurations consist of a number of spatial shells, which depends on the electrons number, and correspond to the arrangement of particles on concentric circles [180]. Path-integral Monte Carlo simulations for up to eight electrons monitored the crossover towards the WM through the dependence of the two-particle correlation function on the z-component of the total spin. The crossover was found at high densities respect to the bulk at $r_s \approx 4$ [178]. Analogous investigations for higher interaction and higher electron numbers indicated that the localization proceed in two steps: formation of radial shells followed by the freezing of inter-shell rotation [180]. This has been confirmed by successive works investigating the intermediate regime of localization—through diffusion quantum Monte Carlo technique—proposing it as an enhancement of non-interacting interference effects [185]. The close-shell structure of the addition spectra in the non-interacting regime is lifted due to the interaction and affected mainly for small electron numbers [186].

In the deep Wigner limit, the electron molecule is amenable to comparison with the classical picture describing N interacting particles. The spatial structure of the wave function, which can be deduced from the one-particle and the two-particle correlation functions, can be compared with the equilibrium geometrical configurations obtained by minimizing (respect to the particle positions r) the classical electrostatic energy $E_{class} = \sum_i (U(\mathbf{r}_i) + \sum_{j < i} (e^2/\epsilon |\mathbf{r}_i - \mathbf{r}_j|))$ for a given confining potential U ⁶. For example Monte Carlo simulations for the classical configurations of point-like charges harmonically confined (carried out up to $N = 38$ [188] and $N > 200$ [189]), showed that the particles arrange in a single circular ring for $N \leq 5$, while internal shells are occupied for $N > 5$. In this case, isomeric configurations are energetically close to the ground state. For very large $N \approx 200$ the innermost shells approximate the bulk triangular arrangement. Analogous calculations for other kinds of confining potentials have been performed, for example for isotropic [189] hard-wall potentials where defined shells are present even for large particle numbers. The classical energy is a lower bound for the quantum mechanical ground-state.

In the Wigner limit the energy excitation spectrum resembles the rotational and vibrational modes allowed by the symmetry group of the electron molecule [104], hence a semiclassical model becomes an important interpretation tool [190, 191]. For example the excitation spectrum of a two-electron QD with harmonic confinement, for highly interacting regimes ($l = 200$), has the same structure of the roto-vibrational bands of the diatomic molecule. In particular the collective motion consist of rotations, bending and stretching vibrations, obtained by the exact solutions (for $N = 2$) of the equation of motion [190]. This structure is preserved also prior to the onset of the WM.

⁶for a macroscopic realization of these 2D classical system in a parabolic potential see Ref. [187]

3.3 Experimental investigation of Wigner molecules

Spectroscopy measurements can access the excitation modes of Wigner molecules realized in QDs with controlled dot population and electrostatic confinement potential. So far, signatures of the WM were found in GaAs/AlGaAs semiconductor heterostructures hosting QDs and in carbon nanotube QDs, both of which allow for clean structures. We remark that the interpretation of the experiments discussed below revealing the WM formation (or its onset), is based on the comparison of the measured excitation energies with configuration interaction predictions.

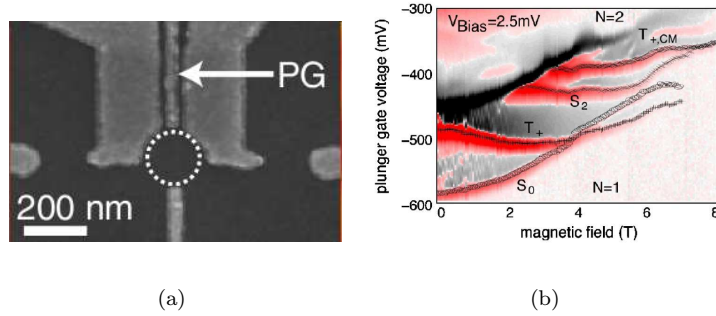


FIGURE 3.1: (a) Ga[Al]As quantum well with the center located 75 nm below the surface. The quantum dot diameter was 220 nm. (b) Differential conductance (at fixed bias) as a function of the plunger gate and magnitude of the perpendicular magnetic field. For increasing magnetic field the transitions between the one-electron ground state and the two-electron spin-singlet ground state (S_0), spin-triplet excited state (T) and spin-singlet excited state (S_2) are visible. Both figures are adopted from Ref. [42].

Tunnelling spectroscopy measurements (see. Section 2.3.3) of the excitation spectrum of a two-electron GaAs/AlGaAs QD, at finite magnetic field ⁷, have shown that the ground-state undergoes a singlet-triplet transition with increasing magnetic field. This observation highlighted the importance of correlations at $l \approx 1.5$ (with $\hbar\omega_0 \approx 5$ meV) and—due to the anti-symmetry of the two-particle wavefunction—suggested the formation of an electron molecule already at low magnetic fields. Indeed, comparison with exact diagonalisation predictions, reproducing the measured spectra, linked the observed modification of the electronic spectrum for increasing B with the modification of the two-electron wavefunction into a molecular dimer with increasing interparticle separation and decreasing overlap between the electron wavefunctions [42].

Resonant inelastic light scattering can be used to inquire the degree of correlation of confined electron systems as it access neutral⁸ few-body excitations of QDs consisting

⁷the experiment was prepared in a situation of negligible Zeeman splitting, thus avoiding a different source of the observed single-triplet transition

⁸neutral excitations involve different Fock- Darwin shells (with same parity) and conserve the angular momentum (monopole excitations) [192]

on spin and charge modes ⁹ [192]. For parabolic confinement the correlated state is characterized by the separation of the relative and center-of-mass motion as stated by the Kohn theorem. In a correlated regime when spatial localization has not been fully reached, at $r_s \approx 1.7$ ¹⁰ with $\hbar\omega_0 \approx 3.8$ meV, i.e. close to the onset of the WM formation, inelastic light-scattering measurements have probed the low-lying few-body excitations of four-electrons QDs realized in GaAs/AlGaAs heterostructures. They have been identified as roto-vibrations with rigid rotor and relative-motion decoupled components. In particular, the relative-motion modes have been demonstrated to be independent of the total angular momentum of the rotational state, modulated by exploiting the transition of the ground-state driven by a moderate magnetic field. The observed molecular-like separation of modes is due to strong correlation as demonstrated by an interpretation based on the CI method [43]. The same optical spectroscopy technique in GaAs/Al-

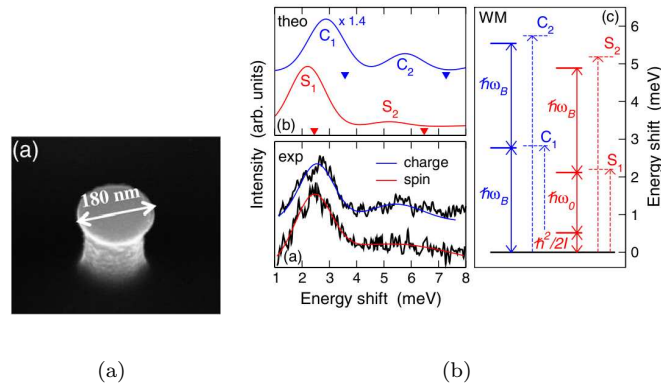


FIGURE 3.2: (a) Scanning electron microscopy of the GaAs/AlGaAs quantum dot with diameter indicated. (b) Measured spin and charge excitations (down panel), the dark lines are Gaussian curves fitting the data. The excitation spectrum is precisely reproduced by CI calculations (upper panel) while Hartree-Fock predictions for the peaks positions (shown by triangles) miss the transition energies, thus correlations effects are unprecindible to interpret the spectrum. The comparison between CI (dashed lines) and the WM modes (solid lines) confirm that at $r_s = 1.6$ the electrons form a dimmer.

Figures are adopted from Ref. [44].

GaAs QDs was employed in another subsequent experiment (in Ref. [44]), performed in a stronger interacting regime, that revealed a two-electron ¹¹ WM at zero magnetic field. In the regime characterized by $r_s \approx 3.4$, with $\hbar\omega_0 \approx 1.6$ meV, the measured low-lying excitation modes were precisely reproduced by fully accounting the electron correlation, which has been demonstrated to be crucial for their interpretation (see left panels of Fig. 3.2(b)). The observed modes, through the comparison with the predicted modes of

⁹in inelastic light scattering experiments spin and charge modes can be discriminated through the polarization of the scattered light [43].

¹⁰defined as $r_s = 1/[a_B \sqrt{\pi n}]$ where a_B is the effective Bohr radius and n the average electron density

¹¹the control of the dot population up to single electron accuracy was achieved through photodepletion by modulating the intensity of a HeNe continuous wave laser beam, the number of confined electrons being identified by the measured spectra of the excitations [44]

the limit case of perfect localization (see right panel in Fig. 3.2(b)), were recognized as the breathing, center-of-mass oscillations and the rigid-rotor rotation modes of a Wigner dimer and their energy quanta were determined. Such identification was confirmed by the analysis of the profiles of pair correlation functions of the excited states which showed a residual delocalization of electrons [44].

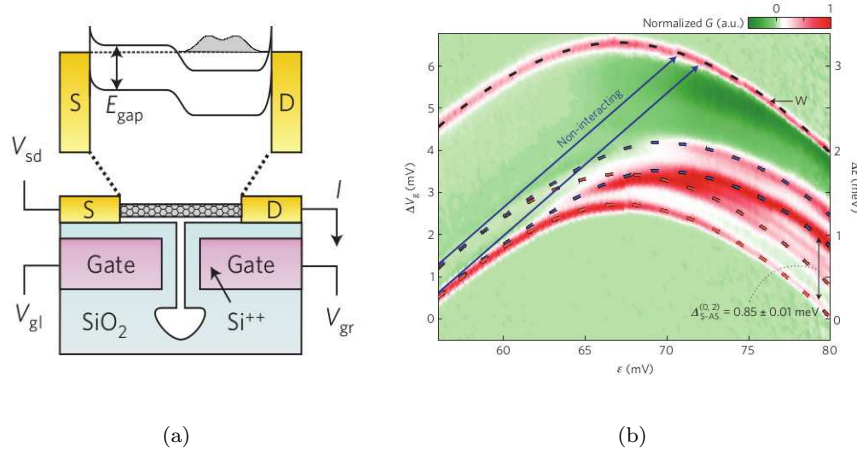
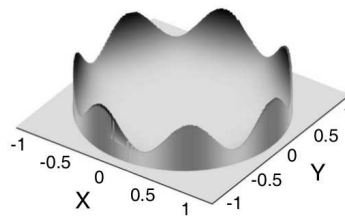


FIGURE 3.3: (a) Schematic of the tunneling spectroscopy set-up: a suspended carbon-nanotube is contacted with source (S) and drain (D) leads, two back gates induce an electrostatic potential (upper panel) along the CNT which allows to tune between the spatial configurations of the two electrons in a different (1,1) and same (0,2) extremities of the CNT. (b) Differential conductance at zero magnetic field as a function of the common gate voltage V_g and the detuning voltage ϵ , the change in slope marks the crossing between the (1,1) configuration and the (0,2) configuration. The red lines correspond to symmetric states while the blue lines to antisymmetric states. The energy splitting between the 2-electrons asymmetric excited-state (blue-dashed lines) and the ground-state (red-dashed bottom line) is one order of magnitude smaller respect to non-interacting value [45]. Figures adopted from Ref. [45]

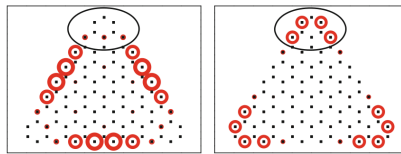
Recently a tunneling spectroscopy experiment, in Ref. [45], demonstrated the formation of a WM in an ultra-clean carbon nanotube (CNT) QD. In order to unambiguously establish the effect of the interaction—which is strong, due to the CNT low screening—various measures were taken. The device used consisted on a ultra-clean suspended nanotube with source and drain contacts on a pair of split-gate electrodes (see Fig. 3.3(a)). The two-electron case was probed, for which precise theoretical predictions [193, 194] allow to distinguish between the effect of spin orbit coupling from the role of interaction on the excitation spectrum. Eventual disorder effects were excluded measuring both electrons and holes spectra—which have opposite response to disorder potentials. The confining potential was controlled through highly tunable gates allowing to exclude extrinsic electrostatic effects. In particular by varying the voltage difference between the split-gate (detuning), the switching between two different spatial configurations of the two electrons was controlled: in the first configuration (low detuning) each electron is in a different extremity of the CNT and the spatial separation is caused by the effect

of the gates, in the second configuration (high detuning) the two electrons are in the same extremity of the CNT and the spatial separation can be ascribed exclusively to the electron repulsion. After the identification of the spatial symmetry of the probed states by monitoring their behaviour in a magnetic field, it has been observed that the excitation energies—given by the single-particle level spacing in the non-interacting regime—quench since the interaction increases forcing the symmetric ground-state to modify its symmetry, as confirmed by CI calculations. The quenching of excitation energies is shown in Fig 3.3(b). This is a paramount example of the high experimental control over extrinsic effects that is required to probe the WM delicate state.

3.4 Electron localization in graphene QDs



(a)



(b)

FIGURE 3.4: Predicted edge-states WMs in graphene QDs (a) Pinned $N = 7$ electron molecule in a circular graphene QD. The figure shows the electron density (lengths are given in units of the dot radius R , the electron density units are R^{-2}) calculated from the superposition of trial (variational) wavefunctions of different total angular momentum. Figure adopted from Ref. [53]. (b) Spin-polarized WMs formed by the edge-states in a triangular graphene QD. The spin densities (red circles around each given atom) of the three electrons (holes) ground-state are shown in the left (right) panel. Figure adapted from Ref. [54].

Most theoretical works investigating electron localization in graphene QDs mainly focused on systems whose noninteracting energy spectrum is dominated by edge states, neglecting orbital states delocalized over the whole dot area. Such edge states form degenerate shells with degeneracy proportional to the imbalance between the number of A-type and B-type atoms at the edges, that is maximal for zig-zag edges [55]. As

the degenerate Landau levels in a strong magnetic fields, degenerate edge states are expected to be strongly affected by Coulomb interaction. The model for circular dots with (enforced) uninterrupted zig-zag boundary conditions has been investigated through both Hartree approximation and configuration-interaction methods with electrons being considered in the restricted space of fully spin-polarized states. Surface states close to half filling were found to be strongly correlated, giving rise to electrons localized at the vertexes of regular polygons at the dot edges. Different trial wavefunctions have been proposed to interpret the few-body correlated state as Laughlin or Wigner localized wavefunctions [56], or variational rotating-electron-molecule wavefunctions that reproduce the correlations and the spectra found by calculations [53]. As zig-zag edges are necessarily disrupted in circular QDs by arm-chair portions of edges, the results suggest that this disruptions act as impurities that pins the molecular structure of electrons at edges [53, 56]. An example of the structure of the $N = 7$ electron wavefunction of a pinned WM at the edge of a circular QD is reported after Ref. [53] in Fig. 3.4(a).

Triangular gated-defined QDs—zig-zag ending—have been investigated by combining atomistic, mean field and CI methods [54, 55]. It has been predicted that few excess charge carriers added at charge neutrality give rise a WM of spin polarized electrons (see Fig. 3.4(b)) in small dots for certain filling fractions of the degenerate bands of edge states [54]. In this case of triangular symmetry, the correlated wavefunction cannot be compared with analytical trial wavefunctions. These findings were formulated within a broader investigation of magnetism at edges.

Beyond electron correlation among edge states, interaction between delocalized states populating graphene magnetic dots has been studied through configuration-interaction method in the work in Ref. [58]. It has been pointed out the localization of the three-electron state and the effect of the mass gap that enhances localization. The investigation is restricted to valley polarized electrons. Another work (in Ref. [57]) considered two different circular confinement configurations: an infinite-mass boundary condition, which models etched graphene QDs [129], and magnetic confinement realized through an inhomogeneous magnetic field [57]. The investigation of up to $N = 20$ interacting electrons in Ref. [57] is based on the Hartree-Fock (HF) method, the exact diagonalization method being used as a benchmark for the case of $N = 2$ particle. The valley degree of freedom has not be included in the calculations. It has been found that as the Coulomb interaction increases, the addition spectra of the quantum dot as a function of the electron number presents more pronounced peaks with respect to the non-interacting structure. The HF results for the ground-state radial density and density-density correlation function exhibit the formation of radial rings for increasing graphene interaction

parameter r_s . For the maximum $r_s = 2$ considered in Ref. [57], the spatial shell fillings have been shown to be in qualitative agreement with the classical shell filling for hard-wall confinement, with deviations being found at large electron numbers ($N > 10$).

Chapter 4

Model system and numerical approach

In this Chapter we present the method employed to solve the problem of few-interacting electrons populating the conduction band of a clean graphene QD. In the presence of a mass gap, induced by the breaking of sublattice symmetry, the QD is defined by a circular confining potential, as induced by patterned gate-electrodes, the electric gate potential being assumed to vary stepwise. First, we deduce the bound-states of electrons in the conduction band by following the method of Ref. [59]. Afterwards we present the configuration interaction (CI) method employed to include the effect of electron-electron interaction.

4.1 Single-particle model

The first step in determining the interacting electron states is to find the eigenstates of a single electron in the graphene QD under consideration. The general approach for deriving an effective mass Hamiltonian, stated by Luttinger and Kohn [195], has been applied to graphene by McClure in the presence of a magnetic field [62] and later by DiVincenzo and Mele in the presence of an external potential [64]. The effective Hamiltonian describes the single particle dynamics of charge carriers in graphene for energies close to the Dirac points.

In our system the external potential is composed by the confinement potential being identical on sublattices A and B, that we assume to be the hard-wall confining potential $U(\rho) = U_0 \Theta(\rho - R)$ of height U_0 with R denoting the QD radius and $\rho = (x^2 + y^2)^{1/2}$, a staggered potential with different values on the A and B sublattices, that is thus coupled

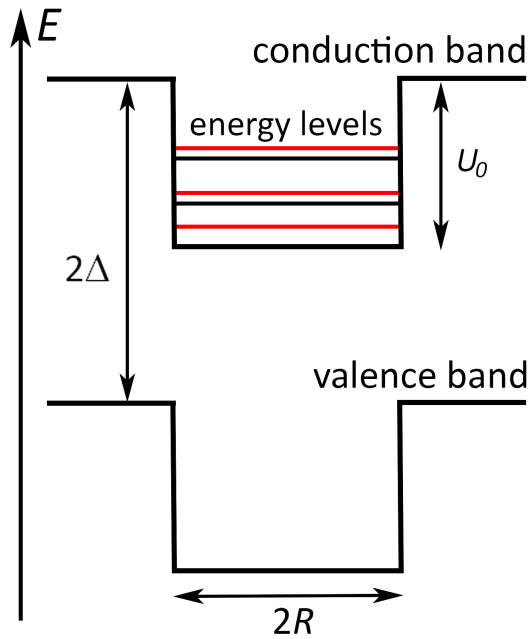


FIGURE 4.1: Radial QD confinement potential. The interaction between graphene and substrate opens a mass gap 2Δ in the QD energy spectrum. Bound state energy levels in the conduction band are shown.

to the Hamiltonian via the 2×2 Pauli matrix $\hat{\tau}_3$. As it has been discussed in Section 2.3.2, this staggered potential can be experimentally induced through substrate-graphene interaction. Due to the presence of the mass-term $\Delta\hat{\tau}_3$ which opens an energy gap of 2Δ in the energy spectrum, the Klein tunneling effect can be avoided and, consequently, the charge carriers will be confined. The low-energy charge carrier states are described by the effective Hamiltonian

$$\hat{H}_\tau = -i\hbar v_F [\hat{\tau}_1(\partial_x + eA_x) + \hat{\tau}_2(\partial_y + eA_y)] + \tau\Delta\hat{\tau}_3 + U(\rho)\hat{\tau}_0, \quad (4.1)$$

in the valley isotropic form [155], where the graphene valleys K and K' are identified by the index $\tau = \pm 1$. The Hamiltonian includes, within the minimal coupling, an homogeneous magnetic field $\vec{B} = B\hat{z}$ normal to the graphene plane, in the symmetric gauge $\vec{A} = (A_x, A_y, A_z) = \frac{B}{2}(-y, x, 0)$. In Eq. 4.1, $v_F \approx 10^6$ m/s is the Fermi velocity, $-e$ is the electron charge. The 2×2 Pauli matrices $\hat{\tau}_1$, $\hat{\tau}_2$, $\hat{\tau}_3$, and the unit matrix $\hat{\tau}_0$ act on envelope-functions that are pseudospinors of the form

$$\Phi(\rho, \varphi) = e^{i(j-1/2)\varphi} \begin{pmatrix} \mathcal{R}^A(\rho) \\ e^{i\varphi}\mathcal{R}^B(\rho) \end{pmatrix}. \quad (4.2)$$

whose components are the A/B sublattice envelopes. Here φ is the azimuthal angle,

$j = m + 1/2$, $m \in \mathbb{Z}$ is the half-integer quantum number eigenvalue of the 'pseudospin-orbital' total angular momentum $\hat{j}_z = -i\hbar\partial/\partial\varphi + \hbar\hat{\tau}_3/2$, and $\mathcal{R}^A(\rho)$ [$\mathcal{R}^B(\rho)$] is the radial envelope on sublattice A [B]. We find the eigenstates of 4.1 by following the procedure of Ref. [59]. For numerical calculations we take $\Delta = U_0 = 0.26$ eV.

4.1.0.1 Bound-states with magnetic field

The eigenvalue problem

$$\hat{H}_\tau \Phi(x, y) = \varepsilon \Phi(x, y) \quad (4.3)$$

reduces to a one dimensional problem $\hat{H}_\tau^{(1)} \mathcal{R}(\rho) = \varepsilon \mathcal{R}(\rho)$ with

$$\hat{H}_\tau^{(1)} = \begin{pmatrix} \tau\Delta + U(\rho) & -iv_F\hbar[\partial_\rho + \frac{j+1/2}{\rho} + \frac{eB\rho}{2\hbar}] \\ iv_F\hbar[-\partial_\rho + \frac{j-1/2}{\rho} + \frac{eB\rho}{2\hbar}] & -\tau\Delta + U(\rho) \end{pmatrix} \quad (4.4)$$

acting on the radial part of the envelope function $\mathcal{R}(\rho) = [\mathcal{R}^A(\rho), \mathcal{R}^B(\rho)]^T$, and it is equivalent to the system of coupled differential equations

$$\begin{cases} v_F\hbar[\partial_\rho + \frac{(j+1/2)}{\rho} + b\rho]i\mathcal{R}^B = [\tau\Delta - \varepsilon]\mathcal{R}^A \\ v_F\hbar[\partial_\rho - \frac{(j-1/2)}{\rho} - b\rho]i\mathcal{R}^A = -[\tau\Delta + \varepsilon]\mathcal{R}^B \end{cases}, \quad (4.5)$$

where the definitions $b \equiv \frac{eB}{2\hbar}$, for the term containing the magnetic field contribution, and

$$\begin{cases} \varepsilon = \varepsilon_{<} \equiv \varepsilon & \text{for } \rho < R \\ \varepsilon = \varepsilon_{>} \equiv \varepsilon - U_0 & \text{for } \rho > R \end{cases} \quad (4.6)$$

for the kinetic energy contribution, have been introduced for the sake of simplicity. In order to find the bound-states solutions within the conduction band (see. Fig 4.1), i.e, the solutions of Eq. 4.3 with energy in the range $\Delta < \varepsilon < \Delta + U_0$, the system 4.5 is decoupled into two second order differential equations

$$\rho^2 \frac{d^2 \mathcal{R}^B}{d\rho^2} + \rho \frac{d\mathcal{R}^B}{d\rho} = [b^2 \rho^4 + \rho^2 [(2j-1)b + \frac{\Delta^2 - \varepsilon^2}{(v_F\hbar)^2}] + j + \frac{1}{4} + j^2] \mathcal{R}^B \quad (4.7)$$

and

$$\rho^2 \frac{d^2 \mathcal{R}^A}{d\rho^2} + \rho \frac{d\mathcal{R}^A}{d\rho} = [b^2 \rho^4 + \rho^2 [(2j+1)b + \frac{\Delta^2 - \varepsilon^2}{(v_F\hbar)^2}] - j + \frac{1}{4} + j^2] \mathcal{R}^A. \quad (4.8)$$

which are independent from the valley index. Therefore, each radial component satisfies a general hypergeometric differential equation of the form

$$\rho^2 \frac{d^2 \mathcal{R}^{A/B}}{d\rho^2} + \rho \frac{d\mathcal{R}^{A/B}}{d\rho} = [b^2 \rho^4 + \rho^2 a_{A/B} + n_{A/B}^2] \mathcal{R}^{A/B}. \quad (4.9)$$

The parameters for the sublattice A and B components are

$$\begin{cases} a_A \equiv 2b \left(j + \frac{1}{2} \right) - \frac{\epsilon^2 - \Delta^2}{(v_F \hbar)^2} & \text{for } \mathcal{R}^A \\ a_B \equiv 2b \left(j - \frac{1}{2} \right) - \frac{\epsilon^2 - \Delta^2}{(v_F \hbar)^2} & \text{for } \mathcal{R}^B \end{cases} \quad (4.10)$$

and

$$\begin{cases} n_A \equiv |j - \frac{1}{2}| & \text{for } \mathcal{R}^A \\ n_B \equiv |j + \frac{1}{2}| & \text{for } \mathcal{R}^B \end{cases} \quad (4.11)$$

The eigenfunction radial part inside the dot ($\rho < R$) is given by the solution of Eq. 4.9 regular at the origin

$$\mathcal{R}_{<}(\rho) = e^{-b\rho^2/2} \begin{pmatrix} \beta_A 2^{(1+n_A)/2} \rho^{n_A} M(q_A, 1 + n_A, b\rho^2) \\ \beta_B 2^{(1+n_B)/2} \rho^{n_B} M(q_B, 1 + n_B, b\rho^2) \end{pmatrix} \quad (4.12)$$

where $M(q, 1 + n, x)$ is the confluent hypergeometric function of the first kind [196], $q_A \equiv \frac{1}{4}[\frac{a_A}{b} + 2(1 + n_A)]$ and $q_B \equiv \frac{1}{4}[\frac{a_B}{b} + 2(1 + n_B)]$.

The normalizable solution of Eq. 4.9 outside the dot ($\rho > R$) is

$$\mathcal{R}_{>}(\rho) = e^{-b\rho^2/2} \begin{pmatrix} \alpha_A 2^{(1+n_A)/2} \rho^{n_A} U(r_A, 1 + n_A, b\rho^2) \\ \alpha_B 2^{(1+n_B)/2} \rho^{n_B} U(r_B, 1 + n_B, b\rho^2) \end{pmatrix} \quad (4.13)$$

where $U(r, 1 + n, x)$ is the confluent hypergeometric function of the second kind decaying exponentially for large ρ [196], and the definitions $r_A \equiv \frac{1}{4}[\frac{a_A}{b} + 2(1 + n_A)]$ and $r_B \equiv \frac{1}{4}[\frac{a_B}{b} + 2(1 + n_B)]$ hold.

To proceed we find the normalization constants α_A/α_B , and β_A/β_B distinguishing between the two cases $j > 0$ and $j < 0$. For $j > 0$, the first equation of the system 4.5, by plugging the solution for $\rho < R$, Eq. 4.12, and by taking into account that

$n \equiv n_A = n_B - 1$ and $q \equiv q_A = q_B = j + (1/2) - (\epsilon_<^2 - \Delta^2)/(4b(v_F\hbar)^2)$ becomes

$$(\tau\Delta - \epsilon_<) \beta_A e^{-b\rho^2/2} 2^{1+n} \rho^n M(q, 1+n, b\rho^2) - iv_F\hbar\beta_B \left[\frac{d}{d\rho} + \frac{(j+1/2)}{\rho} + b\rho \right] e^{-b\rho^2/2} 2^{2+n} \rho^{1+n} M(q, 2+n, b\rho^2) = 0. \quad (4.14)$$

From the recurrence relation 13.4.13 of [196]:

$$\frac{d}{dx} M(q, 1+n, x) = \frac{n}{x} [M(q, n, x) - M(q, 1+n, x)], \quad (4.15)$$

and from Eq. 4.14, it follows that

$$\frac{\beta_A}{\beta_B} = \frac{2^{3/2} v_F \hbar (n_A + 1)}{(\tau\Delta - \epsilon_<)}. \quad (4.16)$$

The ratio α_A/α_B is deduced in an analogous way from $r \equiv r_A = r_B = j + (1/2) - (\epsilon_>^2 - \Delta^2)/(4b(v_F\hbar)^2)$, e.g., from the substitution of Eq. 4.13 into the first equation of the system 4.5 by employing the recurrence relation 13.4.24 of [196]. The result is

$$\frac{\alpha_A}{\alpha_B} = \frac{2^{3/2} v_F \hbar (n_B - r)}{\tau\Delta - \epsilon_>}. \quad (4.17)$$

The continuity condition for the radial envelope functions at the dot edge $\rho = R$

$$\mathcal{R}_>(R) = \mathcal{R}_<(R), \quad (4.18)$$

provides the characteristic equation for the bound-state energies

$$\frac{\beta_A M(q_A, 1+n_A, bR^2)}{\beta_B M(q_B, 1+n_B, bR^2)} = \frac{\alpha_A U(r_A, 1+n_A, bR^2)}{\alpha_B U(q_B, 1+n_B, bR^2)}. \quad (4.19)$$

For $j > 0$, using the expressions for the ratios α_A/α_B and β_A/β_B in Eqs. 4.17 and 4.16, the matching condition in Eq. 4.19 yields

$$\frac{4b(\hbar v_F)^2(j+1/2)}{(\epsilon_< - \tau\Delta)(\epsilon_> + \tau\Delta)} M(q, j+1/2, bR^2) U(r, j+3/2, bR^2) - M(q, j+3/2, bR^2) U(r, j+1/2, bR^2) = 0. \quad (4.20)$$

Similarly for $j < 0$, by accounting that $q_A = q_B + 1 = 1 - (\epsilon_<^2 - \Delta^2)/[4b(v_F\hbar)^2]$ and $n_A = n_B + 1$ it follows that

$$\frac{\beta_A}{\beta_B} = \frac{-(\tau\Delta + \epsilon_<)}{n_A 2^{3/2} v_F \hbar} \quad (4.21)$$

and from $r_A = r_B + 1 = 1 - (\epsilon_>^2 - \Delta^2)/[4b(v_F\hbar)^2]$,

$$\frac{\alpha_A}{\alpha_B} = \frac{(\tau\Delta + \epsilon_>)}{2^{3/2}v_F\hbar}. \quad (4.22)$$

Therefore, for $j < 0$, the matching condition in Eq. 4.19 leads to

$$\begin{aligned} & \frac{-(\tau\Delta + \epsilon_<)}{(\tau\Delta + \epsilon_>)(-j + 1/2)} M(q_A, -j + 3/2, bR^2) U(r_A - 1, -j + 1/2, bR^2) \\ & - M(q_A - 1, -j + 1/2, bR^2) U(r_A, -j + 3/2, bR^2) = 0. \end{aligned} \quad (4.23)$$

Therefore, in the presence of a perpendicular magnetic field, we find that the confined states in the conduction band are given by Eqs. 4.12 and 4.13, the energy eigenvalues are the solutions of Eq. 4.20 and Eq. 4.23 for $j > 0$ and $j < 0$ respectively. These secular equations are solved numerically and their roots used to write down explicitly the two-component pseudospinors. The constants $\alpha_A, \alpha_B, \beta_A, \beta_B$ are determined by imposing the normalization condition

$$\int_0^\infty \int_0^{2\pi} |\Phi(\rho, \varphi)|^2 d\varphi \rho d\rho = 1. \quad (4.24)$$

4.1.0.2 Bound-states with zero magnetic field

Now we consider the limit case $B = 0$. From the reduced eigenvalue problem

$$\hat{H}_\tau^{(1)} \mathcal{R}(\rho) = \varepsilon \mathcal{R}(\rho), \quad (4.25)$$

with

$$\hat{H}_\tau^{(1)} = \begin{pmatrix} \tau\Delta + U(\rho) & -iv_F\hbar[\partial_\rho + \frac{j + 1/2}{\rho}] \\ iv_F\hbar[-\partial_\rho + \frac{j - 1/2}{\rho}] & -\tau\Delta + U(\rho) \end{pmatrix} \quad (4.26)$$

it follows that each component of the radial envelope $\mathcal{R}(\rho) = [\mathcal{R}^A(\rho), \mathcal{R}^B(\rho)]^T$ satisfies the second-order decoupled equation

$$\begin{cases} x^2 \frac{d^2 \mathcal{R}_{A/B}(x)}{dx^2} + x \frac{d\mathcal{R}_{A/B}(x)}{dx} - [-\Omega^2 R^2 x^2 + n_{A/B}^2] \mathcal{R}_{A/B}(x) = 0 & \text{for } \rho < R \\ x^2 \frac{d^2 \mathcal{R}^{A/B}(x)}{dx^2} + x \frac{d\mathcal{R}^{A/B}(x)}{dx} - [\Lambda^2 R^2 x^2 + n_{A/B}^2] \mathcal{R}^{A/B}(x) = 0 & \text{for } \rho > R \end{cases} \quad (4.27)$$

with $x = \rho/R$ and

$$\begin{cases} \Omega \equiv \frac{\sqrt{\varepsilon^2 - \Delta^2}}{v_F \hbar} \\ \Lambda \equiv \frac{\sqrt{\Delta^2 - (\varepsilon - U_0)^2}}{v_F \hbar} \end{cases}. \quad (4.28)$$

For $\rho < R$, Eq. 4.27 is the Bessel-Bowman differential equation [197] of order $n_{A/B} \in \mathbb{Z}$. The bound state requirement of regularity at the origin is satisfied by

$$\mathcal{R}_{\tau, <}(\rho) = \begin{pmatrix} \beta_A J_{n_A}(\Omega \rho) \\ \beta_B J_{n_B}(\Omega \rho) \end{pmatrix} \quad (4.29)$$

with J_n the Bessel function of the first kind of order n . For $\rho > R$, Eq. 4.27 becomes the Modified Bessel-Bowman equation [197] of order $n_{A/B} \in \mathbb{Z}$, which solution

$$\mathcal{R}_{\tau, >}(\rho) = \begin{pmatrix} \alpha_A K_{n_A}(\Lambda \rho) \\ \alpha_B K_{n_B}(\Lambda \rho) \end{pmatrix} \quad (4.30)$$

with K_n the modified Bessel function of the second kind of order n , decays asymptotically at large distances and is normalisable. We recall that the definitions $n_A = |j - 1/2|$ and $n_B = |j + 1/2|$ hold, such that the Bessel functions orders depend on the total angular momentum eigenvalue. Additional solutions do not satisfy the bound states requirements of regularity and normalizability.

From the bound state solutions, the ratios between normalization constants $\alpha_A, \alpha_B, \beta_A, \beta_B$ —as illustrated in detail above for finite magnetic field—are obtained from plugging the bound state expressions Eqs. 4.30 and 4.29 into the Dirac equation 4.25 and employing recurrence relations between Bessel functions. The result of this procedure is

$$\begin{cases} \alpha_A/\alpha_B = -\frac{\Lambda v_F \hbar}{[\tau \Delta - (\varepsilon - U_0)]} \\ \beta_A/\beta_B = \frac{i v_F \hbar}{\tau \Delta - \varepsilon} \Omega \end{cases} \quad (4.31)$$

for $j > 0$, and

$$\begin{cases} \alpha_A/\alpha_B = \frac{[\tau \Delta + (\varepsilon - U_0)]}{v_F \hbar \Lambda} \\ \beta_A/\beta_B = \frac{-w_F \hbar \Omega}{\tau \Delta - \varepsilon} \end{cases} \quad (4.32)$$

for $j < 0$.

Using the expressions for α_A/α_B and β_A/β_B , the energy quantization condition derived from the continuity of the spinor at the dot edge, Eq. 4.18, is

$$\begin{cases} \frac{\Omega}{[\tau\Delta - (\varepsilon - U_0)]} \frac{(\tau\Delta - \kappa_{>})}{\Lambda} J_{n_A}(\Omega R) K_{n_B}(\Lambda R) + J_{n_B}(\Omega R) K_{n_A}(\Lambda R) = 0 & \text{for } j > 0 \\ \frac{\Lambda}{[\tau\Delta + (\varepsilon - U_0)]} \frac{(\tau\Delta + \varepsilon)}{\Omega} J_{n_A}(\Omega R) K_{n_B}(\Lambda R) + J_{n_B}(\Omega R) K_{n_A}(\Lambda R) = 0 & \text{for } j < 0. \end{cases} \quad (4.33)$$

The above equations are linked by the transformation $j \rightarrow -j$ and $\tau \rightarrow -\tau$, therefore $\mathcal{R}_\tau^A = \mathcal{R}_{-\tau}^B$ and $\mathcal{R}_\tau^B = \mathcal{R}_{-\tau}^A$.

4.1.0.3 Single particle energy spectrum: magnetic field lifting of the valley degeneracy

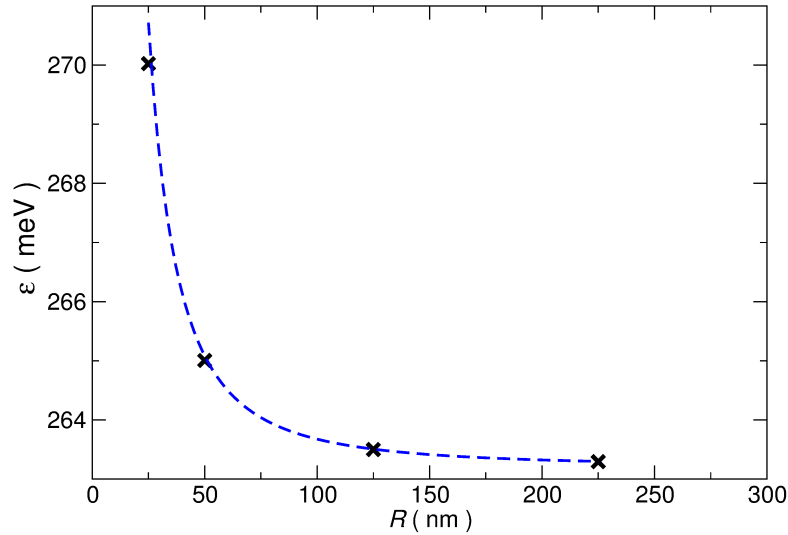
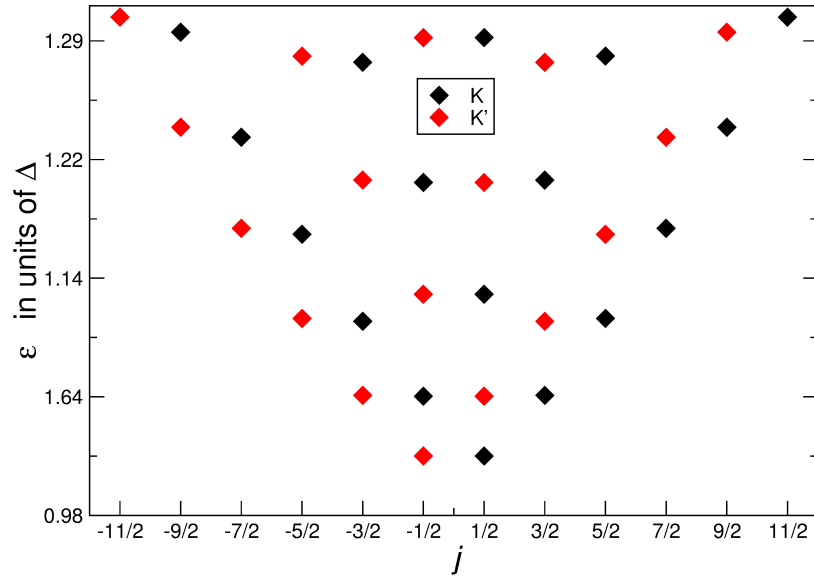


FIGURE 4.2: Single particle ground-state energy vs dot radius in the absence of magnetic field. The energy approximately scales as $1/R^2$ as shown by the fitting of numerical data (black crosses) with the blue curve (chi-square coefficient 1,63)

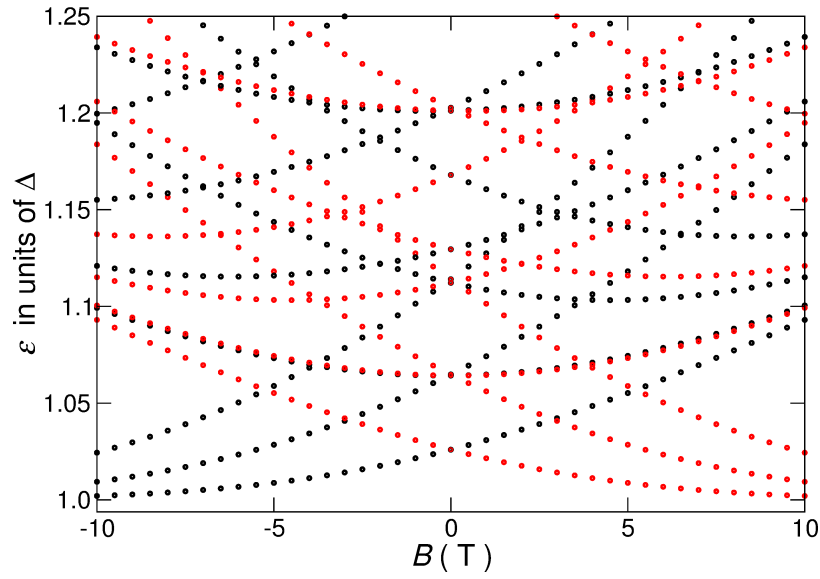
In the presence of a mass term, the lowest-energy solutions—numerically calculated—of the Eq. 4.33 for various dot radii, ranging from $R = 25$ nm to $R = 225$ nm, are shown in Fig. 4.2. The energy decreases for increasing dot radius as $\varepsilon \approx 1/R^2$ (instead of $1/R$ for massless electrons) as shown by the interpolating (blu) curve which fits the data with chi-square of 1,63.

The mass term $\tau\Delta\hat{\tau}_3$ breaks the time reversal symmetry operating within a single valley [102]—so called effective time reversal symmetry. This symmetry is represented by the symplectic¹ operator $\hat{S} \equiv i\hat{\tau}_2\hat{C}$ that transforms the mass term as $\hat{S}\Delta\hat{\tau}_3\hat{S}^+ = -\Delta\hat{\tau}_3$.

¹ $S^2 = -1$



(a)



(b)

FIGURE 4.3: Single particle energy levels for a dot of radius $R = 250 \text{ \AA}$ (a) Energy vs total 'pseudospin-orbital' angular momentum eigenvalue j and zero magnetic field. Black (red) color refers to the $\tau = 1$ ($\tau = -1$) valley. The eigenvalues display the symmetry $\varepsilon(j, \tau) = \varepsilon(-j, -\tau)$. Valley and spin degrees of freedom imply a four-fold degeneracy of the single particle energy spectrum. (b) Single particle energy spectrum for $j = \pm 1/2, \pm 1/3, \pm 5/2$ and different values of B . Energy is given in units of $\Delta = 0.26 \text{ eV}$. Same color code used in (a) distinguishes the two valleys. The valley degeneracy at $B = 0$ is broken for finite magnetic field.

Therefore the energy eigenvalues are such that $\varepsilon(j, \tau) \neq \varepsilon(-j, \tau)$ for both the considered cases of absence (Eq. 4.26) and presence (Eq. 4.4) of magnetic field.

In the absence of a perpendicular magnetic field, the—so called true time reversal symmetry— linking the two valleys is preserved, so that the energy eigenvalues of opposite valleys are degenerate

$$\varepsilon(j, \tau) = \varepsilon(-j, -\tau). \quad (4.34)$$

This is illustrated in Fig. 4.3(a) where the energy levels for zero magnetic field, computed numerically from Eq. 4.33, are shown as a function of the total angular momentum eigenvalue j , for a dot radius of $R = 250 \text{ \AA}$.

The presence of a perpendicular magnetic field breaks the true time reversal symmetry [155] lifting the two-fold degeneracy of the energy levels due to the valley degree of freedom (Eq. 4.34) as it is illustrated in Fig. 4.3(b), which compares the single-particle energy spectrum (in units of Δ) for different values of B . The spectra displayed in Fig. 4.3(b), computed numerically from Eqs. 4.23 and 4.20, include positive and negative values of B in order to illustrate that the energy eigenvalues satisfy $\varepsilon(B, j, \tau) = \varepsilon(-B, -j, -\tau)$.

4.2 Configuration interaction method

4.2.1 Introduction to the Configuration Interaction method

The configuration interaction (CI) method solves the N -body interacting problem for different kinds of interaction by expanding the N -body wavefunction in terms of configurational states, that contain as much Slater determinants as required in order to find the ground state energy at a given interaction strength. It has been largely used in quantum chemistry, where the method originates, and in nuclear physics, as well as successfully employed in condensed matter physics [42, 43, 45, 198], where it is known also as exact diagonalization.

In order to solve the few-electron problem in the graphene QD under consideration, we employ the full version of the CI method [199], that includes all the possible configurations constructed from the chosen single particle (SP) basis set, the only truncation being the cut-off on the expansion of the many-electron wave-function introduced by the finite size of the basis set. Among the several methods used to tackle the interacting problem in QDs, CI has been chosen because it retains all correlation effects missed or only partially taken into account in Hartree-Fock or DFT calculations. Moreover CI, compared to Quantum Monte Carlo frameworks, provides not only the N -body ground state but also the wave functions and energies of the lowest excited states, which extends the possibility of experimental comparison with excitation spectra measurements,

as well as correlation functions in real space. A critical comparison of CI with other methods in the context of the electronic properties of semiconductor quantum dots can be found in Ref. [41]. The main limitation of the CI method is the fact that the computational complexity increases exponentially with N , so the method can tackle only small numbers of interacting particles. However it allows us to tackle, with high numerical precision, the few-electron problem also in the strongly interacting regime, which is the main focus here.

As it has been mentioned in Section 3.4, the CI method has been already used in the context of graphene QDs. Some examples are the study of surface zig-zag states in the strongly interacting regime in circular [56] and triangular [54] graphene QDs. CI has been used as a benchmark for the 2-body energies computed through Hartree-Fock approximation and through the Müller exchange functional methods, in graphene QDs with infinite mass confinement and magnetic confinement conditions [57].

4.2.2 N-body interacting problem in second quantization

An appropriate formulation of the problem of N electrons interacting in a confined structure is provided by the standard second quantization formalism [104], briefly recalled below. We start by considering a single particle basis set of orthogonal orbitals $\{\phi_\alpha\}$, each orbital being uniquely specified by a tuple of quantum numbers α . If the set of single-particle orbitals is complete, it can be constructed a complete set of basis functions for the N -body Hilbert space. In the occupation number representation, the N -body space is constructed by N creation fermionic operators $\hat{c}_{\alpha\sigma}^\dagger$ acting successively on the vacuum $|0\rangle$. The operators $\hat{c}_{\alpha\sigma}^\dagger$, and hermitian conjugated destruction operators $\hat{c}_{\alpha\sigma}$, such that $\hat{c}_{\alpha\sigma}|0\rangle = 0$, respectively create and annihilate an electron of spin z -component σ in the orbital ϕ_α . The N -body basis-states constructed in this way are Slater determinants

$$|\chi_{\{\alpha_i\sigma_i}\}^{(N)}\rangle = \prod_i^N c_{\alpha_i\sigma_i}^\dagger |0\rangle \quad (4.35)$$

with the set of N occupied spin-orbitals $j \equiv \{\alpha_i\sigma_i\}_j$. Slater determinants are anti-symmetric under particle exchange, as required for fermions, since the operators anti-commute

$$\{\hat{c}_{\alpha\sigma}, \hat{c}_{\beta\sigma'}^\dagger\} = \delta_{\alpha,\beta}\delta_{\sigma,\sigma'} \quad \{\hat{c}_{\alpha\sigma}, \hat{c}_{\beta\sigma'}\} = \{\hat{c}_{\alpha\sigma}^\dagger, \hat{c}_{\beta\sigma'}^\dagger\} = 0. \quad (4.36)$$

The N -body Hamiltonian for an isolated system of interacting electrons is

$$\begin{aligned}\hat{H} &= \hat{H}_{SP} + \hat{V} \\ &= \sum_{\alpha\beta\sigma} \varepsilon_{\alpha\beta} \hat{c}_{\alpha\sigma}^\dagger \hat{c}_{\beta\sigma} + \frac{1}{2} \sum_{\alpha\beta\gamma\delta\sigma\sigma'} V_{\alpha\beta\gamma\delta} \hat{c}_{\alpha\sigma}^\dagger \hat{c}_{\beta\sigma'}^\dagger \hat{c}_{\gamma\sigma'} \hat{c}_{\delta\sigma}\end{aligned}\quad (4.37)$$

where the indices $\alpha, \beta, \gamma, \delta$ run over the complete set of single particle states. The single-particle one-body operator \hat{H}_{SP} includes the kinetic energy operator and an eventual external trapping potential, while the two-body operator \hat{V} includes the interaction between particles. The matrix elements of the one and two-body operators in the chosen single-particle basis-set are respectively

$$\varepsilon_{\alpha\beta} = \int d\mathbf{r} \phi_\alpha(\mathbf{r})^* H_{SP}(\mathbf{r}) \phi_\beta(\mathbf{r}) \quad (4.38)$$

and

$$V_{\alpha\beta\gamma\delta} = \int d\mathbf{r} \int d\mathbf{r}' \phi_\alpha^*(\mathbf{r}) \phi_\beta^*(\mathbf{r}') v(\mathbf{r} - \mathbf{r}') \phi_\gamma(\mathbf{r}') \phi_\delta(\mathbf{r}) \quad (4.39)$$

where $v(\mathbf{r} - \mathbf{r}')$ is the interacting potential. This expression includes direct ($\alpha = \delta$ and $\beta = \gamma$), exchange ($\alpha = \gamma$ and $\beta = \delta$) and off-diagonal terms.

4.2.3 Configuration state function expansion

In order to solve the secular equation

$$(\hat{H} - E_N \hat{I}) |\Psi^{(N)}\rangle = 0. \quad (4.40)$$

associated with the N -body problem, where \hat{H} is the interacting Hamiltonian in Eq. 4.37 and \hat{I} the identity matrix, a set of N_{SP} single-particle orbitals is chosen to construct N_{SD} Slater determinants $|\chi_j^{(N)}\rangle$ spanning the Hilbert space. The number of Slater determinants is $N_{SD} = (2N_{SP})! / N! (2N_{SP} - N)!$ since each orbital can host two fermions with opposite spins. From the Slater determinants, the N -body set of configurational states functions (CSFs) is constructed in terms of linear combinations with Clebsch-Gordan coefficients b_{ij} as

$$|\Xi_i\rangle = \sum_j b_{ij} |\chi_j\rangle. \quad (4.41)$$

The CSFs have the correct symmetry of the Hamiltonian, e.g, if the Hamiltonian does not contain any spin interaction terms, as in the cases treated here, CSFs are eigenstates not only of the spatial symmetry group of \hat{H} but also of both S_z and the square total

spin S . The N -body state $|\Psi^{(N)}\rangle$ is then expanded in terms of CSFs

$$|\Psi^{(N)}\rangle = \sum_i a_i |\Xi_i\rangle. \quad (4.42)$$

The interacting Hamiltonian 4.37, in the basis set of CSFs is block diagonal, its matrix elements can be calculated from the Clebsch-Gordan coefficients b_{ij} and from the matrix elements between Slater determinants. The N -body problem Eq. 4.40 reduces in this way to a matrix eigenvalue problem which can be numerically solved [199].

4.2.4 Single particle basis-set and two-body matrix elements

We focus on the interaction among few excess charge carriers populating the conduction band of the graphene QD, so that the vacuum state consist of completely filled valence band and empty conduction band. The basis set $\{\phi_\alpha\}$ is chosen from the eigenstates of the single-particle Hamiltonian $H_\tau = -i\hbar v_F[\hat{\tau}_1(\partial_x + eA_x) + \hat{\tau}_2(\partial_y + eA_y)] + \tau\Delta\hat{\tau}_3 + U(\rho)\hat{\tau}_0$, identified by the tuple of orbital quantum numbers $\alpha = \{j_\alpha, \tau_\alpha, n_\alpha\}$, where j_α is the total angular momentum eigenvalue, τ_α is the isospin z-component eigenvalue and n_α counts subsequent energy eigenvalues within a given $\{j_\alpha, \tau_\alpha\}$ set. In this basis set the single-particle term of the Hamiltonian 4.37 is diagonal $\varepsilon_{\alpha\beta} = \varepsilon_{\alpha\beta}\delta_{\alpha\beta}$, and the interaction matrix elements $V_{\alpha\beta\gamma\delta}$ need to be evaluated for the implementation of the CI method. In the following we show a normalization procedure of single particle eigenstates as a preamble to the computation of interacting matrix elements.

The single-particle orbital states are obtained from the standard modulation [195] of Bloch states—localized at the lattice vectors—by the envelope wave functions (Eq. 4.2), slowly varying on the lattice-constant scale. Single-particle orbital states are

$$\phi_\alpha(\mathbf{r}) = \mathcal{M} \sum_\varsigma \Phi_\alpha^\varsigma(\mathbf{r}) \psi_{\tau_\alpha}^\varsigma(\mathbf{r}) \quad (4.43)$$

where the sum is performed over the index $\varsigma \in \{A, B\}$ ranging over the two sublattices. $\Phi_\alpha^\varsigma(\mathbf{r})$ incorporates the contributions of the envelope function $\Phi(\mathbf{r})$, eigenstate of the effective single-particle Hamiltonian Eq. 4.1 with energy eigenvalue ε_α . The conduction band Bloch functions $\psi_{\tau_\alpha}^\varsigma(\mathbf{r})$ at the Dirac points \mathbf{K} and \mathbf{K}' , are expressed in terms of the graphene $2p_z$ -orbitals $\varphi_{p_z}(\mathbf{r} - \mathbf{R}_\varsigma)$ centred on the \mathbf{R}_ς lattice vectors as

$$\psi_{\tau_\alpha}^\varsigma(\mathbf{r}) = \frac{e^{i\theta_\varsigma^{\tau_\alpha}}}{\sqrt{N_c}} \sum_{\mathbf{R}_\varsigma} e^{i\mathbf{K}^{\tau_\alpha} \cdot \mathbf{R}_\varsigma} \varphi_{p_z}(\mathbf{r} - \mathbf{R}_\varsigma), \quad (4.44)$$

where N_c is the number of unit cells and \mathbf{K}^{τ_α} refer to \mathbf{K} or \mathbf{K}' when the valley index is $\tau_\alpha = 1$ or $\tau_\alpha = -1$ respectively. The normalization constant \mathcal{M} can be determined from

the condition

$$\int |\phi_\alpha(\mathbf{r})|^2 d\mathbf{r} = 1, \quad (4.45)$$

and from the localization of the graphene p_z -orbitals respect to the envelope functions. Indeed, by inserting the expression Eq. 4.43 for the single particle states into Eq. 4.45 and explicitly summing over ς , the normalization condition, equivalent to

$$\begin{aligned} |\mathcal{M}|^2 \int [|\Phi_\alpha^A(\mathbf{r})\psi_{\tau_\alpha}^A(\mathbf{r})|^2 + |\Phi_\alpha^B(\mathbf{r})\psi_{\tau_\alpha}^B(\mathbf{r})|^2 + \\ [\Phi_\alpha^A(\mathbf{r})]^* \Phi_\alpha^B(\mathbf{r}) [\psi_{\tau_\alpha}^A(\mathbf{r})]^* \psi_{\tau_\alpha}^B(\mathbf{r}) + \\ [\Phi_\alpha^B(\mathbf{r})]^* \Phi_\alpha^A(\mathbf{r}) [\psi_{\tau_\alpha}^B(\mathbf{r})]^* \psi_{\tau_\alpha}^A(\mathbf{r})] d\mathbf{r} = 1, \end{aligned} \quad (4.46)$$

reduces to

$$|\mathcal{M}|^2 \int (|\Phi_\alpha^A(\mathbf{r})|^2 |\psi_{\tau_\alpha}^A(\mathbf{r})|^2 + |\Phi_\alpha^B(\mathbf{r})|^2 |\psi_{\tau_\alpha}^B(\mathbf{r})|^2) d\mathbf{r} = 1. \quad (4.47)$$

by considering the vanishing of the last two terms of Eq. 4.46 due to the orthogonality of two different Bloch states belonging to the same wave vector \mathbf{K}^{τ_α} . Let us explicitly write the square modulus of a Bloch state

$$|\psi_{\tau_\alpha}^A(\mathbf{r})|^2 = \frac{1}{N_c} \sum_{\mathbf{R}_A} \sum_{\mathbf{R}'_A} e^{i\mathbf{K}^{\tau_\alpha} \cdot (\mathbf{R}_A - \mathbf{R}'_A)} \varphi_{p_z}^*(\mathbf{r} - \mathbf{R}_A) \varphi_{p_z}(\mathbf{r} - \mathbf{R}'_A). \quad (4.48)$$

We see that the localized nature of the p_z orbitals give rise to two simplifying approximations. First, the two-centred overlaps between p_z orbitals are negligible

$$\varphi_{p_z}(\mathbf{r} - \mathbf{R}_\varsigma) \varphi_{p_z}(\mathbf{r} - \mathbf{R}'_{\varsigma'}) \approx |\varphi_{p_z}(\mathbf{r} - \mathbf{R}'_{\varsigma'})|^2 \delta_{\varsigma, \varsigma'} \delta_{\mathbf{R}_\varsigma, \mathbf{R}'_{\varsigma'}}. \quad (4.49)$$

Second, the localized nature of the p_z orbitals respect to the slowly varying envelope functions length scale allows to treat them as normalized delta functions

$$|\varphi_{p_z}(\mathbf{r} - \mathbf{R}_\varsigma)|^2 \approx \delta(\mathbf{r} - \mathbf{R}_\varsigma) \mathcal{V} \quad (4.50)$$

within a product with envelopes, \mathcal{V} is the overall finite volume of the system, including extension L_z of the p_z orbitals. The normalization condition for the p_z orbitals is

$$\int |\varphi_{p_z}(\mathbf{r} - \mathbf{R}_\varsigma)|^2 d\mathbf{r} = \mathcal{V}. \quad (4.51)$$

The above approximations Eqs. 4.50 and 4.49 simplify Eq. 4.47 into

$$\frac{|\mathcal{M}|^2 \mathcal{V}}{N_c} \sum_{\{\mathbf{R}_A\}} |\Phi_\alpha^A(\mathbf{R}_A)|^2 + \sum_{\{\mathbf{R}_B\}} |\Phi_\alpha^B(\mathbf{R}_B)|^2 = 1. \quad (4.52)$$

The sum over the lattice vectors can be substituted by a 2-fold integral taking into

account the slowly varying nature of the envelope functions respect to the lattice length scale

$$\sum_{\{\mathbf{R}_\zeta\}} |\Phi_\alpha^\zeta(\mathbf{R}_A)|^2 \approx \frac{N_\zeta}{\mathcal{A}} \int \int |\Phi_\alpha^\zeta(\mathbf{r})|^2 dx dy \quad (4.53)$$

where N_ζ/\mathcal{A} is the density of atomic sites belonging to the ζ sublattice and \mathcal{A} is the area of the QD. N_ζ coincides with half the number of atoms, i.e., with the number of graphene unit cells N_c . Therefore we obtain

$$\frac{|\mathcal{M}|^2 \mathcal{V}}{\mathcal{A}} \left[\int \int |\Phi_\alpha^A(x, y)|^2 dx dy + \int \int |\Phi_\alpha^B(x', y')|^2 dx' dy' \right] = 1 \quad (4.54)$$

which in circular coordinates $(x, y) = (\rho \cos \varphi, \rho \sin \varphi)$, after integration over the azimuthal angle coordinates reads ²

$$\int |\Phi_\alpha(\mathbf{r})|^2 d\mathbf{r} = \frac{2\pi |\mathcal{M}|^2 \mathcal{V}}{\mathcal{A}} \left[\int |\mathcal{R}_\alpha^A(\rho)|^2 \rho d\rho + \int |\mathcal{R}_\alpha^B(\rho')|^2 \rho' d\rho' \right]. \quad (4.55)$$

Finally the normalization condition Eq. 4.24 for the envelope function and Eq. 4.45 leads to

$$\frac{|\mathcal{M}|^2 \mathcal{V}}{\mathcal{A}} = 1, \quad (4.56)$$

from which, by considering that $\mathcal{V} = \mathcal{A}L_z$,

$$\mathcal{M} = \frac{1}{\sqrt{L_z}}. \quad (4.57)$$

We proceed by deducing the interaction matrix elements in the basis of single-particle states $\{\phi_\alpha\}$. We consider the forward scattering (FW) process that does not allow inter-valley transitions and involves small momentum transfer, therefore this scattering process is dominant among other allowed scattering processes [194]. Making explicit the isospin z -component eigenvalue in each set of quantum numbers $\alpha = \{a, \tau_\alpha\}$, $\beta = \{b, \tau_\beta\}$, $\gamma = \{c, \tau_\gamma\}$, $\delta = \{d, \tau_\delta\}$, the FW scattering valley selection rule is

$$\begin{cases} \tau \equiv \tau_\alpha = \tau_\delta \\ \bar{\tau} \equiv \tau_\beta = \tau_\gamma \end{cases} \quad (4.58)$$

that is, the isospin of each interacting electron is conserved. Below we derive an expression for the FW interaction matrix element involving only envelope spinors, employing the Bloch states tight-binding expansion, and the localization of the p_z orbitals with respect to the envelope functions length scale. The obtained expression is suitable for numerical calculations.

²the envelope functions depend on the angular variable φ only through a phase factor

From the single particle state expressions³ in terms of the envelope functions and Bloch states 4.43

$$\phi_\alpha(\mathbf{r}) = \mathcal{M} \sum_\zeta \Phi_{a,\tau}^\zeta(\mathbf{r}) \psi_\tau^\zeta(\mathbf{r}) \quad (4.59)$$

$$\phi_\beta(\mathbf{r}') = \mathcal{M} \sum_{\zeta'} \Phi_{b,\bar{\tau}}^{\zeta'}(\mathbf{r}') \psi_{\bar{\tau}}^{\zeta'}(\mathbf{r}') \quad (4.60)$$

$$\phi_\gamma(\mathbf{r}') = \mathcal{M} \sum_{\zeta''} \Phi_{c,\bar{\tau}}^{\zeta''}(\mathbf{r}') \psi_{\bar{\tau}}^{\zeta''}(\mathbf{r}') \quad (4.61)$$

$$\phi_\delta(\mathbf{r}) = \mathcal{M} \sum_{\zeta'''} \Phi_{d,\tau}^{\zeta'''}(\mathbf{r}) \psi_\tau^{\zeta'''}(\mathbf{r}) \quad (4.62)$$

and from the localization of the tight-binding orbitals (Eq. 4.49), which implies that the contributions with $\zeta' \neq \zeta''$ and $\zeta \neq \zeta'''$ can be neglected, the interaction matrix element 4.39 becomes

$$V_{\alpha\beta\gamma\delta} = |\mathcal{M}|^4 \int d\mathbf{r} \int d\mathbf{r}' \sum_s \sum_{\bar{s}} \Phi_{\tau,\bar{\tau}}^{s,\bar{s}}(\mathbf{r}, \mathbf{r}') [\psi_{\bar{\tau}}^{\bar{s}}(\mathbf{r})]^* [\psi_\tau^s(\mathbf{r}')]^* v(\mathbf{r}-\mathbf{r}') \psi_\tau^s(\mathbf{r}') \psi_{\bar{\tau}}^{\bar{s}}(\mathbf{r}) \quad (4.63)$$

where the definitions $s \equiv \zeta'' = \zeta'''$, $\bar{s} \equiv \zeta = \zeta'$, and

$$\Phi_{\tau,\bar{\tau}}^{s,\bar{s}}(\mathbf{r}, \mathbf{r}') \equiv [\Phi_{a,\bar{\tau}}^{\bar{s}}(\mathbf{r})]^* [\Phi_{b,\tau}^s(\mathbf{r}')]^* \Phi_{c,\tau}^s(\mathbf{r}') \Phi_{d,\bar{\tau}}^{\bar{s}}(\mathbf{r}) \quad (4.64)$$

have been introduced to simplify notation. In Eq. 4.63, the sum over s and \bar{s} involves four different lattice vectors ($\mathbf{R}_1^{\bar{s}}, \mathbf{R}_2^s, \mathbf{R}_3^s, \mathbf{R}_4^{\bar{s}}$) in the Bloch states expressions

$$\psi_{\bar{\tau}}^{\bar{s}}(\mathbf{r}) = \frac{e^{i\theta_{\bar{s}}}}{\sqrt{N_c}} \sum_{\mathbf{R}_1^{\bar{s}}} e^{i\mathbf{K}^{\bar{\tau}} \cdot \mathbf{R}_1^{\bar{s}}} \varphi_\pi(\mathbf{r} - \mathbf{R}_1^{\bar{s}}) \quad (4.65)$$

$$\psi_\tau^s(\mathbf{r}') = \frac{e^{i\theta_s}}{\sqrt{N_c}} \sum_{\mathbf{R}_2^s} e^{i\mathbf{K}^\tau \cdot \mathbf{R}_2^s} \varphi_\pi(\mathbf{r}' - \mathbf{R}_2^s) \quad (4.66)$$

$$\psi_\tau^s(\mathbf{r}') = \frac{e^{i\theta_s}}{\sqrt{N_c}} \sum_{\mathbf{R}_3^s} e^{i\mathbf{K}^\tau \cdot \mathbf{R}_3^s} \varphi_\pi(\mathbf{r}' - \mathbf{R}_3^s) \quad (4.67)$$

$$\psi_{\bar{\tau}}^{\bar{s}}(\mathbf{r}) = \frac{e^{i\theta_{\bar{s}}}}{\sqrt{N_c}} \sum_{\mathbf{R}_4^{\bar{s}}} e^{i\mathbf{K}^{\bar{\tau}} \cdot \mathbf{R}_4^{\bar{s}}} \varphi_\pi(\mathbf{r} - \mathbf{R}_4^{\bar{s}}), \quad (4.68)$$

which can be reduced to the sum over two lattice vectors \mathbf{R}^s and $\mathbf{R}^{\bar{s}}$ defined as $\mathbf{R}^s \equiv \mathbf{R}_2^s = \mathbf{R}_3^s$ and $\mathbf{R}^{\bar{s}} \equiv \mathbf{R}_1^{\bar{s}} = \mathbf{R}_4^{\bar{s}}$ by neglecting the overlaps between p_z orbitals centred at different lattice sites (Eq. 4.49), therefore

$$V_{\alpha\beta\gamma\delta} = \frac{|\mathcal{M}|^4}{N_c^2} \int d\mathbf{r} \int d\mathbf{r}' \sum_s \sum_{\bar{s}} \sum_{\mathbf{R}_s} \sum_{\mathbf{R}_{\bar{s}}} \Phi_{\tau,\bar{\tau}}^{s,\bar{s}}(\mathbf{r}, \mathbf{r}') |\varphi_\pi(\mathbf{r} - \mathbf{R}_{\bar{s}})|^2 |\varphi_\pi(\mathbf{r}' - \mathbf{R}_s)|^2 v(\mathbf{r} - \mathbf{r}'). \quad (4.69)$$

³note that we denote quantum numbers as lower indices and pseudospin components as upper indices to facilitate reading

Defining

$$\Phi_{\tau,\bar{\tau}}(\mathbf{r}, \mathbf{r}') \equiv \sum_s \sum_{\bar{s}} \Phi_{\tau,\bar{\tau}}^{s,\bar{s}}(\mathbf{r}, \mathbf{r}') \quad (4.70)$$

and taking into account the orbital localization Eq. 4.50, the matrix element becomes

$$V_{\alpha\beta\gamma\delta} = \frac{|\mathcal{M}|^4 \mathcal{V}^2}{N_c^2} \sum_{\mathbf{R}^s} \sum_{\mathbf{R}^{\bar{s}}} \Phi_{\tau,\bar{\tau}}(\mathbf{R}^{\bar{s}}, \mathbf{R}^s) v(\mathbf{R}^{\bar{s}} - \mathbf{R}^s) \quad (4.71)$$

The sums over the two lattice sites can be replaced by a 6-fold integral

$$V_{\alpha\beta\gamma\delta} = \frac{|\mathcal{M}|^4 \mathcal{V}^2}{N_c^2} \left(\frac{\Delta N_\zeta}{\Delta V} \right)^2 \int d\mathbf{r} \int d\mathbf{r}' \Phi_{\tau,\bar{\tau}}(\mathbf{r}, \mathbf{r}') v(\mathbf{r} - \mathbf{r}') \quad (4.72)$$

where $\frac{\Delta N_\zeta}{\Delta V} = \frac{N_c}{\mathcal{A}L_z} = \frac{N_c}{\mathcal{V}}$. Employing the normalization constant in Eq. 4.57 we obtain

$$V_{\alpha\beta\gamma\delta} = \frac{1}{L_z^2} \int d\mathbf{r} \int d\mathbf{r}' \Phi_{\tau,\bar{\tau}}(\mathbf{r}, \mathbf{r}') v(\mathbf{r}, \mathbf{r}'). \quad (4.73)$$

Up to this point, the interaction potential has not been made explicit. The strong localization of the p_z orbitals taken into account in the approximations Eq. 4.49 and 4.50 removes most of the contributions of the atomic orbitals. In order to recover the contribution of their short-range structure, the Ohno electron-electron interaction is considered. The Ohno interaction potential [200] is

$$v(\mathbf{r} - \mathbf{r}') = \frac{v_0}{\sqrt{1 + (\lambda^{-1}|\mathbf{r} - \mathbf{r}'|)^2}} \quad (4.74)$$

defined by

$$\lambda = \frac{e^2}{v_0 \kappa} \quad (4.75)$$

where κ is the relative static dielectric constant and e is the elementary charge. The potential approaches the long range Coulomb potential for large inter-particle distances $|\mathbf{r} - \mathbf{r}'|$ while for short distances it tends to $v_0 = 15$ eV [201], the Hubbard-like intra-atomic interaction. The interaction matrix element $V_{\alpha\beta\gamma\delta}$ is finite due to the Ohno short-distance cut-off.

We proceed from Eq. 4.73, then integration over the z and z' variables can be performed by replacing $(z - z')$ in the Ohno potential with the averaged extension $a_z = 3a_B$ of a p_z orbital written in terms of the Bohr radius a_B Å. As a result of such integration over the extent of p_z orbitals $[-L_z/2, L_z/2]$ the factor $1/L_z^2$ cancels.

The matrix element for the effective 2D Ohno potential in circular coordinates $(x, y) = (\rho \cos \varphi, \rho \sin \varphi)$ is

$$V_{\alpha\beta\gamma\delta} = \int_0^{+\infty} d\rho \int_0^{+\infty} d\rho' \int_0^{2\pi} d\varphi \int_0^{2\pi} d\varphi' \rho\rho' [\Phi_{\tau,\bar{\tau}}(\rho, \varphi; \rho', \varphi') v(\rho, \varphi; \rho', \varphi')] \quad (4.76)$$

where

$$v(\rho, \varphi; \rho', \varphi') = \frac{v_0}{\sqrt{1 + \lambda^{-2}[(\rho^2 + \rho'^2 - 2\rho\rho' \cos(\varphi - \varphi') + a_z^2)]}}. \quad (4.77)$$

The explicit form of the integrand factor that includes the envelope functions contribution, by recalling the decouple radial and angular parts in Eq. 4.2, becomes

$$\Phi_{\tau,\bar{\tau}}(\rho, \varphi; \rho', \varphi') = \sum_s \sum_{\bar{s}} \Phi_{\tau,\bar{\tau}}^{s,\bar{s}}(\rho, \varphi; \rho', \varphi') = e^{(j_d - j_a)\varphi} e^{(j_c - j_b)\varphi'} \sum_s \sum_{\bar{s}} \mathcal{R}_{\tau,\bar{\tau}}^{s,\bar{s}}(\rho, \rho') \quad (4.78)$$

where

$$\mathcal{R}_{\tau,\bar{\tau}}^{s,\bar{s}}(\rho, \rho') \equiv \mathcal{R}_{a,\bar{\tau}}^s(\rho) * \mathcal{R}_{b,\tau}^{\bar{s}}(\rho') * \mathcal{R}_{c,\tau}^s(\rho') \mathcal{R}_{d,\bar{\tau}}^{\bar{s}}(\rho) \quad (4.79)$$

and the $\mathcal{R}_{a,\bar{\tau}}^s(\rho)$, $\mathcal{R}_{b,\tau}^{\bar{s}}(\rho')$, $\mathcal{R}_{c,\tau}^s(\rho')$, $\mathcal{R}_{d,\bar{\tau}}^{\bar{s}}(\rho)$ functions are the s , \bar{s} components of the radial envelope function eigenstates of quantum numbers $\alpha = a, \tau$.

The interacting matrix element can be written as

$$V_{\alpha\beta\gamma\delta} = \int_0^{+\infty} d\rho \int_0^{+\infty} d\rho' \rho\rho' [\mathcal{R}_{\tau,\bar{\tau}}(\rho, \rho') I(\rho, \rho')] \quad (4.80)$$

using the compact notation

$$\mathcal{R}_{\tau,\bar{\tau}}(\rho, \rho') \equiv \sum_s \sum_{\bar{s}} \mathcal{R}_{\tau,\bar{\tau}}^{s,\bar{s}}(\rho, \rho'); \quad (4.81)$$

and

$$I(\rho, \rho') \equiv \int_0^{2\pi} d\varphi \int_0^{2\pi} d\varphi' [e^{i(j_d - j_a)\varphi} e^{i(j_c - j_b)\varphi'} v(\rho, \varphi; \rho', \varphi')]. \quad (4.82)$$

In the scattering process, the total angular momentum is conserved. This emerge immediately going into the angular coordinates $\xi = (\varphi - \varphi')/2$, $\eta = (\varphi + \varphi')/2$, in which, after some manipulation the only non zero part is such that $j_a + j_b = j_c + j_d$ and reads

$$I(\rho, \rho') = \frac{8v_0}{\sqrt{\frac{(\rho - \rho')^2 + a_z^2 + \lambda^2}{\lambda^2}}} \int_0^\pi d\xi \frac{(\pi - \xi) \cos([j_d - j_a + j_c + j_b]\xi)}{\sqrt{1 + \left[\frac{4\rho\rho'}{(\rho - \rho')^2 + a_z^2 + \lambda^2}\right]^2 \sin^2(\xi)}}. \quad (4.83)$$

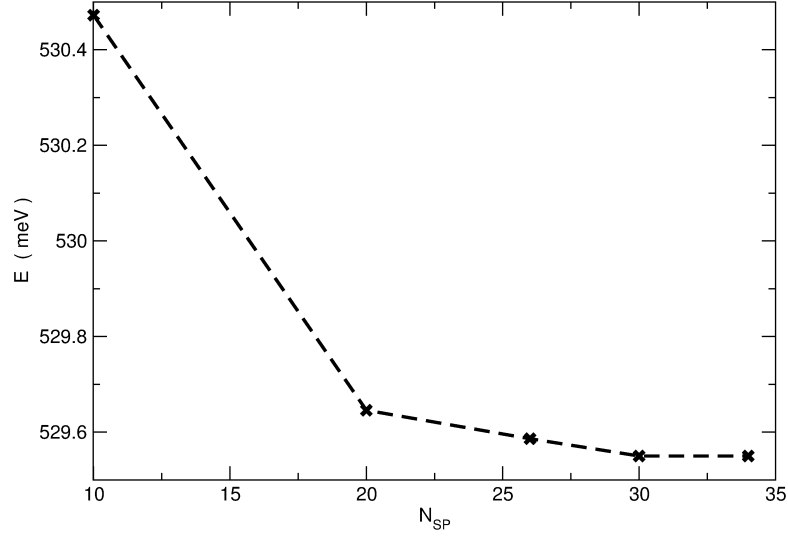


FIGURE 4.4: Ground state energy for $N = 2$, dot radius $R = 2250\text{\AA}$, $B = 0$ in the strong interacting regime characterized by $\epsilon = 2$. For $N_{SP} > 30$ the energy becomes stationary with the SP basis set size.

4.2.5 Numerical methods

We employed the FORTRAN code DONRODRIGO which implements the full CI method specifically to compute the lowest part of the energy spectrum of QDs also for highly interacting regimes. Details of its numerical implementation can be found in Ref. [199]. The input routines (computation of matrix elements) of the code and the post processing ones were adapted to tackle the details of the graphene QD system under consideration. The steps of the CI calculation are the following

- Selection of a pertinent basis set of N_{SP} single particle orbitals. The number of possible configurations increases exponentially with the electron number N and single particle states N_{SP} . This determine the computational cost of the method and therefore limits its use to a small number of interacting electrons. For a given N , the pertinent number of single-particle states N_{SP} is chosen by performing convergence tests, i.e., by increasing N_{SP} up to the point where the resulting energies are practically independent on the single-particle basis size. An example of typical convergence test is reported in Fig. 4.4 for $N = 2$, dot radius $R = 2250\text{\AA}$, zero magnetic field and a strong interacting regime characterized by small dielectric constant $\epsilon = 2$.
- Computation of the one-body and the two-body matrix elements respectively $\epsilon_{\alpha\beta}$ and $V_{\alpha\beta\gamma\delta}$ in the basis set of SP orbitals. The first matrix elements are immediately given because the chosen SP basis states are eigenvalues of \hat{H}_{SP} . The two-body matrix elements were computed by numerical integration of Eq. 4.80 in a Cartesian

grid whose extension was chosen by taking into account the exponentially decaying asymptotic behaviour of the SP orbitals, that are numerically null beyond $\rho = 3R$.

- Diagonalisation of the matrix eigenvalue problem (see. Section 4.2.3). This is the core of the numerical calculation, and employs as inputs the one-body and two-body matrix elements previously computed. The diagonalization proceeds within Hilbert space sectors of fixed (N, J_z, S_z, S) : we considered from $N = 2$ to $N = 6$ electrons, positive and negative values of the total angular momentum along the z-axis J_z and all the possible values of the square total spin S and the spin z-component $-N/2 \leq S_z \leq N/2$. For $N > 2$ the parallel version of the code is needed due to the huge dimension of the Hamiltonian (the maximum subspace dimension we diagonalise is of the order of 10^6), the diagonalization method is the Lanczos process implemented in the ARPACK library (PARPACK for the parallel version) that requires iterative multiplication of the matrix with arbitrary vectors and exploits the sparseness of the matrix to reduce the computational cost of large scale diagonalizations [202].

Chapter 5

Wigner localization in graphene quantum dots with a mass gap

In spite of unscreened Coulomb interactions close to charge neutrality, relativistic massless electrons in graphene allegedly behave as noninteracting particles. A clue to this paradox is that both interaction and kinetic energies scale with particle density in the same way. In contrast, in a dilute gas of nonrelativistic electrons the different scaling drives the transition to Wigner crystal. Here we present evidence that Dirac electrons in a graphene quantum dot with a mass gap localize à la Wigner for realistic values of device parameters. Our theoretical evidence relies on many-body observables obtained through the exact diagonalization of the interacting Hamiltonian, which allows us to take all electron correlations into account. We predict that the experimental signatures of Wigner localization are the suppression of the fourfold periodicity of the filling sequence and the quenching of excitation energies, which may be both accessed through Coulomb blockade spectroscopy. Our findings are relevant to other carbon-based nanostructures exhibiting a mass gap.¹

5.1 Theoretical model and single-particle properties

The envelope-function QD Hamiltonian for noninteracting electrons in the valley τ (Ref. [59]) is

$$\hat{H}_\tau = -i\hbar v_F (\hat{\tau}_1 \partial/\partial x + \hat{\tau}_2 \partial/\partial y) + \tau \Delta \hat{\tau}_3 + U(\rho) \hat{\tau}_0. \quad (5.1)$$

Here $v_F \approx 10^6$ m/s is the Fermi velocity, the 2×2 Pauli matrices $\hat{\tau}_1$, $\hat{\tau}_2$, $\hat{\tau}_3$, and the unit matrix $\hat{\tau}_0$ act on pseudospinors whose components are the A/B sublattice envelopes,

¹In this chapter an adapted version of the results published in Phys. Rev. B 90, 125446 (2014) is presented

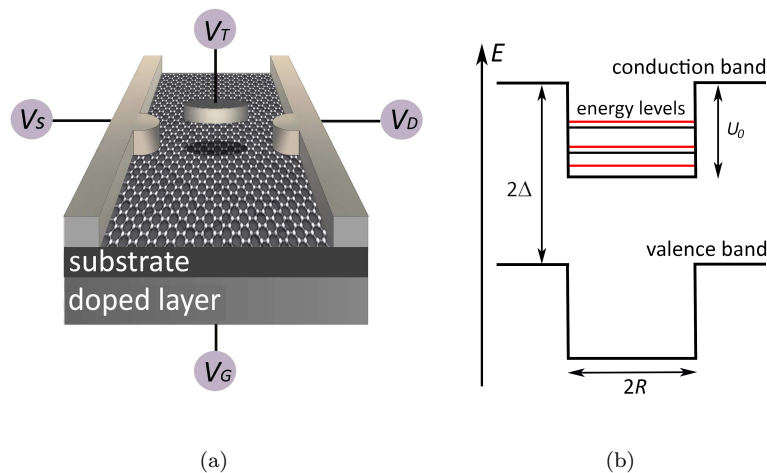


FIGURE 5.1: Graphene QD defined by electrostatic gates. (a) Proposed setup. The top gate (V_T) defines the dot while source (V_S), drain (V_D), and back (V_G) gates allow for Coulomb blockade spectroscopy. (b) Radial QD confinement potential. The interaction between graphene and substrate opens a mass gap 2Δ in the QD energy spectrum.

$U(\rho) = U_0 \Theta(\rho - R)$ is the circular hard-wall confinement potential of height U_0 plotted in Fig. 5.1(b), with R being the QD radius and $\rho = (x^2 + y^2)^{1/2}$. The potential U , modulated by the top gate shown in Fig. 5.1(a), confines the electrons in the QD since the Zeeman-like term $\Delta \hat{\tau}_3$ breaks sublattice inversion symmetry, hence inducing a gap 2Δ into the energy spectrum [Fig. 5.1(b)]. In the following we take $\Delta = U_0 = 0.26$ eV.

We find numerically the eigenvalues of \hat{H}_τ following the method of Ref. [59]. The QD bound states $\Phi(\mathbf{r})$ are pseudospinors of the form

$$\Phi(\mathbf{r}) = e^{i(j-1/2)\varphi} \begin{pmatrix} \mathcal{R}^A(\rho) \\ e^{i\varphi} \mathcal{R}^B(\rho) \end{pmatrix}, \quad (5.2)$$

where φ is the azimuthal angle, $j = \pm 1/2, \pm 3/2, \dots$ is the half-integer quantum number eigenvalue of the total angular momentum $\hat{j}_z = -i\hbar\partial/\partial\varphi + \hbar\hat{\tau}_3/2$, and $\mathcal{R}^A(\rho)$ [$\mathcal{R}^B(\rho)$] is the radial envelope on sublattice A [B] (Ref. [64]). As illustrated in Fig. 5.2(a) for the lowest conduction-band states, QD orbitals whose quantum numbers differ solely in the sign of τ (black or red [gray] lines) have different energies since inversion symmetry is broken, whereas time reversal symmetry protects $\varepsilon(\tau, j) = \varepsilon(-\tau, -j)$. Overall, including the spin degree of freedom $\sigma = \{\uparrow, \downarrow\}$, QD levels are four-fold degenerate. Both radial profiles and integrated weights of envelopes $\mathcal{R}(\rho)$ are generically different on the two sublattices, as shown in the example of Fig. 5.2(b). We consider a few excess interacting charge carriers populating the QD conduction band. The presence of the gap 2Δ allows us to ignore the pathologies that plague the many-body problem of Dirac electrons due

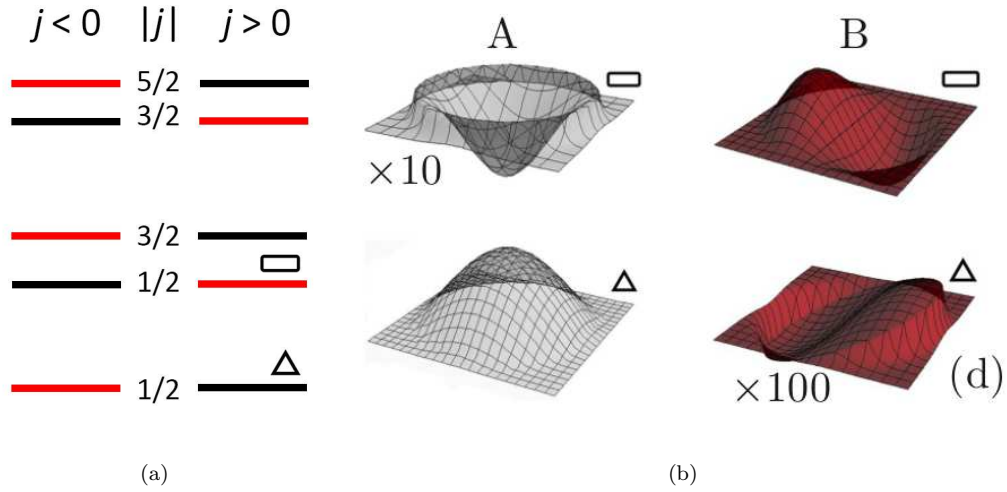


FIGURE 5.2: (a) Lowest non-interacting QD energy levels in the conduction band. Black (red [gray]) lines label states in K (K') valley. (b) Real part of sublattice-resolved envelopes whose energies are labeled by the square and triangle symbols in panel c.

to the unboundedness of the energy spectrum [203, 204]. The interacting Hamiltonian is

$$\hat{H} = \sum_{a\tau\sigma} \varepsilon_{a\tau} \hat{c}_{a\tau\sigma}^\dagger \hat{c}_{a\tau\sigma} + \frac{1}{2} \sum_{abcd} \sum_{\tau\tau'} \sum_{\sigma\sigma'} \langle a\tau, b\tau' | v(\mathbf{r} - \mathbf{r}') | c\tau', d\tau \rangle \hat{c}_{a\tau\sigma}^\dagger \hat{c}_{b\tau'\sigma'}^\dagger \hat{c}_{c\tau'\sigma'} \hat{c}_{d\tau\sigma}, \quad (5.3)$$

where $\hat{c}_{a\tau\sigma}^\dagger$ creates an electron of spin σ in the orbital $|a\tau\rangle$ labeled by quantum numbers τ and $a \equiv (j_a, n_a)$ whose energy is $\varepsilon_{a\tau}$ (n_a is the number of radial nodes). Two-body interaction takes the Ohno form $v(\mathbf{r} - \mathbf{r}') = v_0 [1 + (v_0\varepsilon/e^2)^2 |\mathbf{r} - \mathbf{r}'|^2]^{-1/2}$, where ε is the background relative dielectric constant. Since realistic values of ε fall in a wide range between $\varepsilon = 1.4$ and $\varepsilon = 44$, depending on the substrate [205] [206] [28] as well as on nearby gates, here we treat ε as a free parameter. At large distances v approaches the Coulomb potential, whereas its contact limit is the Hubbard-like intra-atomic interaction $v_0 = 15$ eV for the $2p_z$ orbital [200]. Matrix elements $\langle a\tau, b\tau' | v | c\tau', d\tau \rangle$ are obtained from tight-binding states neglecting interatomic orbital overlaps [194] as well as small intervalley exchange terms [207].

The many-body states are superpositions of the Slater determinants obtained by filling the lowest 68 spin-valley-orbitals with N electrons in all possible ways (aka full configuration interaction [199]). This size of the truncated single-particle basis set was chosen after checking that the computed many-body ground-state energy is well converged. In the Fock basis of Slater determinants \hat{H} is a sparse matrix, with blocks labeled by the total angular momentum and (iso)spin. The maximum linear size of the matrix

is 2,187,712, which we diagonalize with the home-built parallel code DONRODRIGO [43, 44, 45, 199]. This provides highly accurate energies and wave functions of both ground and excited states, in contrast to other high-level methods, such as quantum Monte Carlo, addressing ground state properties only.

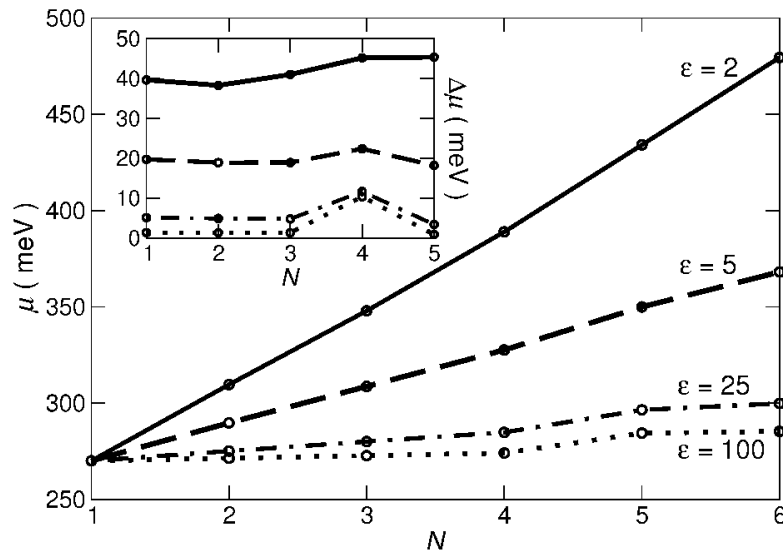


FIGURE 5.3: Coulomb blockade linear spectroscopy. Chemical potential $\mu(N)$ vs electron number N for different background dielectric constants ε , with radius $R = 250 \text{ \AA}$. Inset: Charging energy $\Delta\mu(N)$ vs N . Lines are guides to the eye. $\Delta\mu$ may be measured as electrons are added to the quantum dot one by one tuning the backgate shown in Fig. 5.1(a).

5.2 Coulomb blockade spectroscopy

A key quantity we obtain from the computed ground state energies $E_0(N)$ is the chemical potential $\mu(N) = E_0(N) - E_0(N - 1)$, that is the resonating tunneling energy of the N th electron injected into the QD containing $N - 1$ interacting particles. This may be measured through Coulomb blockade spectroscopy, as electrons are added to the QD one by one tuning the backgate shown in Fig. 5.1(a) [117]. In Fig. 5.3 we artificially modulate the background screening ε to highlight the effect of Coulomb interaction on the filling sequence (here $R = 250 \text{ \AA}$). In the absence of interactions ($\varepsilon = 100$, dotted line), $\mu(N)$ is constant except for a step when adding the fifth electron, which corresponds to a peak in the charging energy $\Delta\mu(N) = \mu(N + 1) - \mu(N)$ (see inset). This finite value $\Delta\mu(N = 4) \approx 10 \text{ meV}$ is the orbital energy cost required to add an electron to the second shell after the first one has been filled with four electrons. This fourfold periodicity is generic for all fillings, as clear from Fig. 5.2(a).

As the interaction strength is turned on, the shell structure of $\mu(N)$ is progressively washed out. In contrast with circular QDs in ordinary semiconductors [208], the charging

energy $\Delta\mu$ shown in the inset of Fig. 5.3 neither exhibits half-shell peaks linked to Hund's rule nor decreases with N . The former feature, shared by carbon-nanotube QDs [45, 193], is due to the spin-valley multicomponent nature of the wave function. In fact, at the noninteracting level the four-fold degenerate spin-valley projections are linked to a single orbital state, hence there is no Hund's rule, which is associated with the partial filling of a degenerate manifold of separate orbital states. The latter feature is peculiar to the hard-wall confinement potential, as in the case of ordinary semiconductors the potential is soft so the dot size L increases with N whereas the charging energy $\Delta\mu = e^2/C$ decreases with N ($C \sim L$ is the QD capacitance).

For realistic values of ε the Coulomb energy overwhelms the kinetic energy, making μ increase almost linearly with N (dashed and solid lines in Fig. 5.3 for $\varepsilon = 5$ and 2, respectively).

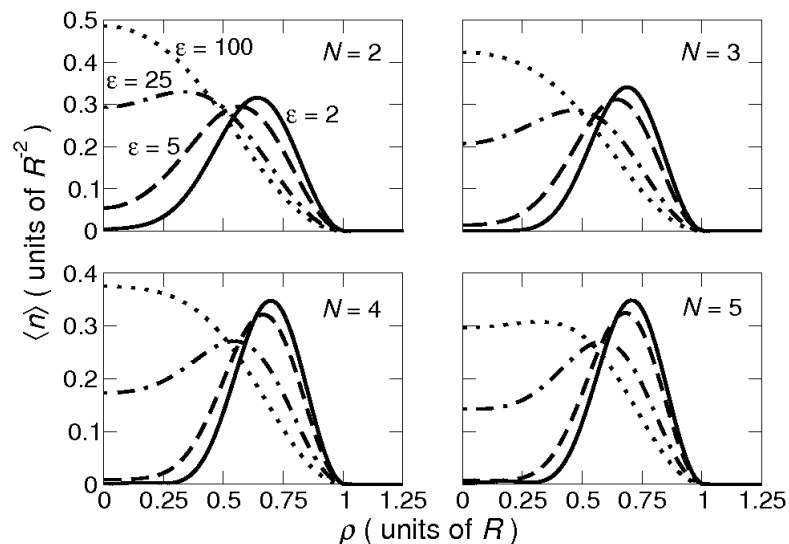


FIGURE 5.4: Emergence of radial correlations in the wave function. One-body density $\langle n(\mathbf{r}) \rangle$ vs radial coordinate ρ for different values of dielectric constant ε and electron number N , with radius $R = 1250$ Å. Realistically screened mutual interactions push electrons against the QD potential wall.

5.3 Emergence of radial correlations

To clarify how interactions affect the wave function we compute the—circularly symmetric— one-body density

$$\langle n(\mathbf{r}) \rangle = \frac{1}{N} \sum_{i=1}^N \langle \delta(\mathbf{r} - \mathbf{r}_i) \rangle, \quad (5.4)$$

where $\langle \dots \rangle$ is the quantum statical average for vanishing temperature. In practice, we average $\langle n(\mathbf{r}) \rangle$ over the ground-state multiplet, whose large angular-momentum degeneracy is protected by symmetry against the effect of interaction. After the averaging

$\langle n(\mathbf{r}) \rangle$ is the same on both sublattices, unspecified in the following. Figure 5.4 shows the

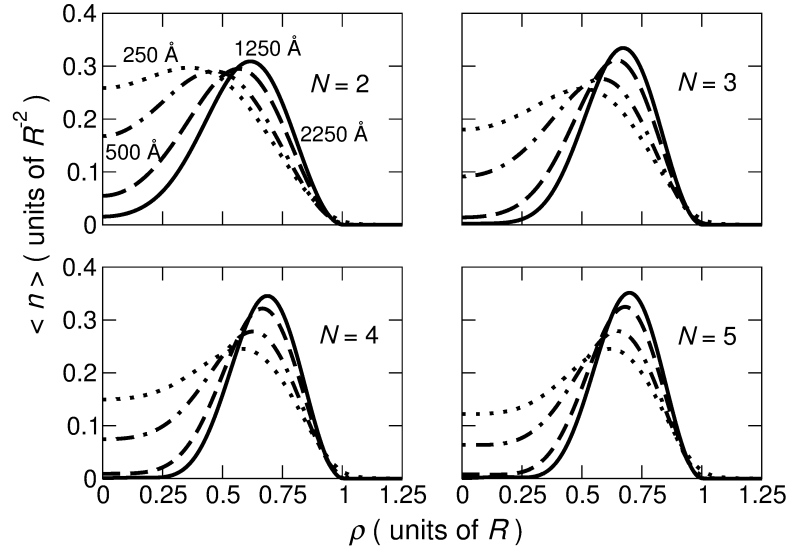


FIGURE 5.5: One-body density $\langle n(\mathbf{r}) \rangle$ vs radial coordinate ρ for different values of the dot radius and electron number N . The dielectric constant is $\varepsilon = 5$. The ring structure is more pronounced for larger dot radius.

evolution of the radial profile of $\langle n(\mathbf{r}) \rangle$ with the interaction strength. Whereas for large screening (dotted lines) the probability weight is spread all over the QD, as ε is decreased the central region is depleted with its weight being moved towards the dot wall. For realistic screening (dashed and solid lines) $\langle n \rangle$ is a ring with electrons pushed against the potential wall by Coulomb repulsion, which hints to the formation of a Wigner molecule [41]. This trend is generic for different electron numbers and dot radii, as shown in Fig. 5.5 the larger R the more pronounced ring structure at a given ε .

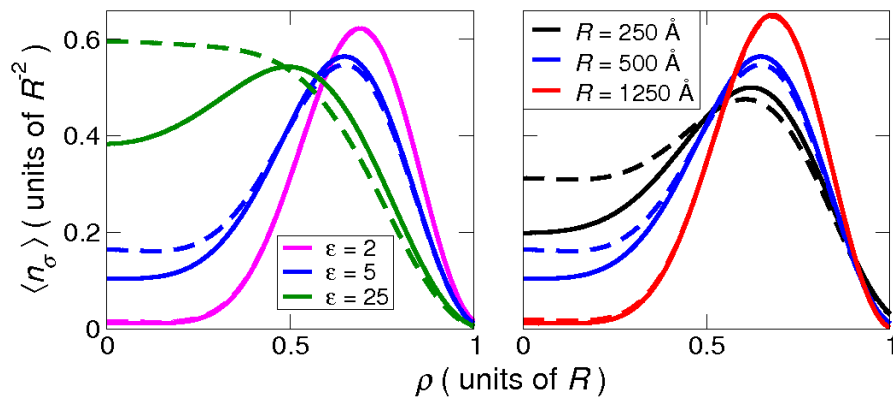


FIGURE 5.6: Suppression of exchange interactions. Spin-resolved density $\langle n_\sigma(\mathbf{r}) \rangle$ vs radial coordinate ρ for different values of dielectric constant ε (left panel, $R = 500 \text{ \AA}$) and radius R (right panel, $\varepsilon = 5$), with $N = 5$ and spin projection $S_z = 1/2$. Solid and dashed lines point to $\langle n_\uparrow \rangle$ and $\langle n_\downarrow \rangle$, respectively. Wigner localization depletes the probability weight in the regions halfway an electron and its neighbors and hence suppresses exchange interactions, inducing large spin degeneracies.

5.4 Suppression of exchange interactions

A fingerprint of Wigner localization is provided by the spin-resolved one-body density $\langle n_\sigma(\mathbf{r}) \rangle$,

$$\langle n_\sigma(\mathbf{r}) \rangle = \frac{1}{N_\sigma} \sum_{i=1}^N \langle \delta_{\sigma\sigma_i} \delta(\mathbf{r} - \mathbf{r}_i) \rangle_{S_z}. \quad (5.5)$$

Here N_σ is the number of electrons with spin σ so $\langle n_\sigma(\mathbf{r}) \rangle$ is normalized to one, and $\langle \dots \rangle_{S_z}$ is the average taken over the manifold of states with fixed total spin projection $S_z = (N_\uparrow - N_\downarrow)/2$. For odd electron numbers $\langle n_\uparrow(\mathbf{r}) \rangle$ and $\langle n_\downarrow(\mathbf{r}) \rangle$ generically differ, as illustrated in Fig. 5.6 for five electrons and $S_z = 1/2$. However, as the interaction strength is increased by either suppressing screening (left panel) or increasing the dot size (right panel), the radial profiles of $\langle n_\uparrow \rangle$ (solid lines) and $\langle n_\downarrow \rangle$ (dashed lines) tend to overlap and form the same probability density ring [43]. The rationale is that Coulomb forces localize electrons in space, depleting the probability weight in the regions halfway an electron and its neighbours. Therefore, exchange interactions between pairs of electrons are suppressed, making spin degrees of freedom redundant.

5.5 Emergence of angular correlations

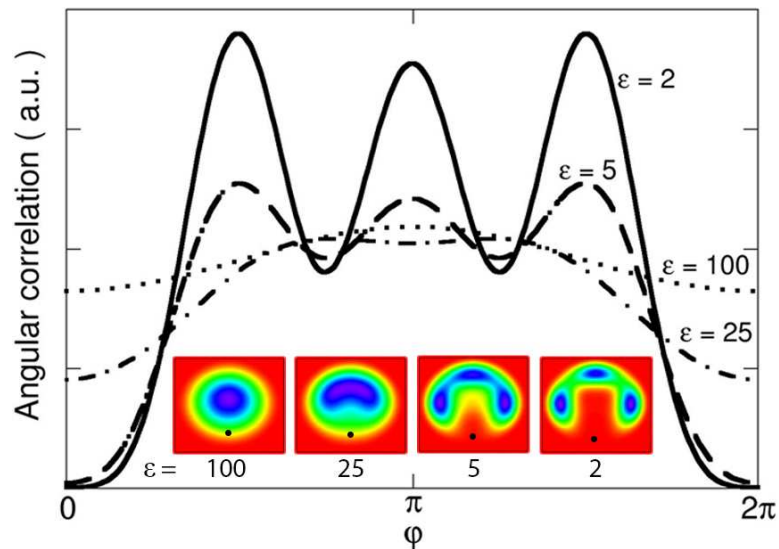


FIGURE 5.7: Pair correlation function $P(\mathbf{r}, \mathbf{r}_0)$ vs angle φ with $|\mathbf{r}| = |\mathbf{r}_0|$ for four electrons and different values of dielectric constant ε , with $R = 500 \text{ \AA}$. Inset: corresponding contour plots of $P(\mathbf{r}, \mathbf{r}_0)$ in the xy plane. Increasing the interaction strength leads to the formation of the correlation hole as well as the development of angular correlations, which enforce a square Wigner molecule.

To detect whether angular correlations are enforced by interactions we break the circular symmetry of the one-body density introducing the pair correlation function $P(\mathbf{r}, \mathbf{r}_0)$, i.e.,

the conditional probability of finding an electron at \mathbf{r} provided another electron is located at the fixed position \mathbf{r}_0 displaced from the origin,

$$P(\mathbf{r}, \mathbf{r}_0) = \frac{1}{N(N-1)} \sum_{\sigma_1, \sigma_2, \dots, \sigma_N} \int d\mathbf{r}_3 d\mathbf{r}_4 \dots d\mathbf{r}_N |\psi(\mathbf{r}, \sigma_1; \mathbf{r}_0, \sigma_2; \mathbf{r}_3, \sigma_3; \dots; \mathbf{r}_N, \sigma_N)|^2. \quad (5.6)$$

For the sake of simplicity, here we take the quantum average over a selected pure quantum state ψ belonging to the ground-state multiplet and show the sublattice component with the largest weight.

The insets of Fig. 5.7 show how the contour plots of $P(\mathbf{r}, \mathbf{r}_0)$ for four electrons evolve in the xy plane as screening is suppressed. The black dots highlight the positions \mathbf{r}_0 of the fixed electron, located at the maximum of of the one-body density with arbitrary angle. As the interaction strength increases [panels from left ($\varepsilon = 100$) to right ($\varepsilon = 2$)], we see—beyond the onset of the correlation hole around the fixed particle—a strong rearrangement of the probability weight: a non-trivial structure emerges made of three peaks located at the vertices of a square whose last vertex is placed at \mathbf{r}_0 . Overall, the three peaks plus the fixed electron realize a square Wigner molecule, which rotates together with \mathbf{r}_0 .

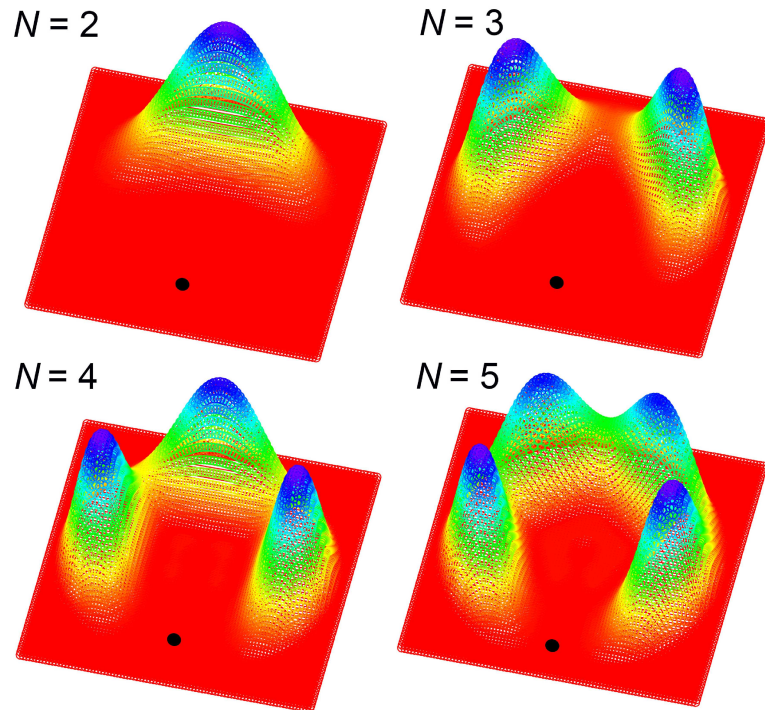


FIGURE 5.8: Three-dimensional contour plots of pair correlation functions $P(\mathbf{r}, \mathbf{r}_0)$ for $\varepsilon = 2$ and $R = 2250 \text{ \AA}$. Black dots point to the locations \mathbf{r}_0 of fixed electrons.

Cutting the contour plots of $P(\mathbf{r}, \mathbf{r}_0)$ along a ring of radius $|\mathbf{r}_0|$ allows us to appreciate the role of interactions in driving spatial order and localization, as we show in Fig. 5.7. For weak correlations (dotted line) P vs φ is featureless, exhibiting a minor depression close to $\varphi = 0, 2\pi$, which realizes the exchange hole around the fixed electron position. Increasing the interaction (up to $\varepsilon = 2$, solid line) the three peaks of the square Wigner molecule emerge together with a deep correlation hole around \mathbf{r}_0 , the peak-to-valley ratio increasing with decreasing ε .

Figure 5.8 shows the generic behavior of N electrons in the strongly correlated limit, here enforced with $\varepsilon = 2$ and $R = 2250 \text{ \AA}$. The electrons realize Wigner molecules whose forms are regular polygons with N vertices, as illustrated by the three-dimensional plots of $P(\mathbf{r}, \mathbf{r}_0)$ for the dimer ($N = 2$), the triangle ($N = 3$), the square ($N = 4$), and the pentagon ($N = 5$).

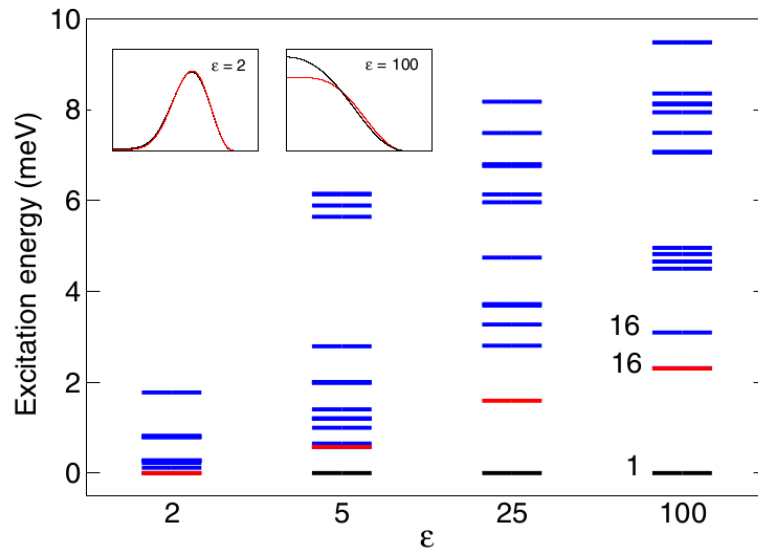


FIGURE 5.9: Excitation spectrum of a Wigner molecule. Low-lying excitation energies vs dielectric constant ε for $N = 4$ and $R = 500 \text{ \AA}$. Numbers label degeneracies of selected multiplets. Insets: density $n(\mathbf{r})$ vs radial coordinate ρ averaged over the ground state (black curve) and the first excited multiplet (red [gray] curve). The Wigner-molecule ground state is highly degenerate as localized electrons may independently flip their (iso)spins.

5.6 Excitation spectrum

The excitation spectrum of a Wigner molecule may be measured by either non-linear Coulomb blockade spectroscopy [45]—opening the source-drain bias window in the setup of Fig. 5.1(a)—or inelastic light scattering [43, 44]. Figure 5.9 shows the dependence of low-lying excitation energies on the interaction strength for four electrons. For weak interactions ($\varepsilon = 100$), the spectrum reminds us of the single-particle ladder of levels

of Fig. 5.2(a), as to excite the ground state one moves an electron from the lowest completely filled shell to higher orbital states. Whereas in this specific case the ground state is non degenerate, the excited multiplets exhibit large degeneracies (labeled by numbers) linked to different (iso)spin orientations. For stronger interactions, the lowest excitation energies are strongly quenched as the system turns into a square Wigner molecule. Comparing the one-body density $n(\mathbf{r})$ of the ground-state (black curves in the insets) with $n(\mathbf{r})$ averaged over the lowest excited multiplet (red [gray] curves), we see that the two curves overlap for strong interactions (left inset, $\varepsilon = 2$). In fact, in the limit of perfect localization the Wigner-molecule ground state exhibits a huge degeneracy since localized electrons may independently flip their (iso)spins, as exchange interactions are completely suppressed. Therefore, the energy spectrum of the Wigner molecule is a ladder of highly-degenerate rotovibrational quanta [41, 43, 44].

Chapter 6

Few-body energy spectrum in the presence of a magnetic field

We present the energy spectrum of few interacting electrons confined in a clean, circular graphene quantum dot with a mass gap induced by the breaking of sublattice symmetry, in the presence of a perpendicular magnetic field. We demonstrate that the modifications of the magnetic dependence of the dot energy spectrum, accessible through magnetic-field spectroscopy measurements, provide an indication of the degree of electronic correlation, reaching the limit of electron localization. The results rely on the combined analysis of few-body spectra and two-point correlation functions obtained from the exact diagonalisation of the interacting Hamiltonian.

6.1 Single-particle energy spectrum

We start recalling the continuum model that describe the QD low-energy scale dynamics of single electrons. In this model, we recall, the Hamiltonian is

$$H_\tau = -i\hbar v_F [\hat{\tau}_1(\partial_x + eA_x) + \hat{\tau}_2(\partial_y + eA_y)] + \tau\Delta\hat{\tau}_3 + U(\rho)\hat{\tau}_0, \quad (6.1)$$

near each graphene valley K(K') identified by the valley index $\tau = 1(-1)$. An homogeneous magnetic field $\vec{B} = B\hat{z}$, normal to the graphene plane, is included within minimal coupling. We choose the symmetric gauge for the vector potential $\vec{A} = (A_x, A_y, A_z) = \frac{B}{2}(-y, x, 0) = \frac{B}{2}(-\rho\sin(\varphi), \rho\cos(\varphi), 0)$, here $\rho = (x^2 + y^2)^{1/2}$ and φ is the azimuthal angle. In Eq. 6.1, $v_F = 10^6$ m/s denotes the Fermi velocity module, $(\partial_x \equiv \partial/\partial x, \partial_y \equiv \partial/\partial y)$ denote derivatives respect to the indicated coordinate. We recall that the 2×2 Pauli matrices $\hat{\tau}_{1,2,3}$ and the unit matrix $\hat{\tau}_0$ act on the two components of the envelope

wave function encoding the A and B (pseudospin) sublattices honeycomb structure of graphene. The constant mass term $\tau\Delta\hat{\tau}_3$ accounts for the lifting of the inversion symmetry between the carbon sublattices opening a gap of 2Δ in the energy spectrum. The potential asymmetry between lattice sites may be induced by the interaction with a periodic substrate (see Section 2.3.2). The last term in Eq. 6.1 includes the hard-wall confinement potential $U(\rho) = U_0\Theta(\rho - R)$ of height U_0 (here Θ is the Heaviside step-function), determining the dot region of radius R . The isotropy of the Hamiltonian implies that the ‘‘pseudospin-orbital’’ total angular momentum along the transverse z -direction $\hat{j}_z = -i\hbar\partial/\partial\varphi + \hbar\hat{\tau}_3/2$ is conserved and the single-particle solutions to the Dirac equation $\hat{H}_\tau\Phi(\rho, \varphi) = \varepsilon\Phi(\rho, \varphi)$ are simultaneous eigenfunctions of \hat{H}_τ and \hat{j}_z

$$\Phi(\rho, \varphi) = e^{i(j-1/2)\varphi} \begin{pmatrix} \mathcal{R}^A(\rho) \\ e^{i\varphi}\mathcal{R}^B(\rho) \end{pmatrix} \quad (6.2)$$

with \hat{j}_z eigenvalue $\hbar j$, $j = m + 1/2$, $m \in \mathbb{Z}$. The radial components of the bound-state solutions $\mathcal{R}(\rho) = [\mathcal{R}^A(\rho), \mathcal{R}^B(\rho)]^T$ are hypergeometric functions regular at the origin and decaying asymptotically inner and outer the dot respectively. We obtained numerically the single-particle energies from the energy quantization condition $\mathcal{R}(\rho < R) = \mathcal{R}(\rho > R)$. The deduction of both the secular equation and the bound-state solutions is described in detail in Section 4.1.0.1.

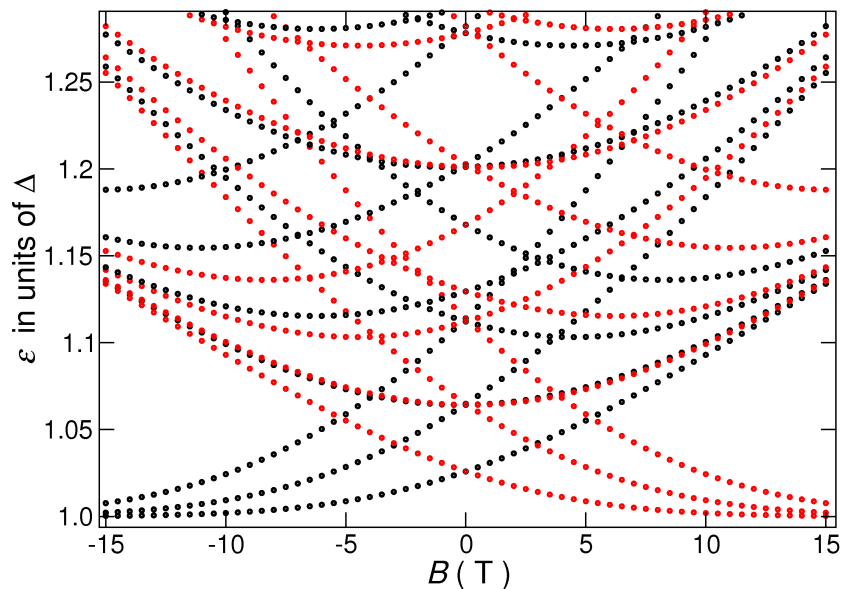


FIGURE 6.1: SP energy spectrum for $j = \pm 1/2, \pm 1/3, \pm 5/2$. Black (red) color refers to the $\tau = 1$ ($\tau = -1$) valley. The valley degeneracy at $B = 0$ is broken for finite magnetic field B . The SP levels merge into the graphene Landau levels for high values of B . Energies are given in units of half band-gap Δ .

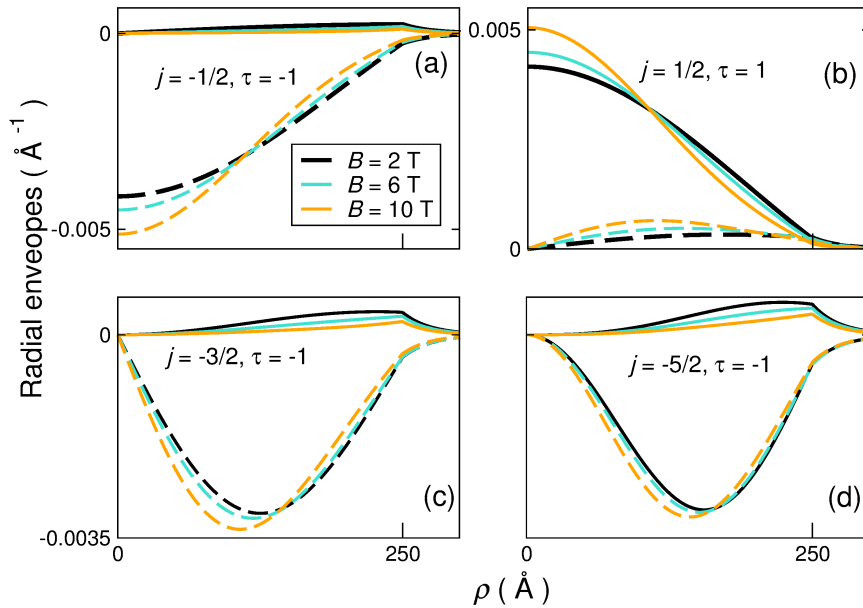


FIGURE 6.2: \mathcal{R}^A (continuous lines) and $\mathfrak{S}(\mathcal{R}^B)$ (dashed lines) sublattice components of representative single-particle radial envelopes (at different B values), corresponding to lowest-energy levels with quantum numbers $[j, \tau]$: (a) $[-1/2, -1]$ (b) $[1/2, 1]$ (c) $[-3/2, -1]$ (d) $[-5/2, -1]$. Dot radius $R = 250 \text{ \AA}$.

The single particle energy spectrum of the confined states in the conduction band—obtained numerically—of a dot of radius $R = 250 \text{ \AA}$, is shown in Fig. 6.1, for a wide range of magnetic field values. Note that at zero magnetic field, $\varepsilon(j, \tau) = \varepsilon(-j, -\tau)$, therefore single-particle levels are four-fold degenerate due to valley and spin degrees of freedom. Such symmetry is lifted at finite magnetic field as it is shown in Fig. 6.1 while $\varepsilon(j, \tau, B) = \varepsilon(-j, -\tau, -B)$ (see Section 4.1.0.3). In the limit of large magnetic fields the single-particle energy levels merge into the lowest Landau levels $\varepsilon_n/\Delta = \sqrt{1 + 2n(v_F\hbar)^2/(\Delta l_B)^2}$, where $n = 1, 2, \dots$ and $l_B = \sqrt{\hbar/eB}$ is the magnetic length. They include the zero mode ($n = 0$) Landau level peculiar of graphene (see Section 2.2.3) $\varepsilon_0/\Delta = 1$, which is valley-polarized. Note that the energy of the levels approaching the zero mode ($n = 0$) Landau level decreases for increasing magnetic field¹. For realistic dot radius, the Zeeman splitting $g\mu_B B$ is negligible respect to the SP level spacing so it is here ignored².

A zoom over low-lying energy levels for positive magnetic field values is shown in Fig. 6.3(a), including states of $|j|$ up to $11/2$ denoted by dashed (dotted-dashed) lines for $j > 0$ ($j < 0$), with black (red) colors distinguishing the valleys $\tau = 1(-1)$. For the highlighted levels, the quantum numbers $[j, \tau]$ are indicated. We show in Fig. 6.2 the A [\mathcal{R}^A] and B [$\mathfrak{S}(\mathcal{R}^B)$] sublattice components of representative single-particle radial

¹this is in contrast to semiconductor QDs energy levels merging the Landau-levels, which energy increases for increasing magnetic field

²for instance, at $B = 10 \text{ T}$ the Zeeman splitting is one order of magnitude smaller than the lowest SP level spacing

envelopes, corresponding to the lowest energy levels of Fig. 6.3(a). Note that the prevalent sublattice component is different in each valley, being A (B) for $\tau = 1$ ($\tau = -1$). The effect of increasing the magnetic field is to increase the relative weight of the B component³ and to displace the amplitude toward the dot center.

6.2 Evolution of Coulomb resonances in a perpendicular magnetic field

We consider few electrons in the conduction band interacting through the Ohno potential

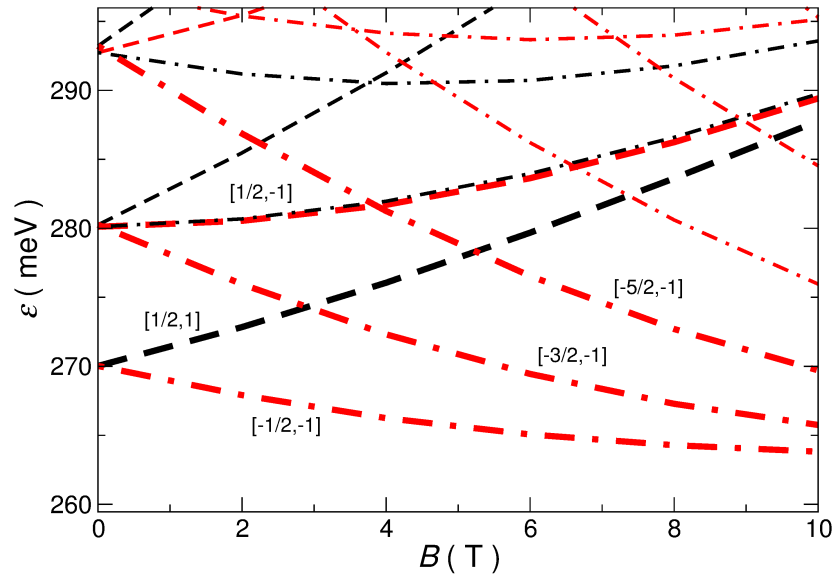
$$v(\mathbf{r} - \mathbf{r}') = \frac{v_0}{\sqrt{1 + (\lambda^{-1}|\mathbf{r} - \mathbf{r}'|)^2}} \quad (6.3)$$

defined by $\lambda \equiv e^2/v_0\varepsilon$, where ε is the background relative dielectric constant. The Ohno interaction potential accounts for the long-range Coulomb interaction at large interparticle distances $|\mathbf{r} - \mathbf{r}'|$ and for the short-range structure of the $2p_z$ atomic orbitals by approaching, at short interparticle distances, the energy cost of localizing two electrons on the same carbon site $v_0 = 15$ eV [200]. In the following, we inquire how quantities accessible by magneto-tunneling spectroscopy, i.e., the Coulomb blockade resonance evolution as a function of the magnetic field, may change as the interaction strength increases. To this aim, the interacting problem up to $N = 5$ electrons was numerically solved through the Configuration Interaction (CI) method (see Section 4.2), for a wide range of magnetic field values and interaction regimes. The interaction strength is tuned by varying the background dielectric constant ε . The obtained few-body ground- and excited-states are labelled by the total quantum numbers (J_z, S, T_z) , i.e., the total "pseudospin-angular" momentum J_z , the total spin S and the total isospin z -component T_z respectively. All numerical results shown here refer to a QD of radius $R = 250$ Å, the mass parameter and the potential depth (see Eq. (6.1)) being fixed to $\Delta = U_0 = 0.26$ eV. From the exact N -body ground-state energy $E_0(N)$ and the i th excited-state energy $E_i(N)$, we compute the chemical potential $\mu(N)$ of the N th electron tunneling into the QD at a given magnetic field B

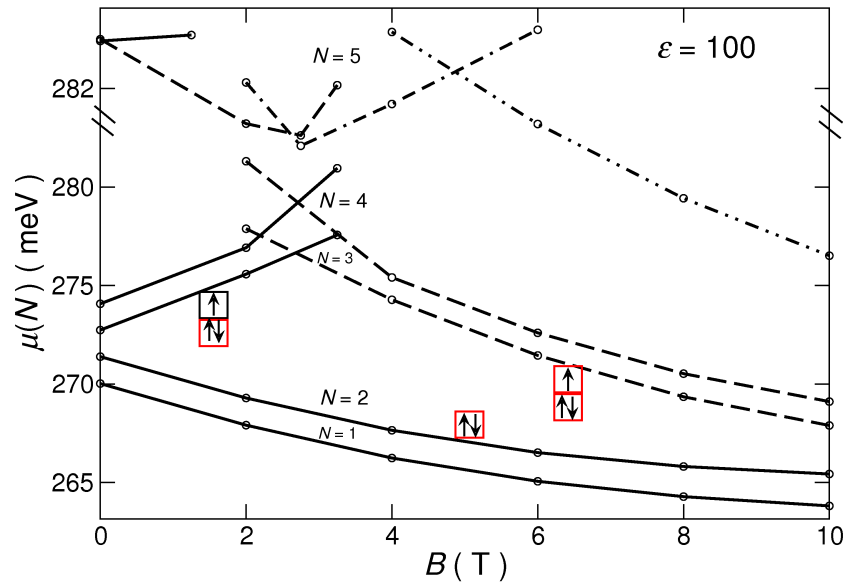
$$\mu_{(0)i}(N) = E_{(0)i}(N) - E_0(N - 1). \quad (6.4)$$

Fig. 6.3(b) depicts, for weak interaction strength, i.e., for dielectric constant $\varepsilon = 100$, $\mu(N)$ vs B up to $N = 5$ electrons. For a given N , by following the lowest curves, $\mu_0(N)$ is traced. Excited-state contributions $\mu_i(N)$ near each kink are also depicted. Upward

³the lowest LLs are sublattice polarized, i.e., their wave functions amplitudes are non-zero only in one of the sublattices



(a)



(b)

FIGURE 6.3: (a) SP levels for $j = \pm 1/2, \dots, \pm 11/2$. Same color code of Fig. 6.1, black (red) lines corresponds to valley $\tau = 1$ ($\tau = -1$). Dashed-lines depict $j > 0$ levels whereas dashed-dotted lines correspond to $j < 0$ levels. Emphasized levels are denoted by the quantum numbers $[j, \tau]$. (b) Chemical potential $\mu(N)$ in the weakly interacting regime, i.e., $\varepsilon = 100$, for a dot of radius $R = 250 \text{ \AA}$. The behaviour is determined by the consecutive filling of the SP levels of panel (a).

cusps of the chemical potential identify crossings between different N -body ground-states as the magnetic field changes. In this weakly interacting regime, the behaviour of the chemical potential is basically determined by the non-interacting energy spectrum

structure, as highlighted by the comparison of Fig. 6.3(b) with the emphasized curves (thick lines) of Fig. 6.3(a). The occupation of a SP orbital in the $\tau = 1$ ($\tau = -1$) valley corresponds to a positive (negative) $\mu_0(N)$ slope. Note that the maximum for $\mu_0(4)$ around $B = 3$ T corresponds to the minimum for $\mu_0(5)$ and that the first and second curves are paired as well as the third and fourth curves. In fact, the lowest SP levels (Fig. 6.3(a)) are filled sequentially by opposite-spin electrons, according with the Pauli exclusion principle. The pair of curves ($N = 1$ and $N = 2$) and ($N = 3$ and $N = 4$) do not overlap because of finite interaction. We now progressively increase the interaction

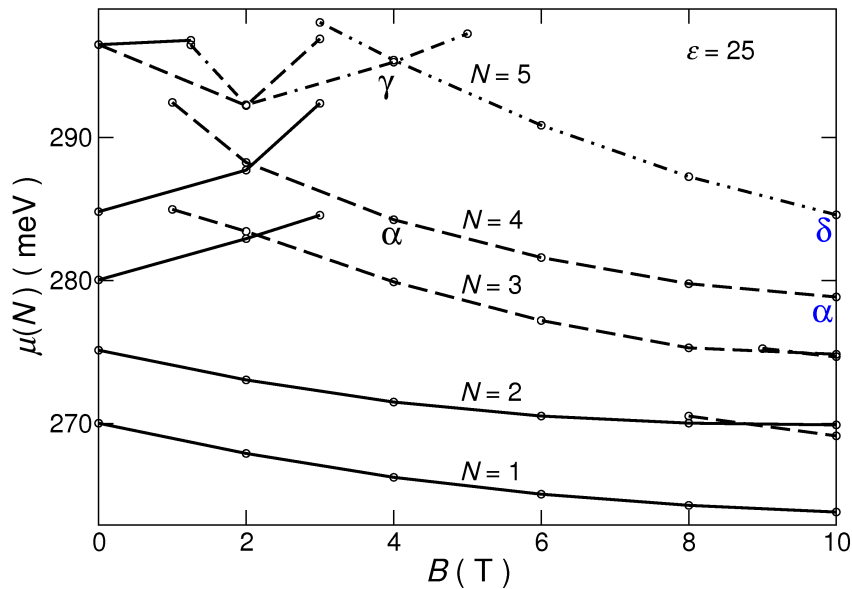


FIGURE 6.4: Chemical potential $\mu(N)$ vs magnetic field B for $\varepsilon = 25$, with dot radius $R = 250$ Å. The ground-state transitions at high magnetic fields are due to interaction.

strength by lowering the screening. For $\varepsilon = 25$ (see Fig. 6.4), the curves still resemble the single-particle level structure but the kinks appear for lower B values with respect to the crossings shown in Fig. 6.3(b). New ground-state transitions arise at higher magnetic field values: for $N = 2$ at $B_c \approx 8.8$ T and for $N = 3$ at $B_c \approx 9.5$ T. These two transitions—on which we focus in the following—are associated with the promotion of one electron from the $[-1/2, -1]$ to the $[-3/2, -1]$ single-particle orbital (see Fig. 6.3(a)), as the interaction energy gain overcomes the kinetic energy cost of occupying orbitals with greater $|j|$, which have null weight at the center of the dot. Consequently, the 2-body ground-state (denoted by the (J_z, S, T_z) total quantum numbers) change from $(-1, 0, -1)$ to $(-2, 1, -1)$, that is, an experimentally traceable singlet-triplet transition occurs. For $N = 3$, as one electron is promoted from the $[-1/2, -1]$ to the $[-3/2, -1]$ single-particle state, the ground-state shifts from $(-5/2, 1/2, -3/2)$ to $(-7/2, 1/2, -3/2)$ without S change.

As we further decrease screening, the impact of the interaction becomes substantial as

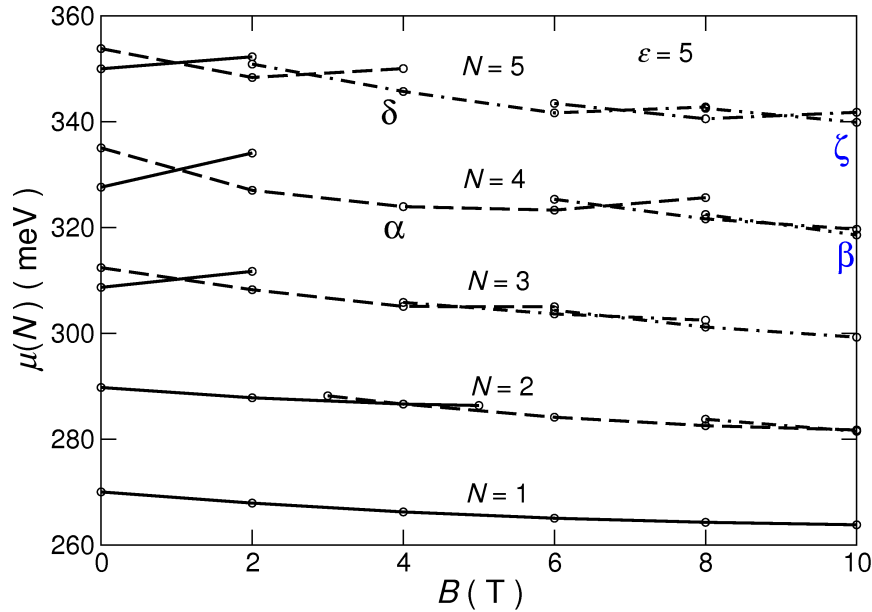


FIGURE 6.5: Chemical potential $\mu(N)$ vs magnetic field B in the interacting regime characterized by $\varepsilon = 5$, with dot radius $R = 250 \text{ \AA}$. The SP level structure (Fig. 6.3(a)) is almost completely washed out.

it is illustrated in Fig. 6.5, where $\varepsilon = 5$. The critical magnetic field at which ground-state transitions occur decreases, specifically the $[-1/2, -1]$ to $[-3/2, -1]$ transition can be traced at $B_c \approx 3.9 \text{ T}$ (for $N = 2$) and $B_c \approx 4.7 \text{ T}$ (for $N = 3$). At this (and at stronger) interaction regimes, the few-body states are linear superpositions of many Slater determinants. However, the $[-1/2, -1] \rightarrow [-3/2, -1]$ transition involves one prevalent configuration in the few-body expansion. Notice that new transitions (absent for weakly interacting regimes) emerge at higher magnetic fields for all electron numbers.

In the strongly interacting regime (see Fig. 6.6), i.e., at $\varepsilon = 2$, there is a further decrease of the critical magnetic field at which transitions take place. In particular, the $[-1/2, -1]$ to $[-3/2, -1]$ transition arises at $B_c \approx 2.4 \text{ T}$ for $N = 2$ and at $B_c \approx 3.1 \text{ T}$ for $N = 3$. The number of crossings further increases for all $\mu(N)$. A similar phenomenology has been seen in QDs in conventional semiconductors [41] and interpreted in terms of analogy with correlated states of the quantum Hall effect at fractional filling factors. Overall, in this regime of interaction, the resonating energy of the N th electron tunneling into the dot is almost constant in contrast to weaker interaction regimes (Figs. 6.3(b) and 6.4) where the slopes of $\mu_0(N)$ strongly vary with B with signs depending on the valley index of the lowest available single-particle level.

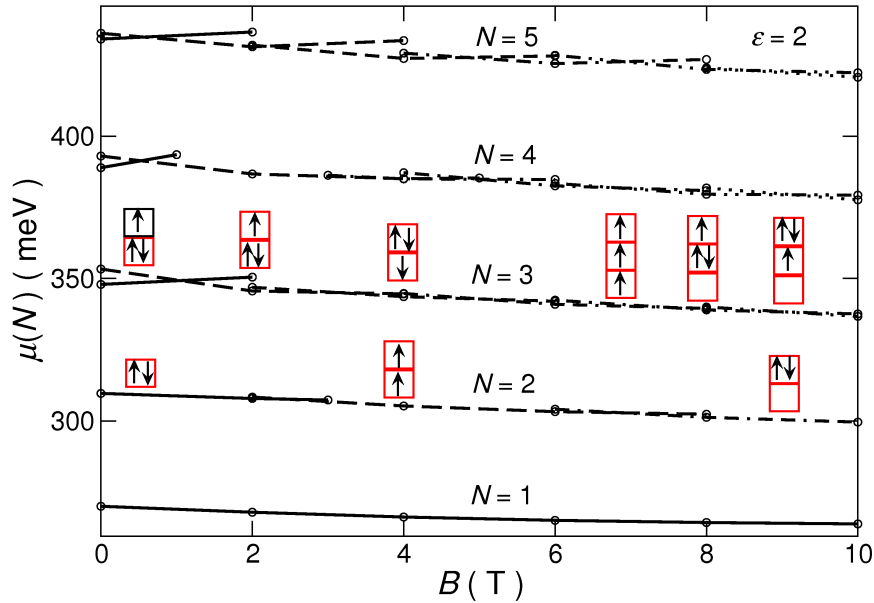


FIGURE 6.6: Chemical potential $\mu(N)$ vs magnetic field B in the strongly interacting regime of $\varepsilon = 2$, with dot radius $R = 250$ Å. The plot shows many transitions between competing ground-states yielding to almost constant slopes of $\mu(N)$ vs B for all N . The Slater determinant of dominant weight in the CI expansion of the $N = 2$ and $N = 3$ wave function, are shown: black (red) boxes represent SP orbitals $[j, \tau]$ of $\tau = 1$ ($\tau = -1$).

6.3 Electron localization onset

We have pointed out the modification of the graphene QD few-body spectrum, determined by the interplay between the electron repulsion and the effect of the magnetic field, which selects the single-particle energy levels of a single valley and determines the energy splitting between them. For increasing magnetic field, the wave functions of the lowest-energy single-particle states—the non-interacting basis set of our few-body calculation—are squeezed towards the dot center. Besides, as the zero LL is approached, the occupation of a prevalent sublattice is enforced [see Fig. 6.2]. To better understand the interplay between electron repulsion and magnetic field in determining the spatial structure of the few-body ground-state, we focus the analysis to $N = 4$ and $N = 5$ electrons and we employ the pair correlation function (PCF)

$$P(\mathbf{r}, \mathbf{r}_0) = \frac{1}{N(N-1)} \left\langle \sum_{i,j}^N \delta(\mathbf{r} - \mathbf{r}_i) \delta(\mathbf{r}_0 - \mathbf{r}_j) \right\rangle, \quad (6.5)$$

where $\langle \dots \rangle$ denotes the expectation value over the N -body ground-state. We recall that the pair correlation function provides the conditional probability to find an electron at \mathbf{r} under the condition that another electron is located at the fixed position \mathbf{r}_0 . We compute the PCF $[P(\varphi)]$ as a function of the azimuthal angle φ by fixing $|\mathbf{r}| = \rho$ at $|\mathbf{r}_0| = \rho_0$, the maximum of the one-body density $n(\mathbf{r}) = \sum_{\sigma \in \{\uparrow, \downarrow\}} n_{\sigma}(\mathbf{r}) N_{\sigma} / N$. For

circular dots both the total one-body density n and the spin-resolved one-body density $n_\sigma(\mathbf{r}) = \langle \sum_{i=1}^N \delta_{\sigma\sigma_i} \delta(\mathbf{r} - \mathbf{r}_i) \rangle / N_\sigma$, with N_σ the number of electrons with spin $\sigma \in \{\uparrow, \downarrow\}$, being isotropic quantities, provide radial correlation only. Tracing $P(\varphi)$, we visualize instead spatial correlations beyond circular symmetry.

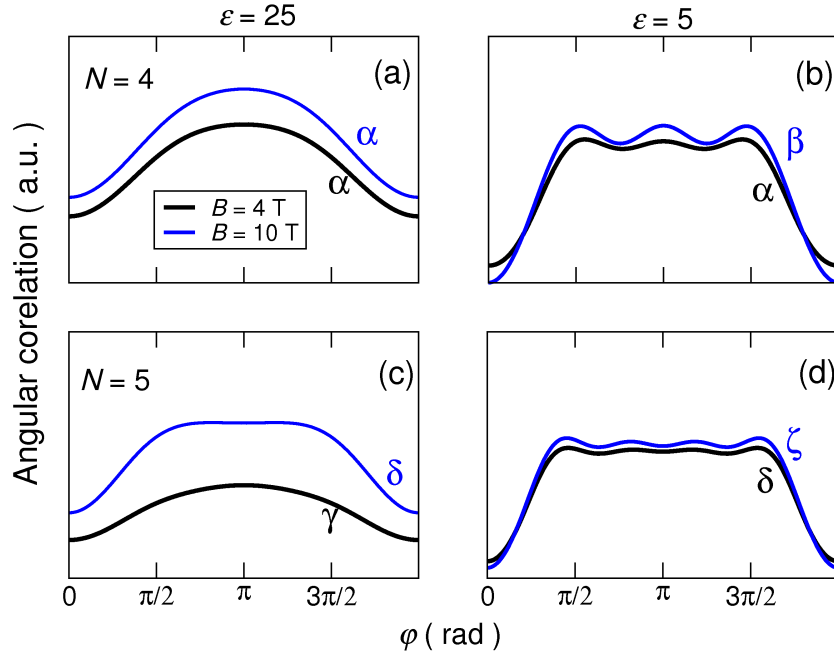


FIGURE 6.7: Ground-state angular correlation $P(\varphi)$ vs azimuthal angle φ at selected $B = 4$ T (black lines) and $B = 10$ T (blue lines). Large screening $\varepsilon = 25$ (left panels) and low screening $\varepsilon = 5$ (right panels) is considered for electron numbers $N = 4$ [(a) and (b) panels] and $N = 5$ [(c) and (d) panels]. Corresponding energy levels are labelled with greek letters in Figs. 6.4 and 6.5. Whilst at weak interaction $\varepsilon = 25$ [panels (a) and (c)], the internal structure of the ground-state wave function features only a slight modulation at $\varphi = 0, 2\pi$ due to the Pauli exclusion principle, for stronger interaction $\varepsilon = 5$ [panels (b) and (d)] the ground-state wave function displays a consistent correlation hole and $N - 1$ peaks indicate the onset of electron localization.

We consider two intermediate interaction regimes corresponding to $\varepsilon = 25$ and $\varepsilon = 5$, which spectra are shown respectively in Figs. 6.4 and 6.5. For these interaction regimes, the ground-state angular correlation $P(\varphi)$ at $B = 4$ T (black curves) and $B = 10$ T (blue curves) are compared in Fig. 6.7.

In the weakly interacting regime of $\varepsilon = 25$, the 4-electron ground-state does not undergo any crossing from $B = 4$ T to $B = 10$ T as it is shown in Fig. 6.4. The total quantum numbers of the state labelled with α in Fig. 6.4 are $(J_z = -4, S = 0, T_z = -2)$, corresponding to double occupation of the low-lying single-particle orbitals. The wave function structure is shown in Fig. 6.7(a): both for $B = 4$ T (black curve) and for $B = 10$ T (blue curve) there is only a weak angular modulation consisting on a depletion at $\varphi = 0, 2\pi$, featuring the excluded region due to the Pauli exclusion principle. By comparing the two curves, it can be observed that as the magnetic field is increased, the

peak-to-valley ratio slightly increases. The angular conditional probability at $B = 10$ T (blue curve) has been computed along a circumference of smaller radius (corresponding to the n maximum) respect to $B = 4$ T (black curve); the difference between the curves in Fig 6.7(a) is a consequence of the evolution of the SP occupied states being squeezed for increasing magnetic field.

In contrast, for $\varepsilon = 5$, the internal structure of the 4-electron ground-state wave function—which is a linear superposition of many Slater determinants—is qualitatively different as it is shown in Fig. 6.7 (b). We recall that at this low screening regime, electron interaction drives ground-state crossings for increasing magnetic field [see Fig. 6.5], namely from α at $B = 4$ T to $(J_z = -8, S = 2, T_z = -2)$ at $B = 10$ T, the last state being denoted as β in Fig. 6.5. At $B = 4$ T, $P(\varphi)$ displays a strong correlation hole and $N - 1$ peaks smoothly modulate the angular PCF. For $B = 10$ T, $P(\varphi)$ —computed at a greater radial distance from the dot center respect to $B = 4$ T—features greater peak-to-valley ratios and clear $N - 1$ maxima at $2\pi/N$.

The conditional probabilities for the 5-electron ground-state are shown in the bottom panels of Fig. 6.7: for large screening, $\varepsilon = 25$ [Fig. 6.7(c)], the black curve corresponds to the ground-state at $B = 4$ T, being denoted as γ [see Fig 6.4], whose total quantum numbers are $(J_z = -7/2, S = 1/2, T_z = -5/2)$. It is compared with the ground-state at $B = 10$ T (blue curve), with total quantum numbers $(J_z = -13/2, S = 1/2, T_z = -5/2)$. This state, we denote with δ , becomes the ground-state as a consequence of the low-lying SP energy levels merging the zero-mode LL [see Figs. 6.4 and 6.3(a)]. The maximum of n is closer to the dot center for δ respect to the analogous for γ . Both γ and δ are featureless except for the hole at $\varphi = 0, 2\pi$. For lower screening, $\varepsilon = 5$ [Fig. 6.7(d)] the ground-state at $B = 4$ T, δ , is compared with the ground state at $B = 10$ T, $\zeta \equiv (J_z = -21/2, S = 3/2, T_z = -5/2)$, which features a slightly more evident modulation.

6.4 Discussion

For a few-electron system in a quantum dot, the identification of cusps of the chemical potential in magneto-transport experiments accesses the ground-state transformations induced by a magnetic field. We computed the magnetic field dependence of the few-electron energy spectrum of a clean graphene QD with a mass gap, for a wide range of interaction regimes (tuned by screening). Transitions between different ground-states in the weakly interacting regime are determined by the structure of the single-particle energy levels: the magnetic field removes the four-fold degeneracy of energy levels at

$B = 0$, the energy levels approach the bulk Landau levels for large magnetic field values, among which the zero-mode graphene LL is valley polarized. We found that the single-particle level structure is progressively washed out as the interaction is increased, enforcing an incrementing number of crossings between ground-states and smoothing the cusps corresponding to the ground-state transformations. In the limit case of very low screening, the obtained structure of the chemical potentials is associated to strong electron correlation and is a signature of Wigner molecule formation analogous to the deviation from the single-particle energy level structure at $B = 0$, presented in Sections 5.2 and 5.6. The onset of electron localization as well as the enhancing role of the magnetic field have been pointed out through the comparison of the spatial structure of the ground-state at different magnetic field values, for intermediate interaction regimes. The predicted modifications of the energy spectrum may be accessed through magneto-tunneling spectroscopy.

Chapter 7

Conclusion

In the last Chapter of this thesis, the main results obtained in this successful PhD research project are summarized. The results are contained in the publication ‘Wigner localization in a graphene quantum dot with a mass gap’, Phys. Rev. B 90, 125446 (2014) and a manuscript entitled ‘Signatures of electron correlation in a graphene quantum dot from Coulomb-blockade spectroscopy’ is presently under preparation.

7.1 Summary

In the present Thesis we have theoretically investigated electron correlation in few-electron graphene quantum dots with a mass gap. We presented the main results in Chapters 5 and 6. In Chapter 5, in the absence of a magnetic field, for up to $N = 6$ excess charge carriers in the conduction band, we extracted the chemical potentials and the addition energies—which can be accessed through Coulomb-blockade spectroscopy—from the exact ground-state energies. We monitored these quantities as the interaction increases when lowering the screening. We found that as the interaction between electrons increases, the four-fold periodicity of the non-interacting filling sequence is completely washed out. The effect of interaction in the ground-state wave function spatial structure was unveiled by considering one-particle charge densities which—for all the electron numbers considered—were found to display ring structures at low screening. This ring structures set in at lower screening for higher dot radii. Additionally, we found that the spin-resolved one-body densities of an even number of electrons, in contrast to the weakly interacting regime where spin-up and spin-down densities differ, tend to coincide as the interaction increases. This is due to the negligible exchange interaction among localized electrons. Angular correlations were found to be enforced by interactions, and the spatial structure of polygonal Wigner molecules was obtained. We found a strong

quenching of the low-lying excitation energies as compared with the non-interacting ones while approaching the limit of perfect electron localization. This strong theoretical evidence of Wigner molecule formation was found for a broad range of realistic values of device parameters. In Chapter 6, we extended our analysis of the graphene QD low-lying energy spectrum to account for the presence of a magnetic field normal to the graphene plane, and we analysed observables accessible through magneto-tunneling spectroscopy measurements. We found that the magnetic field dependence of the energy spectrum is significantly modified by electron-electron interaction, as it induces an increasing number of ground-state transitions flattening the chemical potential structure. We expect our predictions to be inspiring for future experiments in graphene QDs.

7.2 Outlook

Presently, the preparation of clean and electrostatically controlled graphene quantum dots is still a challenging task as well as the experimental validation of our predictions. In bilayer graphene, it has been demonstrated that the electronic band gap can be continuously tuned through a perpendicular electric field. This interesting option has been exploited recently to achieve electrostatically confined bilayer graphene quantum dots. Tunneling spectroscopy measurements have already been performed in very clean architectures both in bilayer graphene on a substrate as well as in suspended bilayer graphene. Therefore we envisage the investigation of strongly correlated behaviour in bilayer graphene quantum dots to be an affordable task, including theoretical predictions to be compared with transport experiments.

Up to now the whole experimental evidence of the electron molecule is indirect, being based on transport measurements. Graphene offers the possibility of directly accessing the spatial structure of Wigner molecules. Therefore, it would be of particular interest to theoretically investigate the dot density of states and local density of states in view of possible comparisons with local probe experiments such as scanning tunneling spectroscopy.

Bibliography

- [1] N. Savage. Super carbon. *Nature*, 483:S13, 2012.
- [2] P. Shapira J. Youtie and S. Arora. *Early Patterns of Commercialization in Graphene, in Science, Technology and Innovation Policy for the Future*. Springer, 2013.
- [3] A. C. Ferrari, F. Bonaccorso, V. Falko, K. S. Novoselov, S. Roche, P. Bøggild, S. Borini, F. Koppens, V. Palermo, and N. Pugno. Science and technology roadmap for graphene, related two-dimensional crystals, and hybrid systems. *Nanoscale*, 2014.
- [4] K. S. Novoselov, V. I. Falko, L. Colombo, P. R. Gellert, M. G. Schwab, and K. Kim. A roadmap for graphene. *Nature*, 490:192–200, 2012.
- [5] G. Fiori, F. Bonaccorso, G. Iannaccone, T. Palacios, D. Neumaier, A. Seabaugh, S. K. Banerjee, and L. Colombo. Electronics based on two-dimensional materials. *Nature Nanotech*, 9:768779, 2014.
- [6] F. H. L. Koppens, T. Mueller, Ph. Avouris, A. C. Ferrari, M. S. Vitiello, and M. Polini. Photodetectors based on graphene, other two-dimensional materials and hybrid systems. *Nature Nanotech.*, 9:780793, 2014.
- [7] W. Han, K. K. Roland, M. Gmitra, and J. Fabian. Graphene spintronics. *Nature Nanotech.*, 9:794807, 2014.
- [8] Graphene flagship, 2013. URL <http://graphene-flagship.eu/>.
- [9] S. Das Sarma, S. Adam, E. H. Hwang, and E. Rossi. Electronic transport in two-dimensional graphene. *Rev. Mod. Phys.*, 83:407–470, May 2011.
- [10] A. H. Castro Neto, F. Guinea, N. M. R. Peres, K. S. Novoselov, and A. K. Geim. The electronic properties of graphene. *Rev. Mod. Phys.*, 81:109, 2009.
- [11] D. S. L. Abergel, V. Apalkov, J. Berashevich, K. Ziegler, and T. Chakraborty. Properties of graphene: a theoretical perspective. *Advances in Physics*, 59(4): 261–482, 2010.

-
- [12] V. N. Kotov, B. Uchoa, V. M. Pereira, A.H. Castro Neto, and F. Guinea. Electron-electron interactions in graphene: current status and perspectives. *Reviews of Modern Physics*, 84:1067, 2012.
- [13] P. Recher and B. Trauzettel. Quantum dots and spin qubits in graphene. *Nanotechnology*, 21:302001, 2010.
- [14] A. V. Rozhkov, G. Giavaras, Y. P. Bliokh, V. Freilikher, and F. Nori. Electronic properties of mesoscopic graphene structures: Charge confinement and control of spin and charge transport. *Phys. Rep.*, 503:77, 2011.
- [15] J. Güttinger, F. Molitor, C. Stampfer, S. Schnez, A. Jacobsen, S. Drscher, T. Ihn, and K. Ensslin. Transport through graphene quantum dot. *Reports on Progress in Physics*, 75:126502, 2012.
- [16] D. Prezzi, D. Varsano, A. Ruini, A. Marini, and E. Molinari. Optical properties of graphene nanoribbons: The role of many-body effects. *Phys. Rev. B*, 77:041404, 2008.
- [17] O. V Yazyev. Emergence of magnetism in graphene materials and nanostructures. *Rep. Prog. Phys.*, 73:056501, 2010.
- [18] X. Wang, Y. Ouyang, L. Jiao, H. Wang, L. Xie, and J. Wu. Graphene nanoribbons with smooth edges behave as quantum wires. *Nature Nanotech*, 6:563, 2011.
- [19] D-K. Ki and A. F. Morpurgo. Crossover from Coulomb blockade to quantum Hall effect in suspended graphene nanoribbons. *Phys. Rev. Lett.*, 108:266601, 2012.
- [20] A. Müller, B. Kaestner, F. Hohls, T. Weimann, K. Pierz, and H. W. Schumacher. Bilayer graphene quantum dot defined by topgates. *J. Appl. Phys.*, 115:233710, 2014.
- [21] S. Engels, A. Epping, C. Volk, S. Korte, B. Voigtländer, K. Watanabe, T. Taniguchi, S. Trellenkamp, and C. Stampfer. Etched graphene quantum dots on hexagonal boron nitride. *Appl. Phys. Lett.*, 103:073113, 2013.
- [22] A. Gamucci, D. Spirito, M. Carrega, B. Karmakar, A. Lombardo, M. Bruna, A. C. Ferrari, L. N. Pfeiffer, K. W. West, M. Polini, and V. Pellegrini. Electron-hole pairing in graphene-gaas heterostructures, 2014. arXiv:1401.0902.
- [23] M. Müller, J. Schmalian, and L. Fritz. Graphene: A nearly perfect fluid. *Phys. Rev. Lett.*, 103:025301, 2009.
- [24] J. Hofmann, E. Barnes, and S. Das Sarma. Why does graphene behave as a weakly interacting system? *Phys. Rev. Lett.*, 113:105502, 2014.

- [25] D. C. Elias, R. V. Gorbachev, A. S. Mayorov, S. V. Morozov, A. A. Zhukov, P. Blake, L. A. Ponomarenko, I. V. Grigorieva, K. S. Novoselov, F. Guinea, and A. K. Geim. Dirac cones reshaped by interaction effects in suspended graphene. *Nat. Phys.*, 7:701, 2011.
- [26] J. Chae, S. Jung, A. F. Young, C. R. Dean, L. Wang, Y. Gao, K. Watanabe, T. Taniguchi, J. Hone, K. L. Shepard, P. Kim, N. B. Zhitenev, and J. A. Stroscio. Renormalization of the graphene dispersion velocity determined from scanning tunneling spectroscopy. *Phys. Rev. Lett.*, 109:116802, 2012.
- [27] D. A. Siegel, W. Regan, A. V. Fedorov, A. Zettl, and A. Lanzara. Charge-carrier screening in single-layer graphene. *Phys. Rev. Lett.*, 110:146802, 2013.
- [28] A. Bostwick, F. Speck, T. Seyller, K. Horn, M. Polini, R. Asgari, A. H. MacDonald, and E. Rotenberg. Observation of plasmarons in quasi-freestanding doped graphene. *Science*, 328:999, 2010.
- [29] A. N. Grigorenko, M. Polini, and K. S. Novoselov. Graphene plasmonics. *Nature photonics*, 6:749–758, 2012.
- [30] D. V. Khveshchenko. Ghost excitonic insulator transition in layered graphite. *Phys. Rev. Lett.*, 87:246802, 2001.
- [31] J. E. Drut and T. A. Lähde. Is graphene in vacuum an insulator? *Phys. Rev. Lett.*, 102:026802, 2009.
- [32] M. Rontani and L. J. Sham. *Novel superfluids volume 2*. K. H. Bennemann, J. B. Ketterson, International Series of Monographs on Physics no. 157, pp. 423-474 (Oxford University Press), Oxford, UK, 2014.
- [33] N. W. Ashcroft and N. D. Mermin. *Solid State Physics*. Holt-Saunders, New York, 1976.
- [34] H. P. Dahal, Y. N. Joglekar and K. S. Bedell, and A. V. Balatsky. Absence of Wigner crystallization in graphene. *Phys. Rev. B*, 74:233405, 2006.
- [35] T. Ando, A. B. Fowler, and F. Stern. Electronic properties of two-dimensional systems. *Rev. Mod. Phys.*, 54:437–672, 1982.
- [36] E. Wigner. On the interaction of electrons in metals. *Phys. Rev.*, 46:1002, 1934.
- [37] X. Du, I. Skachko, F. Duerr, A. Luican, and E. Y. Andrei. Fractional quantum Hall effect and insulating phase of Dirac electrons in graphene. *Nature*, 462:192, 2009.

- [38] K. I. Bolotin, F. Ghahari, M. D. Shulman, H. L. Stormer, and P. Kim. Observation of the fractional quantum Hall effect in graphene. *Nature*, 462:196, 2009.
- [39] E. McCann and M. Koshino. The electronic properties of bilayer graphene. *Rep. Prog. Phys.*, 76:056503, 2013.
- [40] H. Min, R. Bistritzer, J.-J. Su, and A. H. MacDonald. Room-temperature superfluidity in graphene bilayers. *Phys. Rev. B*, 78:121401, 2008.
- [41] S. M. Reimann and M. Manninen. Electronic structure of quantum dots. *Rev. Mod. Phys.*, 74:1283, 2002.
- [42] C. Ellenberger, T. Ihn, C. Yannouleas, U. Landman, K. Ensslin, D. Driscoll, and A.C. Gossard. Excitation spectrum of two correlated electrons in a lateral quantum dot with negligible zeeman splitting. *Physical Review Letters*, 96:126806, 2006.
- [43] S. Kalliakos, M. Rontani, V. Pellegrini, C. P. García, A. Pinczuk, G. Goldoni, E. Molinari, N. L. Pfeiffer, and K. W. West. A molecular state of correlated electrons in a quantum dot. *Nature Physics*, 4:469, 2008.
- [44] A. Singha, V. Pellegrini, A. Pinczuk, L. N. Pfeiffer, K. W. West, and M. Rontani. Correlated electrons in optically tunable quantum dots: Building an electron dimer molecule. *Phys. Rev. Lett.*, 104:246802, 2010.
- [45] S. Pecker, F. Kuemmeth, A. Secchi, M. Rontani, D. C. Ralph, and P. L. McEuen and S. Ilani. Observation and spectroscopy of a two-electron Wigner molecule in an ultraclean carbon nanotube. *Nat. Phys.*, 9:576–581, 2013.
- [46] P. Ruffieux, J. Cai, N. C. Plumb, L. Patthey, D. Prezzi, A. Ferretti, E. Molinari, X. Feng, K. Müllen, C. A. Pignedoli, and R. Fasel. Electronic structure of atomically precise graphene nanoribbons. *ACS Nano*, 6:6930, 2012.
- [47] J. Milton Pereira, Jr. P. Vasilopoulos, and F. M. Peeters. Tunable quantum dots in bilayer graphene. *Nano Lett.*, 7:946, 2007.
- [48] M. T. Allen, J. Martin, and A. Yacoby. Gate-defined quantum confinement in suspended bilayer graphene. *Nature Commun.*, 3:934, 2012.
- [49] A. M. Goossens, S. C. M. Driessen, T. A. Baart, K. Watanabe, T. Taniguchi, and L. M. K. Vandersypen. Gate-defined confinement in bilayer graphene-hexagonal boron nitride hybrid device. *Nano Lett.*, 12:4656, 2012.
- [50] M. Zarenia, B. Partoens, T. Chakraborty, and F. M. Peeters. Electron-electron interactions in bilayer graphene quantum dots. *Phys. Rev. B*, 88:245432, 2013.

- [51] D. Bischoff, F. Libisch, J., Burgdörfer, T. Ihn, and K. Ensslin. Characterizing wave functions in graphene nanodevices: Electronic transport through ultrashort graphene constrictions on a boron nitride substrate. *Phys. Rev. B*, 90:115405, 2014.
- [52] J. Baringhaus, M. Ruan, F. Edler, A. Tejada, M. Sicot, A. Taleb-Ibrahimi, A.-P. Li, Z. Jiang, E. H. Conrad, C. Berger, C. Tegenkamp, and W. A. de Heer. Exceptional ballistic transport in epitaxial graphene nanoribbons. *Nature*, 506:349, 2014.
- [53] I. Romanovsky, C. Yannouleas, and U. Landman. Edge states in graphene quantum dots: Fractional quantum Hall effect analogies and differences at zero magnetic field. *Physical Review B*, 79:075311, 2009.
- [54] P. Potasz, A. D. Güçlü, A. Wöjs, and P. Hawrylak. Electronic properties of gated triangular graphene quantum dots: Magnetism correlations and geometrical effects. *Phys. Rev. B*, 85:075431, 2012.
- [55] A. D. Güçlü, P. Potasz, O. Voznyy, M. Korkusinski, and P. Hawrylak. Magnetism and correlations in fractionally filled degenerate shells of graphene quantum dots. *Phys. Rev. Lett.*, 103:246805, 2009.
- [56] B. Wunsch T. Stauber and F. Guinea. Electron-electron interactions and charging effects in graphene quantum dots. *Phys. Rev. B*, 77:035316, 2008.
- [57] T. Paananen, R. Egger, and H. Siedentop. Signatures of Wigner molecule formation in interacting Dirac fermion quantum dots. *Phys. Rev. B*, 83:085409, 2011.
- [58] N. Yang and J. L. Zhu. Planar Dirac electrons in magnetic quantum dots. *J. Phys. Condens. Matter*, 24:215303, 2012.
- [59] P. Recher, J. Nilsson, G. Burkard, and T. Trauzettel. Bound states and magnetic field induced valley splitting in gate-tunable graphene quantum dots. *Phys. Rev. B*, 79:085407, 2009.
- [60] P. R. Wallace. The band theory of graphite. *Phys. Rev.*, 71:622, 1947.
- [61] J. C. Slonczewski and P. R. Weiss. Band structure of graphite. *Phys. Rev.*, 109:272, 1958.
- [62] J. M. McClure. Diamagnetism of graphite. *Phys. Rev.*, 104:666, 1956.
- [63] G. W. Semenoff. Condensed-matter simulation of a three-dimensional anomaly. *Phys. Rev. Lett.*, 53(26):2449, 1984.

- [64] D. P. DiVincenzo and E. J. Mele. Self-consistent effective-mass theory for intralayer screening in graphite intercalation compounds. *Phys. Rev. B*, 29:1685, 1984.
- [65] R. E. Peierls. Quelques proprietes typiques des corps solides. *Ann. I. H. Poincare*, 5:177–222, 1935.
- [66] L. D. Landau. Zur theorie der phasenumwandlungen II. *Phys. Z. Sowjetunion*, 11: 26–35, 1937.
- [67] L. D. Landau and E. M. Lifshitz. *Statistical Physics, Part I*. Pergamon Press, Oxford, 1980.
- [68] N. D. Mermin. Crystalline order in two dimensions. *Phys. Rev.*, 176:250–254, 1968.
- [69] K. S. Novoselov, A. K. Geim, S. V. Morozov, D. Jiang, Y. Zhang, S. V. Dubonos, I. V. Grigorieva, and A. A. Firsov. Electric field effect in atomically thin carbon films. *Science*, 306:666, 2004.
- [70] K. Novoselov, D. Jiang, F. Schedin, T. Booth, V. Khotkevich, S. Morozov, and A. Geim. Two-dimensional atomic crystals. *Proc. Natl. Acad. Sci. USA*, 102: 10451, 2005.
- [71] H. P. Boehm, R. Setton, and E. Stumpp. Nomenclature and terminology of graphite intercalation compounds. *Carbon*, 24:241, 1986.
- [72] *IUPAC in Compendium of Chemical Terminology*, 1997. (Eds.: A. D. McNaught, A. Wilkinson), 2nd ed. Blackwell Scientific Publications, Oxford.
- [73] C. Berger et al. Ultrathin epitaxial graphite: 2D electron gas properties and a route toward graphene-based nanoelectronics. *J. Phys. Chem. B*, 108:19912, 2004.
- [74] A. J. van Bommel, J. E. Crombeen, and A. van Tooren. LEED and Auger electron observations of the SiC(0001) surface. *Surf. Sci.*, 48:463, 1975.
- [75] J. W. May. Platinum surface LEED rings. *Surf. Sci.*, 17:267, 1969.
- [76] X. K. Lu, H. Huang, N. Nemchuk, and R. S. Ruoff. Tailoring graphite with the goal of achieving single sheets. *Nanotechnology*, 10:269, 1999.
- [77] The 2010 Nobel Prize in Physics Press Release, 2010. URL http://www.nobelprize.org/nobel_prizes/physics/laureates/2010/.
- [78] K. Novoselov, A. Geim, S. Morozov, D. Jiang, M. Katsnelson, I. Grigorieva, S. Dubonos, and A. Firsov. Two-dimensional gas of massless Dirac fermions in graphene. *Nature*, 438:197, 2005.

- [79] Y. Zhang, Y-W. Tan, H. Stormer, and P. Kim. Experimental observation of the quantum Hall effect and Berrys phase in graphene. *Nature*, 201:438, 2005.
- [80] K. S. Novoselov, Z. Jiang, Y. Zhang, S. V. Morozov, H. L. Stormer, U. Zeitlera, J. C. Maan, G. S. Boebinger, P. Kim, and A. K. Geim. Room-temperature quantum Hall effect in graphene. *Science*, 315:1379, 2007.
- [81] O. Klein. Die reflexion von elektronen an einem potentialsprung nach der relativischen dynamik von Dirac. *Z. Phys.*, 53:157, 1929.
- [82] N. Stander, B. Huard, and D. G. Gordon. Evidence for Klein tunneling in graphene p-n junctions. *Phys. Rev. Lett.*, 102:026807, 2009.
- [83] A. F. Young and P. Kim. Quantum interference and Klein tunnelling in graphene heterojunctions. *Nat. Phys.*, 5:222, 2009.
- [84] M. I. Katsnelson, K. S. Novoselov, and A. K. Geim. Chiral tunnelling and the Klein paradox in graphene. *Nat. Phys.*, 2:620, 2006.
- [85] Y. Wang, D. Wong, A. V. Shytov, V. W. Brar, S. Choi, Q. Wu, H-Z. Tsai, W. Regan, A. Zettl, R. K. Kawakami, S. G. Louie, L.S. Levitov, and M. F. Crommie. Observing atomic collapse resonances in artificial nuclei on graphene. *Science*, 340:734–737, 2013.
- [86] A. V. Shytov, M. I. Katsnelson, and L. S. Levitov. Atomic collapse and quasi-rydberg states in graphene. *Phys. Rev. Lett.*, 99:246802, 2007.
- [87] J. C. Meyer, A. K. Geim, M. I. Katsnelson, K. S. Novoselov, T. J. Booth, and S. Roth. The structure of suspended graphene sheets. *Nature*, 446:60, 2007.
- [88] A. K. Geim and I. V. Grigorieva. Van der Waals heterostructures. *Nature*, 499:419, 2013.
- [89] B. Hunt, J. D. Sanchez-Yamagishi, A. F. Young, M. Yankowitz, B. J. LeRoy, K. Watanabe, T. Taniguchi, P. Moon, M. Koshino, P. Jarillo-Herrero, and R. C. Ashoori. Massive Dirac fermions and Hofstadter butterfly in a van der Waals heterostructure. *Science*, 340:1427, 2013.
- [90] C. R. Dean, L. Wang, P. Maher, C. Forsythe, F. Ghahari, Y. Gao, J. Katoch, M. Ishigami, P. Moon, M. Koshino, T. Taniguchi, K. Watanabe, K. L. Shepard, J. Hone, and P. Kim. Hofstadters butterfly and the fractal quantum Hall effect in moir superlattices. *Nature*, 497:598, 2013.
- [91] D. R. Hofstadter. Energy levels and wave functions of Bloch electrons in rational and irrational magnetic fields. *Phys. Rev. B*, 14:2239–2249, 1976.

- [92] C. Berger, Z. Song, X. Li, X. Wu, N. Brown, C. Naud, D. Mayou, T. Li, J. Hass, A. Marchenkov, E. Conrad, P. N. First, and W. A. de Heer. Electronic confinement and coherence in patterned epitaxial graphene. *Science*, 312:1191, 2006.
- [93] L. Liao, Y. C. Lin, M. Bao, R. Cheng, J. Bai, Y. Liu, Y. Qu, K. L. Wang, Y. Huang, and X. Duan. High-speed graphene transistors with a self-aligned nanowire gate. *Nature*, 467:305, 2010.
- [94] Y. M. Lin, C. Dimitrakopoulos, K. A. Jenkins, D. B. Farmer, H. Y. Chiu, A. Grill, and Ph. Avouris. 100-ghz transistors from wafer-scale epitaxial graphene. *Science*, 327:662, 2010.
- [95] J. Güttinger. *Graphene Quantum Dots*. PhD thesis, ETH Zurich, 2011.
- [96] M. S. Dresselhaus, G. Dresselhaus, and J. E. Fischer. Graphite intercalation compounds: Electronic properties in the dilute limit. *Phys. Rev. B*, 15:3180, 1977.
- [97] W. W. Toy, M. S. Dresselhaus, and G. Dresselhaus. Minority carriers in graphite and the h -point magnetoreflexion spectra. *Phys. Rev. B*, 15:4077–4090, 1977.
- [98] M. I. Katsnelson. *Graphene: Carbon in Two Dimensions*. Cambridge University-press, New York, 2012.
- [99] T. Ihn, J. Güttinger, F. Molitor, S. Schnez, E. Schurtenberger, A. Jacobsen, S. Hellmüller, T. Frey, S. Dirscher, C. Stampfer, and K. Ensslin. Graphene single-electron transistors. *Materials Today*, 13:44, 2010.
- [100] A. Bostwick, T. Ohta, Th. Seyller, K. Horn, and E. Rotenberg. Quasiparticle dynamics in graphene. *Nature Physics*, 3:36, 2007.
- [101] P. A. M. Dirac. The quantum theory of the electron. *Phil. Trans. R. Soc. A*, 117:610, 1928.
- [102] M. Berry and R. Mondragon. Neutrino billiards: time-reversal symmetry-breaking without magnetic fields. *Proc. R. Soc. Lond. A*, 412:53, 1987.
- [103] T. Ando, T. Nakanishi, and R. Saito. Berrys phase and absence of back scattering in carbon nanotubes. *J. Phys. Soc. Jpn*, 67:2857, 1998.
- [104] L. D. Landau and E. M. Lifshitz. *Quantum mechanics. Vol. 3 of Course in Theoretical Physic*. Pergamon Press, Oxford, 1977.
- [105] M. L. Sadowski, G. Martinez, M. Potemski, C. Berger, and W. A. de Heer. Landau level spectroscopy of ultrathin graphite layers. *Phys. Rev. Lett.*, 97:266405, 2006.

-
- [106] G. Li and E. Y. Andrei. Observation of Landau levels of Dirac fermions in graphite. *Nature Physics*, 3:623, 2007.
- [107] L. A. Ponomarenko, R. Yang, R. V. Gorbachev, P. Blake, A. S. Mayorov, K. S. Novoselov, M. I. Katsnelson, and A. K. Geim. Density of states and zero Landau level probed through capacitance of graphene. *Phys. Rev. Lett.*, 105:136801, 2010.
- [108] Z. Jiang, E. A. Henriksen, L. C. Tung, Y. J. Wang, M. E. Schwartz, M. Y. Han, P. Kim, and H. L. Stormer. Infrared spectroscopy of Landau levels of graphene. *Phys. Rev. Lett.*, 98:197403, 2007.
- [109] Z. G. Chen, Z. Shi, W. Yang, X. Lu, Y. Lai, H. Yan, F. Wang, G. Zhang, and Z. Li. Observation of an intrinsic bandgap and Landau level renormalization in graphene/boron-nitride heterostructures. *Nat Commun*, 5:4461, 2014.
- [110] F. D. M. Haldane. Model for a quantum Hall effect without Landau levels: Condensed-matter realization of the parity anomaly. *Phys. Rev. Lett.*, 61:2015, 1988.
- [111] T. Ando. Theory of electronic states and transport in carbon nanotubes. *J. Phys. Soc. Jpn.*, 74:777, 2005.
- [112] T. Ihn. *Semiconductor Nanostructures: Quantum States and Electronic Transport*. Oxford University Press, Oxford, 2010.
- [113] L. D. Landau. Paramagnetism of metals. *Z. Phys.*, 64:629, 1930.
- [114] M. F. Atiyah and I. M. Singer. The index of elliptic operators i, ii, iii. *Ann. Math.*, 87:484, 1968.
- [115] K. Novoselov, Z. Jiang, Y. Zhang, S. Morozov, H. Stormer, U. Zeitler, J. Maan, G. Boebinger, P. Kim, and A. Geim. Room-temperature quantum Hall effect in graphene. *Science*, 315:1379, 2007.
- [116] D. Loss and D. D. Vincenzo. Quantum computation with quantum dots. *Phys. Rev. A*, 57:120, 1998.
- [117] G. Schön, L.L. Sohn, L. P. Kouwenhoven, North Atlantic Treaty Organization. Scientific Affairs Division, and NATO Advanced Study Institute on Mesoscopic Electron Transport, editors. *Mesoscopic electron transport*. Dordrecht, Netherlands; Boston, Mass.: Kluwer Academic Publishers, 1997.
- [118] D. Huertas-Hernando, F. Guinea, and A. Brataas. Spin-orbit coupling in curved graphene, fullerenes, nanotubes, and nanotube caps. *Phys. Rev. B*, 74:155426, 2006.

- [119] H. Min, J. E. Hill, N. Sinitsyn, B. Sahu, L. Kleinman, and A. MacDonald. Intrinsic and rashba spin-orbit interactions in graphene sheets. *Phys. Rev. B*, 74:165310, 2006.
- [120] Y. Yao, F. Ye, X-L. Qi, S-C. Zhang, and Z. Fang. Spin-orbit gap of graphene: First-principles calculations. *Phys. Rev. B*, 75:041401, 2007.
- [121] M. Fuchs, J. Schliemann, and B. Trauzettel. Ultralong spin decoherence times in graphene quantum dots with a small number of nuclear spins. *Phys. Rev. B*, 88:245441, 2013.
- [122] M. Gmitra, S. Konschuh, C. Ertler, C. Ambrosch-Draxl, and J. Fabian. Band-structure topologies of graphene: Spin-orbit coupling effects from first principles. *Phys. Rev. B*, 80:235431, 2009.
- [123] D. Loss B. Trauzettel, D. V. Bulaev and G. Burkard. Spin qubits in graphene quantum dots. *Nature Phys.*, 3:192–6, 2007.
- [124] A. Rycerz, J. Tworzydło, and C. W. J. Beenakker. Valley filter and valley valve in graphene. *Nat. Phys.*, 3:172, 2007.
- [125] Y. Jiang, T. Low, K. Chang, M. I. Katsnelson, and F. Guinea. Generation of pure bulk valley current in graphene. *Phys. Rev. Lett.*, 110:046601, 2013.
- [126] D. Gunlycke and C. T. White. Graphene valley filter using a line defect. *Phys. Rev. Lett.*, 106:136806, 2011.
- [127] C. Stampfer, J. Güttinger, F. Molitor, D. Graf, T. Ihn, and K. Ensslin. Tunable Coulomb blockade in nanostructured graphene. *Appl. Phys. Lett.*, 92:012102, 2008.
- [128] L.A Ponomarenko, F. Schedin, M. I. Katsnelson, E. W. Hill R. Yang, K. S. Novoselov, and A. K. Geim. Chaotic Dirac billiard in graphene quantum dots. *Science*, 320:356, 2008.
- [129] S. Schnez, F. Molitor, C. Stampfer, J. Güttinger, I. Shorubalko, and T. Ihn K. Ensslin. Observation of excited states in a graphene quantum dot. *Appl. Phys. Lett.*, 94:012107, 2009.
- [130] D. Subramaniam, F. Libisch, Y. Li, C. Pauly V., Geringer, R. Reiter, T. Mashoff, M. Liebmann, J. Burgdörfer, C. Busse, T. Michely, R. Mazzarello, M. Pratzer, and M. Morgenstern. Wave-function mapping of graphene quantum dots with soft confinement. *Phys. Rev. Lett.*, 108:046801, 2012.
- [131] S. V. Morozov, K. S. Novoselov, M. I. Katsnelson, F. Schedin, D. C. Elias, J. A. Jaszczak, and A. K. Geim. Giant intrinsic carrier mobilities in graphene and its bilayer. *Phys. Rev. Lett.*, 100:016602, 2008.

- [132] G. Giovannetti, P. A. Khomyakov, G. Brocks, P. J. Kelly, and J. van den Brink. Substrate-induced band gap in graphene on hexagonal boron nitride: Ab initio density functional calculations. *Phys. Rev. B*, 76:073103, 2007.
- [133] J. H. Bardarson, M. Titov, and P. W. Brouwer. Electrostatic confinement of electrons in an integrable graphene quantum dot. *Phys. Rev. Lett.*, 102:226803, 2009.
- [134] K. Novoselov. Mind the gap. *Nature Materials*, 6:720, 2007.
- [135] M. R. Setare and D. Jahani. Klein tunneling of massive Dirac fermions in single-layer graphene. *Condensed Matter*, 405:1433, 2009.
- [136] T. Low, F. Guinea, and M. I. Katsnelson. Gaps tunable by electrostatic gates in strained graphene. *Phys. Rev. B*, 83:195436, 2011.
- [137] F. Wang, G. Liu, S. Rothwell, M. Nevius, A. Tejeda, A. Taleb-Ibrahimi, L.C. Feldman, P. I. Cohen, and E. H. Conrad. Wide-gap semiconducting graphene from nitrogen-seeded SiC. *Nano Letters*, 13(10):4827–4832, 2013.
- [138] J. Berashevich and T. Chakraborty. Tunable band gap and magnetic ordering by adsorption of molecules on graphene. *Phys. Rev. B*, 80:033404, 2009.
- [139] 2012. Tech. Dig. Int. Electron Devices Meeting.
- [140] F. Schwierz. Graphene transistors: Status, prospects, and problems. *Proc. IEEE*, 101:1567, 2013.
- [141] G. Giavaras and F. Nori. Dirac gap-induced graphene quantum dot in an electrostatic potential. *Phys. Rev. B*, 83:165427, 2011.
- [142] C. Enderlein, Y. S. Kim, A. Bostwick, E. Rotenberg, and K. Horn. The formation of an energy gap in graphene on ruthenium by controlling the interface. *New J. Phys.*, 12:033014, 2010.
- [143] J. A. Kelber, M. Zhou, S. Gaddam, F. L. Pasquale, L. M. Kong, and P. A. Dowben. Direct graphene growth on oxides: Interfacial interactions and band gap formation. *ECS Trans.*, 45:49, 2012.
- [144] W. A. de Heer, C. Berger, X. Wu, M. Sprinkle, Y. Hu, M. Ruan, J. A. Stroscio, P. N. First, R. Haddon, B. Piot, C. Faugeras, M. Potemski, and J-S. Moon. Epitaxial graphene electronic structure and transport. *J. Phys. D: Appl. Phys.*, 43:374007, 2010.

- [145] S. Y. Zhou, G. H. Gweon, A. V. Fedorov, P. N. First, W. A. de Heer, D. H. Lee, F. Guinea, A. H. Castro Neto, and A. Lanzara. Substrate-induced bandgap opening in epitaxial graphene. *Nature Mater.*, 6:770, 2007.
- [146] S. Y. Zhou, D. A. Siegel, A. V. Fedorov, F. El Gabaly, A. K. Schmid, A. H. Castro Neto, and A. Lanzara D-H. Lee. Origin of the energy bandgap in epitaxial graphene. *Nature Mater.*, 7:259, 2008.
- [147] E. Rotenberg, A. Bostwick, T. Ohta, J. L. McChesney, T. Seyller, and K. Horn. Origin of the energy bandgap in epitaxial graphene. *Nature Mater.*, 7:258, 2008.
- [148] A. K. Geim and K. S. Novoselov. The rise of graphene. *Nature Mater.*, 6:183, 2007.
- [149] J. Xue, J. Sanchez-Yamagishi, D. Bulmash, P. Jacquod, A. Deshpande, K. Watanabe, T. Taniguchi, P. Jarillo-Herrero, and B. J. LeRoy. Scanning tunnelling microscopy and spectroscopy of ultra-flat graphene on hexagonal boron nitride. *Nature Materials*, 10:282, 2011.
- [150] C. R. Dean, A. F. Young, I. Meric, C. Lee, S. Sorgenfrei L. Wang, K. Watanabe, T. Taniguchi, P. Kim, K. L. Shepard, and J. Hone. Boron nitride substrates for high-quality graphene electronics. *Nature Nanotechnology*, 5:722, 2010.
- [151] R. Decker, Y. Wang, V. W. Brar, W. Regan, H.-Z. Tsai, Q. Wu, W. Gannett, A. Zettl, and M. F. Crommie. Local electronic properties of graphene on a BN substrate via scanning tunneling microscopy. *Nano Letters*, 11:2291, 2011.
- [152] C. R. Woods, L. Britnell, A. Eckmann, R. S. Ma, J. C. Lu, H. M. Guo, X. Lin, G. L. Yu, Y. Cao, R. V. Gorbachev, A. V. Kretinin, J. Park, L. A. Ponomarenko, M. I. Katsnelson, Yu. N. Gornostyrev, K. Watanabe, T. Taniguchi, C. Casiraghi, H.-J. Gao, A. K. Geim, and K. S. Novoselov. Commensurate-incommensurate transition in graphene on hexagonal boron nitride. *Nat. Phys.*, 10:451, 2014.
- [153] J. Jung, A. DaSilva, S. Adam, and A. H. MacDonald. Origin of band gaps in graphene on hexagonal boron nitride, 2014. arxiv:1403.0496.
- [154] M. Bokdam, T. Amlaki, G. Brocks, and P. J. Kelly. Band gaps in incommensurable graphene on hexagonal boron nitride. *Phys. Rev. B*, 89:201404, May 2014.
- [155] C. W. J. Beenakker. Colloquium. *Rev. Mod. Phys.*, 80:1337, 2008.
- [156] J. L. Mañes, F. Guinea, and M. A. H. Vozmediano. Existence and topological stability of Fermi points in multilayered graphene. *Phys. Rev. B*, 75:155424, 2007.

- [157] R. Hanson, L. P. Kouwenhoven, J. R. Petta, S. Tarucha, and L. M. K. Vandersypen. Spins in few-electron quantum dots. *Rev. Mod. Phys.*, 79:1217, 2007.
- [158] C. W. J. Beenakker. Theory of Coulomb-blockade oscillations in the conductance of a quantum dot. *Phys. Rev. B*, 44:1646, 1991.
- [159] H. van Houten, C. W. J. Beenakker, and A. A. M. Staring. Coulomb-blockade oscillations in semiconductor nanostructures. In *Single Charge Tunneling, NATO ASI Series B294 (Plenum, New York, 1992)*, page 167216, 1992.
- [160] J. Güttinger, C. Stampfer, F. Libisch, T. Frey, J. Burgdörfer, T. Ihn, and K. Ensslin. Electron-hole crossover in graphene quantum dots. *Phys. Rev. Lett.*, 103:046810, 2009.
- [161] J. Güttinger, T. Frey, C. Stampfer, T. Ihn, and K. Ensslin. Spin states in graphene quantum dots. *Phys. Rev. Lett.*, 105:116801, 2010.
- [162] C. Volk, C. Neumann, S. Kazarski, S. Fringes, S. Engels, F. Haupt, A. Müller, and C. Stampfer. Probing relaxation times in graphene quantum dots. *Nat. Commun.*, 4:1753, 2013.
- [163] A. Jacobsen, P. Simonet, K. Ensslin, and T. Ihn. Finite-bias spectroscopy of a three-terminal graphene quantum dot in the multilevel regime. *Phys. Rev. B*, 89:165413, 2014.
- [164] S. K. Hämäläinen, Z. Sun, M. P. Boneschanscher, A. Uppstu, M. Ijäs, A. Harju, D. Vanmaekelbergh, and P. Liljeroth. Quantum-confined electronic states in atomically well-defined graphene nanostructures. *Phys. Rev. Lett.*, 107:236803, 2011.
- [165] J. Cai, P. Ruffieux, R. Jaafar, M. Bieri, T. Braun, S. Blankenburg, M. Muoth, A. P. Seitsonen, M. Saleh, X. Feng, K. Mullen, and R. Fasel. Atomically precise bottom-up fabrication of graphene nanoribbons. *Nature*, 466:470, 2010.
- [166] G. F. Giuliani and G. Vignale. *Quantum Theory of the Electron Liquid*. Cambridge University Press, Cambridge UK, 2005.
- [167] B. Tanatar and D. M. Ceperley. Ground state of the two-dimensional electron gas. *Phys. Rev. B*, 39:5005, 1989.
- [168] Y. P. Monarkha and V. E. Syvokon. A two-dimensional Wigner crystal. *Low Temp. Phys.*, 38:1067, 2012.
- [169] C. C. Grimes and G. Adams. Evidence for a liquid-to-crystal phase transition in a classical, two-dimensional sheet of electrons. *Phys. Rev. Lett.*, 42:795, 1979.

- [170] E. Y. Andrei, G. Deville, F. Williams and I. B. Paris, and B. Etienne. Observation of magnetically induced Wigner solids. *Physical Review Letters*, 60(26):2765–2768, 1988.
- [171] V. M. Pudalov, M. D’Iorio, S.V. Kravchenko, and J.W. Campbell. Zero-magnetic-field collective insulator phase in a dilute 2D electron system. *Physical Review Letters*, 70(12):1866–1869, 1993.
- [172] S. Das Sarma and A. Pinczuk. *Perspectives in Quantum Hall Effects*. Wiley, New York, 1997.
- [173] R. L. Willett, H. L. Stormer, D. C. Tsui, L. N. Pfeiffer, K. W. West, and K. W. Baldwin. Termination of the series of fractional quantum Hall states at small filling factors. *Phys. Rev. B*, 38:7881–7884, 1988.
- [174] C. H. Zhang and Y. N. Joglekar. Wigner crystal and bubble phases in graphene in the quantum Hall regime. *Phys. Lett. B*, 75:245414, 2007.
- [175] O. Poplavskyy, M. O. Goerbig, and C. Morais Smith. Local density of states of electron-crystal phases in graphene in the quantum Hall regime. *Phys. Rev. B*, 80:195414, 2009.
- [176] B. Reusch, W. Häusler, and H. Grabert. Wigner molecules in quantum dots. *Phys. Rev. B*, 63:113313, 2001.
- [177] S. M. Reimann, M. Koskinen, and M. Manninen. Formation of Wigner molecules in small quantum dots. *Phys. Rev. B*, 62:8108, 2000.
- [178] R. Egger, W. Häusler, C.H. Mak, and H. Grabert. Crossover from Fermi liquid to Wigner molecule behavior in quantum dots. *Phys. Rev. Lett.*, 82:3320, 1999.
- [179] M. Koskinen, M. Manninen, and S. M. Reimann. Hund’s rules and spin density waves in quantum dots. *Phys. Rev. Lett.*, 79:1389–1392, 1997.
- [180] A. V. Filinov, M. Bonitz, and Yu. E. Lozovik. Wigner crystallization in mesoscopic 2D electron systems. *Phys. Rev. Lett.*, 86:3851, 2001.
- [181] E. Räsänen, H. Saarikoski, M. J. Puska, and R. M. Nieminen. Wigner molecules in polygonal quantum dots: A density-functional study. *Phys. Rev. B*, 67:035326, 2003.
- [182] G. W. Bryant. Electronic structure of ultrasmall quantum-well boxes. *Phys. Rev. Lett.*, 59:1140, 1987.
- [183] C. E. Creffield, W. Häusler, J. H. Jefferson, and S. Sarkar. Interacting electrons in polygonal quantum dots. *Phys. Rev. B*, 59:10719, 1999.

-
- [184] D. C. Thompson and A. Alavi. Electron correlation in a hard spherical external potential: Wigner molecule formation and hybridization. *Phys. Rev. B*, 69:201302, 2004.
- [185] A. Ghosal, A. D. Güçlü, C. J. Umrigar, D. Ullmo, and H. U. Baranger. Incipient Wigner localization in circular quantum dots. *Phys. Rev. B*, 76:085341, 2007.
- [186] A. Ghosal, A. D. Güçlü, C. J. Umrigar, D. Ullmo, and H. U. Baranger. Correlation induced inhomogeneity in circular quantum dots. *Nature Physics*, 2:336, 2006.
- [187] M. Saint Jean, C. Even, and C. Guthmann. Macroscopic 2D Wigner islands. *Europhys. Lett.*, 55:4551, 2001.
- [188] F. Bolton and U. Rössler. Classical model of a Wigner crystal in a quantum dot. *Superlattices Microstruct.*, 13:139, 1993.
- [189] V. M. Bedanov and F. M. Peeters. Ordering and phase transition of charged particles in a classical finite two-dimensional system. *Phys. Rev. B*, 49:2667, 1994.
- [190] C. Yannouleas and U. Landman. Collective and independent-particle motion in two-electron artificial atoms. *Phys. Rev. Lett.*, 85:1726–1729, 2000.
- [191] M. Koskinen, M. Manninen, B. Mottelson, and S. M. Reimann. Rotational and vibrational spectra of quantum rings. *Phys. Rev. B*, 63:205323, 2001.
- [192] C. P. García, V. Pellegrini, A. Pinczuk, M. Rontani, G. Goldoni, E. Molinari, B. S. Dennis, L. N. Pfeiffer, and K. W. West. Evidence of correlation in spin excitations of few-electron quantum dots. *Phys. Rev. Lett.*, 95:266806, 2005.
- [193] A. Secchi and M. Rontani. Coulomb versus spinorbit interaction in few-electron carbon-nanotube quantum dots. *Phys. Rev. B*, 80:041404(R), 2009.
- [194] A. Secchi and M. Rontani. Wigner molecules in carbon-nanotube quantum dots. *Phys. Rev. B*, 82:035417, 2010.
- [195] J. M. Luttinger and W. Kohn. Motion of electrons and holes in perturbed periodic fields. *Phys. Rev.*, 97:869–883, Feb 1955.
- [196] M. Abramowitz and I.A Stegun. *Handbook of Mathematical Functions*. Dover (New York), 1965.
- [197] F. Bowman. *Introduction to Bessel Functions*. Dover, New York, 1958.
- [198] M. Rontani and E. Molinari. Imaging quasiparticle wave functions in quantum dots via tunneling spectroscopy. *Phys. Rev. B*, 71:233106, 2005.

- [199] M. Rontani, C. Cavazzoni, D. Bellucci, and G. Goldoni. Full configuration interaction approach to the few-electron problem in artificial atoms. *J. Chem. Phys.*, 124:124102, 2006.
- [200] K. Ohno. Some remarks on the pariser-parr-pople method. *Theor. Chim. Acta*, 2: 219, 1964.
- [201] P. Fulde. *Electron Correlations in Molecules and Solids*. Springer Verlag, Berlin, New York,, 1995.
- [202] R. B. Lehoucq, K. Maschhoff, D. C. Sorensen, and C. Yang, 1997. URL <http://www.caam.rice.edu/software/ARPACK/>. ARPACK computer code.
- [203] W. Greiner, B. Müller, and J. Rafelsk. *Quantum Electrodynamics of Strong Fields*. Springer Verlag, Berlin, 1985.
- [204] W. Häusler and R. Egger. Artificial atoms in interacting graphene quantum dots. *Phys. Rev. B*, 80:161402, 2009.
- [205] A. L. Walter, A. Bostwick, K.-J. Jeon, F. Speck, M. Ostler, T. Seyller, L. Moreschini, Y.-J. Chang, M. Polini, R. Asgari, A. H. MacDonald, K. Horn, and E. Rotenberg. Effective screening and the plasmaron bands in graphene. *Phys. Rev. B*, 84: 085410, 2011.
- [206] C. Hwang, D. A. Siegel, S. K. Mo, W. Regan, A. Ismach, Y. Zhang, A. Zettl, and A. Lanzara. Fermi velocity engineering in graphene by substrate modification. *Sci. Rep.*, 2:590, 2012.
- [207] A. Secchi and M. Rontani. Intervalley scattering induced by Coulomb interaction and disorder in carbon-nanotube quantum dots. *Phys. Rev. B*, 88:125403, Sep 2013.
- [208] S. Tarucha, D. C. Austing, T. Honda, R. J. van der Hage, and L. P. Kouwenhoven. Shell filling and spin effects in a few electron quantum dot. *Phys. Rev. Lett.*, 77: 3613–3616, 1996.

Karina Andrea Guerrero Becerra

Curriculum Vitae

☎ (+39) 0516218894
✉ 90811@studenti.unimore.it

Personal information

Name **Karina Andrea.**
Surname **Guerrero Becerra.**
Nationality **Colombian.**
Date of birth **02/11/1984.**

Education

- 2011–2015 **PhD in Physics (expected February 2015)**, School of Graduate Studies in Physics and Nanosciences, Università degli Studi di Modena e Reggio Emilia, Italy. Thesis title: “Electron correlation in graphene quantum dots”. Supervisor: Dr. Massimo Rontani.
- 2007–2010 **Master in Physics, Subject area: Theoretical Physics**, Alma Mater Studiorum—Università degli Studi di Bologna, Italy. Thesis title: “Applications of sine-Gordon theory in non linear quantum optics”. Supervisor: Dr. Francesco Ravanini. Final mark 110/110.
- 2003–2006 **Bachelor in Physics**, Alma Mater Studiorum—Università degli Studi di Bologna, Italy. Thesis title: “Statistical mechanics of an urban complex network”. Supervisor: Dr. Sandro Rambaldi. Final mark 105/110.
- 1998–2002 **High School diploma, scientific area**, Liceo Scientifico Leonardo Da Vinci, Bogotá, Colombia. Final mark 100/100.

Teaching experience

- 2011–2012 **Undergraduate teaching assistant**, Department of Physics, Università degli Studi di Modena e Reggio Emilia, Italy. 2th-year bachelor’s course: “Mathematical methods for Physics”.
It involved the discussion of lecture material, correction of homework assignments and presiding exercise sessions
- 2009–2011 **Tutor of the “Fisica in Moto” educational workshop**, joint project of the Ducati Foundation, the Malpighi School and the Università degli Studi di Modena e Reggio Emilia, Borgo Panigale, Italy. High school-level course of classical mechanics.
It involved teaching the laws of classical mechanics through interactive examples in the context of motorcycle world.

Workshops, conferences and schools

- 08/2008 **International Summer School in Theoretical Physics**, Utrecht University, The Netherlands.

- 05/2011 **“Introduction to high performance scientific computing (HPC): tools and techniques”**, CINECA consortium, Super Computing Applications and Innovation (SCAI), Casalecchio di Reno, Bologna, Italy.
- 08/2011 **“Quantum Phenomena in graphene, other low-dimensional materials, and optical lattices” Summer School**, ICAM-I2CAM, Ettore Majorana Foundation and Centre for Scientific Culture, Erice, Italy.
- 09/2012 **“Graphene: From band structure to many-body physics” workshop**, CECAM, University of Bremen, Germany.
contribution: poster
- 06/2013 **“2nd Meeting of the Nanosciences Institute CNR-NANO” workshop**, CNR-NANO S3 research center, University of Modena and Reggio Emilia, Italy.
contribution: poster
- 02/2014 **“GRAPHEsp2014” workshop**, Graphene Flagship, Lanzarote, Spain.
contribution: oral
- 03/2014 **“The American Physical Society March Meeting 2014”**, APS Physics, Denver, USA.
contribution: oral
- 05/2014 **“8th International Conference on Quantum Dots”**, Italian institute of technology (IIT) and Università degli Studi di Milano-Bicocca, Pisa, Italy.
contribution: oral

Publications

- K. A. Guerrero-Becerra and Massimo Rontani, **Wigner localization in a graphene quantum dot with a mass gap**, Phys. Rev. B 90, 125446 (2014).
- K. A. Guerrero-Becerra and Massimo Rontani, **Signatures of electron correlation in a graphene quantum dot from Coulomb-blockade spectroscopy**, in preparation

Research interests

- electronic and transport properties of graphene-based nanostructures
- electron correlation effects in nanostructures

Grants and fellowships

- 2013-2014 **Research fellowship**, granted by CNR-NANO S3 Research Center, Modena Italy.
- 2011-2013 **PhD fellowship**, granted by MIUR (Ministry for Education, University and Research), Italy.
- 2003-2007 **Undergraduate fellowship for international students**, granted by Alma Mater Studiorum - Università di Bologna, Italy.

Computer skills

- OS Microsoft Windows, GNU/Linux
- Maths Wolfram's Mathematica

Programming Fortran
Text editing L^AT_EX, OpenOffice, Microsoft Word
Graphics Photoshop, GIMP
Plotting/data Xmgrace, IGOR Pro
analysis

Language skills

Spanish **Mother tongue**
Italian **Proficient user**
English **Fluent**